2007-08-14

The Effect of Nonlinear Propagation on Near-field Acoustical Holography

Micah Raymond Shepherd
Brigham Young University - Provo

THE EFFECT OF NONLINEAR PROPAGATION ON NEAR-FIELD ACOUSTICAL HOLOGRAPHY

by

Micah R. Shepherd

A thesis submitted to the faculty of

Brigham Young University

in partial fulfillment of the requirements for the degree of

Master of Science

Department of Physics and Astronomy

Brigham Young University

Dec 2007

BRIGHAM YOUNG UNIVERSITY

GRADUATE COMMITTEE APPROVAL

of a thesis submitted by

Micah R. Shepherd

This thesis has been read by each member of the following graduate committee and by majority vote has been found to be satisfactory.

Date	Kent L. Gee, Chair
Date	Timothy W. Leishman
Date	Scott D. Sommerfeldt

BRIGHAM YOUNG UNIVERSITY

As chair of the candidate's graduate committee, I have read the thesis of Micah R. Shepherd in its final form and have found that (1) its format, citations, and bibliographical style are consistent and acceptable and fulfill university and department style requirements; (2) its illustrative materials including figures, tables, and charts are in place; and (3) the final manuscript is satisfactory to the graduate committee and is ready for submission to the university library.

Date

Kent L. Gee
Chair, Graduate Committee

Accepted for the Department

J. Ward Moody, Graduate Coordinator
Department of Physics and Astronomy

Accepted for the College

Thomas W. Sederberg, Associate Dean
College of Physical and Mathematical Sciences

ABSTRACT

THE EFFECT OF NONLINEAR PROPAGATION ON NEAR-FIELD ACOUSTICAL HOLOGRAPHY

Micah R. Shepherd

Department of Physics and Astronomy

Master of Science

Near-field acoustical holography (NAH) has been used extensively for acoustical imaging of infinitesimal-amplitude (or small-amplitude) sources. However, recent interests are in the application of NAH to image finite-amplitude (or high-amplitude) sources such as jets and rockets. Since NAH is based on linear equations and finite-amplitude sources imply nonlinear effects, which cause shock formation and consequently an altered spectral shape, a feasibility study is carried out to determine the effect of nonlinear propagation on NAH.

Jet and rocket sources typically have a distinct spectral shape resembling a 'haystack' and center frequencies varying from 30 to 300 Hz. To test the effect of nonlinear propagation on jet or rocket noise, several waveforms with varying spectral shapes and center frequencies were created and numerically propagated in one dimension using a nonlinear propagation algorithm. Bispectral methods were used to determine the amount and effect of nonlinearity,

showing that higher center frequencies lead to more nonlinearities for a given amplitude. Also, higher-order statistical analysis of the time derivative of the waveforms was used to determine information about the relative amount of waveform steepening and shock coalescence occurring.

NAH was then used to reconstruct the original waveform magnitude and the errors were determined. It was found that the 'haystack' spectral shape can be preserved by the nonlinear effects leading to low amplitude-reconstruction errors, whereas a narrow-band spectral shape will become altered and reconstruct very poorly. However, if nonlinear effects become strong due to higher center frequencies, longer propagation distances or higher amplitudes, even the 'haystack' shape will become altered enough to cause poor reconstruction.

Two-dimensional propagation studies were also performed from two point sources, showing differences between linear and nonlinear propagation.

ACKNOWLEDGMENTS

I would like to acknowledge and thank my advisor Dr. Kent Gee for his commitment to helping me learn and succeed and for the many productive discussions related to this and other research projects which helped me to master concepts and ideas. I would also like to thank Dr. Sommerfeldt and Dr. Leishman for serving on my committee, for their dedication to building the acoustics program at BYU and for helping me get involved in research as an undergraduate. They have both also served as great teachers and mentors to me. I would also like to thank the members of my committee for letters of recommendation and for introducing me to other professionals.

I would also like to thank NASA and the Rocky Mountain Space Grant Consortium for financial support, Mark Wochner for his sharing of his code and helping me get started with it, Daniel Jensen for his help with getting started on Marylou4, Dr. David Neilsen for answering some of my Unix questions and the Fulton Supercomputing Lab computer support team for managing the supercomputing cluster.

I would also like to thank my officemates, Ryan Chester, Buye Xu, Ben Shafer and Matt Green for the many useful discussions, sanity checks and other tips. Also, I would like to acknowledge the rest of the BYU Acoustics Research Group. Additionally, I would like to thank Diann Sorensen and Nan Ellen Ah You for their help with scheduling and other assistance with the paperwork.

I also would like to thank my wife Rachel and our son Simon for their love, support and visits to my office. I am also grateful for the support and prayers from many other family members and friends. Finally, I must thank Heavenly Father for giving me the strength and ability to complete this thesis.

Contents

List of Figures

Chapter 1

Introduction

1.1 Introduction

This thesis describes the theory, methods and results of research focused on one part of the complicated problem of understanding, predicting and possibly reducing the noise radiated by finite-amplitude sources such as jets and rockets. The term *finite-amplitude* is common in relevant literature and refers to any acoustic process with disturbances large enough that linear (or infinitesimal-amplitude) models break down and nonlinear effects become significant. This chapter describes the motivation for the research, some of the background information and previous work that has been published, and the present research objectives. It is concluded with a description of the thesis organization.

1.2 Motivation

High-power rockets and jets have become an integral part of the 20^{th} and 21^{st} century. Due to the large amounts of mechanical power required to propel both jets and

rockets, extremely high random pressure fluctuations are produced from complex fluid interactions in the plume region that occur when the flow is supersonic. Because the sound generation process is due to air interactions, these types of sources are known as aeroacoustic sources. Their high levels have a significant impact on the vehicle structure itself as well as the surrounding environment. Acoustically induced vibrations can cause structural fatigue or failure, leading to expensive launch vehicle repairs or remodeling. The acoustic energy also takes on the form of noise pollution as it propagates away from the source. This may increase community annoyance or have a detrimental impact on delicate ecosystems. Additionally, noise levels should be known to ensure adequate hearing protection for those working on or near a vehicle of interest. In fact, studies have shown that as little as a few minutes of exposure to rocket noise only 150 feet from the rocket can have a permanent effect on hearing [1].

Knowledge of the noise generated by a jet or rocket is necessary to properly plan for and estimate these effects. Many studies have been and continue to be performed on a variety of related subjects. Each investigation is an incremental step in understanding, predicting, and ultimately reducing these effects. If the source characteristics were better known, community noise, vibro-acoustic and even computational fluid dynamic (CFD) models could be improved dramatically. The method studied in this research for determining source characteristics of finite-amplitude sources is near-field acoustical holography, abbreviated as NAH.

1.3 Background and Previous Work

Experimental investigations to determine rocket source characteristics and other noise effects started in the early 1950's. Cole *et al.* [2] performed one of the first studies on rocket noise by measuring noise radiation from 14 different rockets varying in size and

thrust, finding the radiation in all cases to be directional. Mayes, *et al.* [3] took near-field and far-field measurements and determined that the noise sources are located 20 or more nozzle diameters downstream from the nozzle exit region. The authors also suggested that the source radiation is in the form of Mach waves[1] due to the supersonic flow but that the location and directivity may be frequency dependent. Potter also published several reports on determining rocket source location [4, 5] and similarly found the major source for sound power generation to be located at least 20 diameters downstream [6]. Several other relevant rocket noise measurements were performed over the next decade in an attempt to characterize and predict far-field rocket noise. They are described extensively by McInerny (see References [7, 8]).

Almost simultaneously, theoretical and analytical models were being developed to understand the aeroacoustic noise-generating mechanisms and to predict radiated sound fields. Lighthill [9, 10] developed fundamental theory on aerodynamic sound, showing that the sound-generation process can be modeled as sets of quadrupoles. Many other researchers have followed in the groundbreaking work of Lighthill. Since the early 1990's, a new subfield of computational fluid dynamics known as computational aeroacoustics (CAA) has developed with its main goal being able to simultaneously model both the aerodynamics and acoustic radiation of aeroacoustic sources. However, due to the complexity of the mathematics involved and the resulting computational power required to solved the relevent equations, current aeroacoustic models are somewhat limited. Significant progress has been made in this field, but as of yet, CAA models have been unable to accurately predict the full broadband noise generation process for all jet and rocket engine configurations (e.g., see Reference [14]). For a

[1]The Mach wave radiation concept is analogous to supersonic structural waves with radiation at some angle. Density visualizations of supersonic flow have also been performed to indicate the Mach wave nature of the radiation of supersonic flow.

more complete discussion of noise generated aerodynamically, see References [15, 16].

These theories have also been combined with data in the form of semi-empirical models and have been used for predicting sound fields. Eldred [11] developed an empirical method for predicting acoustic loads generated by rockets based on measured data in the early 1970's. This method is still frequently used today to predict rocket liftoff noise [12]. More recently, Varnier [13] compared experimental data for basic nozzle configurations and field conditions using the results of a near-field prediction algorithm, finding that many semi-empirical models need some refinement.

Experimental jet noise studies also began around this same time period. Several methods were pursued to visualize jet sources starting in the late 1960's. Lowson and Ollerhead [17] attempted to use shadowgraphs to visualize cold supersonic jets and determined that visual intensity does not necessarily give accurate estimates of sound fields. Fuchs [18] compared three far-field methods, the acoustic "mirror," the acoustic "telescope," and the "polar correlation" technique for determining jet noise source location. He found that in the region where these methods are valid, the spatial resolution is poor, due to the large wavelengths of interest. Laufer *et al.* [19] developed a directional microphone system and showed two separate source producing regions in supersonic jets. Other array processing and beamforming techniques have also been developed with varying success (see e.g. References [20, 21]).

Acoustical measurements of both jet and rocket sources have shown similar trends in their spectral shape. Lower frequency magnitudes increase according to frequency squared, or f^2, up to some center frequency, after which a decay follows according to f^{-2} (see published data in References [11, 33]). The shape resembles a 'haystack' when plotted on a logarithmic scale as shown in Figure 1.1. The spectral center frequency for rocket noise, which depends on size and thrust, ranges from as low as 15 Hz up to around 100 Hz. For jet noise, the peak frequency is usually higher,

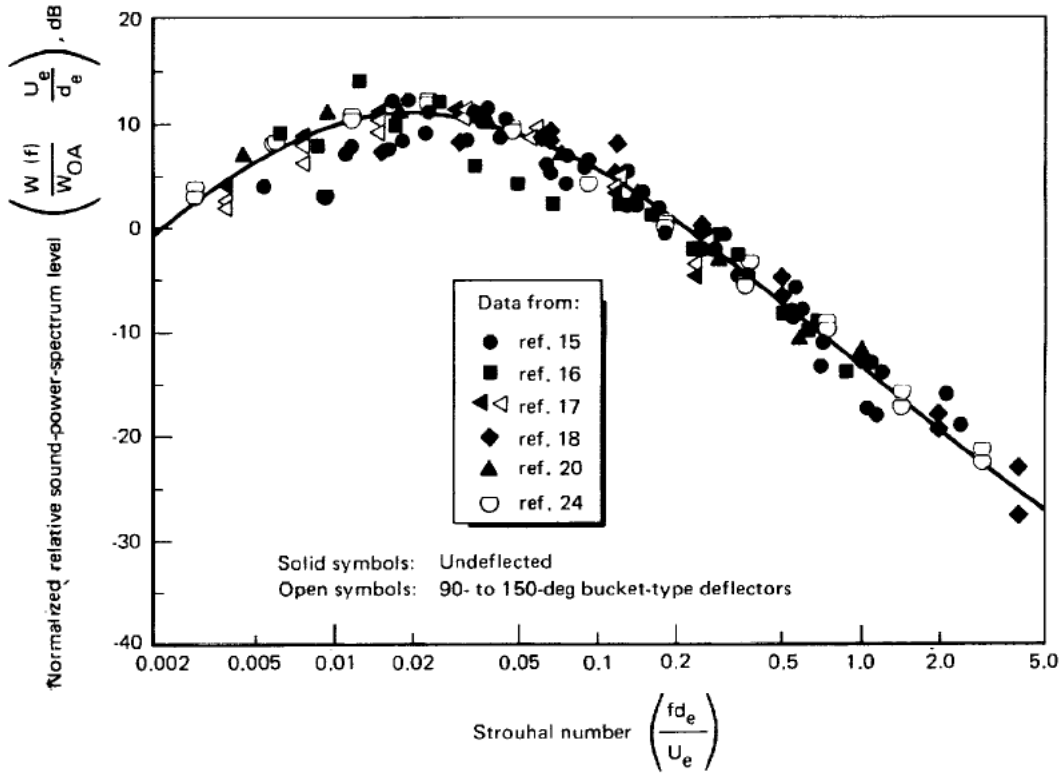

Figure 1.1 Data published in Reference [11] showing the typical 'haystack' spectrum for a number of rockets. As noted in the x-axis label, the Strouhal number is a normalized frequency. The other variables are discussed further in Reference [11].

ranging from 100 to 300 Hz. Although the spectral shape of such aeroacoustic sources has been experimentally well established, the exact mechanisms that cause it are not completely understood.

The imaging technique studied in this research is near-field acoustical holography (NAH). NAH was first developed in the early 1980's and is a form of acoustical holography in that it can predict a three-dimensional sound field based on a two-dimensional pressure measurement [24]. The significance of NAH is in solving the inverse problem or determining the radiation of a source based on a measurement array a short distance from the source (see Figure 1.2). NAH utilizes the basic physics

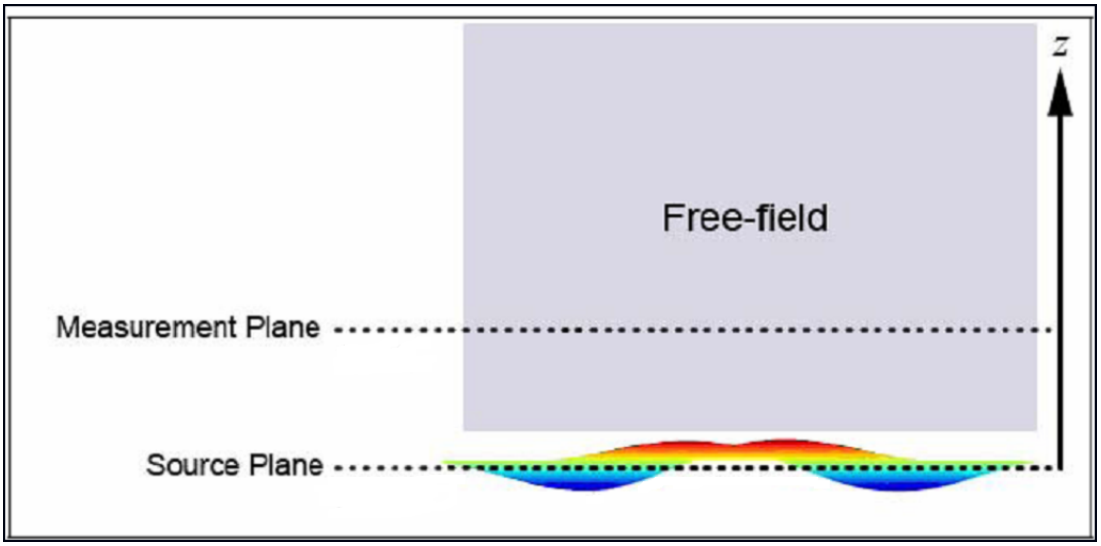

Figure 1.2 A graphical representation of near-field acoustical holography. After measuring the pressure in one plane, the entire pressure field can be determined.

of the wave propagation and radiation with cost-effective methods for accurately performing the signal processing, the specific details of which will be discussed in greater detail in Chapter 3. Several NAH methods have been developed (e.g. see References [26–29]) each with its own strengths and limitations. As a source-imaging method, NAH has been shown to be quite versatile and can reconstruct acoustical

quantities for varying source configurations and types. It has, therefore, become fairly standard for source characterization in many industrial and research applications.

While NAH methods have been successfully applied to many structural sources and even some basic aeroacoustic sources, such as fans and subsonic jets, it cannot be automatically assumed that it would correctly image a supersonic jet or rocket source. The reason for this lies in the high amplitudes of such sources. Both Morfey, *et al.* [32] and Gee, *et al.* [33] showed that some errors in linear propagation algorithms of aircraft noise are due to nonlinear effects. The published overall sound pressure levels (OASPL) from these authors are between 140-150 dB at about 20 meters from the jet. McInerny [35, 36] also found strong evidence of nonlinear propagation in measured rocket noise data, publishing similar OAPSL values for the Titan IV rocket, but at the much greater distance of 820 meters. Since geometrical spreading and air absorption inevitably lowered the amplitude during the propagation, the levels at 20 meters could have easily been on the order of 170 dB. Additionally, peak pressure values were shown to be as much as 15 dB higher than the rms values used for OASPL calculations [35]. Because of the finite-amplitude nature of these sources, a linear technique such as NAH may not accurately image the acoustic source.

1.4 Present Research Objectives

Near-field acoustical holography may become less accurate when applied to a finite-amplitude sound source due to the breakdown of linear assumptions. However, if these errors were studied and characterized, NAH could still be useful in cases where nonlinear effects were known to be negligible. The present research consists of non-linearly propagating several random noise waveforms with varying spectral shapes and center frequencies using a numerical propagation algorithm, applying NAH and

determining the reconstruction errors at multiple propagation distances for low and high amplitudes. The nonlinearities will then be studied and characterized to correlate the nonlinear effects with the reconstruction errors. The main research objective is to show the feasibility of imaging rocket noise using NAH. However, since jets are similar to rockets in their source generating mechanisms and are also finite-amplitude sources, this study is automatically extended to imaging jet noise also.

1.5 Outline

The remainder of this thesis is organized as follows:

- Chapter 2 deals with the theory of linear and nonlinear wave propagation.
- Chapter 3 explains the research methods including the propagation algorithm, the implementation of NAH, as well as the nonlinearity indicators.
- Chapter 4 displays and discusses the nonlinear propagation results.
- Chapter 5 includes the holography results and the reconstruction errors.
- Chapter 6 summarizes the results and concludes this thesis.
- Following the main body of this thesis is a bibliography with a list of references and an appendix with supplemental information.

Chapter 2

Theory: Wave Propagation

Waves are important in describing many physical systems and the manner in which they travel is known as wave propagation. In linear acoustics, the spatial and temporal behavior of a wave can be determined by solving a partial differential equation that is derived from basic conservation laws. The basic solutions for simple coordinate systems can provide much insight into a particular problem, such as the one addressed in this thesis. For this reason, linear wave motion is described in this chapter for plane and spherical waves. For nonlinear acoustics, the same conservation laws are valid, but are more complicated because certain linear assumptions no longer hold. These nonlinear terms that are neglected with linear assumptions cause the behavior to deviate from the linear case. Therefore, the basics of nonlinear acoustic propagation will also be discussed. Additionally, the effects of loss mechanisms are described for both linear and nonlinear propagation.

2.1 Fundamentals of Linear Propagation

For low-amplitude acoustic perturbations, nonlinear or terms higher than first-order are not significant and subsequently neglected. When these terms are not accounted for in expanded versions of the basic conservation equations and losses are neglected, the linear, lossless, homogeneous wave equation can be derived,

$$\nabla^2 \mathbf{p} = \frac{1}{c_0^2} \frac{\partial^2 \mathbf{p}}{\partial t^2}, \tag{2.1}$$

where c_0 is the small-amplitude sound speed and $\mathbf{p}$ is the complex acoustic pressure. Neglecting nonlinear terms inherently assumes that the amplitude of the occurrence is relatively small, and that the temperature fluctuations due to the sound waves are negligible. Ignoring temperature changes would result in a constant sound speed. For many applications, the temperature changes are indeed so small that this assumption is valid. In the next sections, geometrical spreading will be addressed with the assumption of constant sound speed c_0 as well as a homogeneous, isotropic medium.

2.1.1 Plane Waves

The complex solution to the wave equation in Cartesian coordinates takes on the form of

$$\mathbf{p} = \mathbf{A} e^{j(\omega t - \vec{k} \cdot \vec{r})}, \tag{2.2}$$

where $\mathbf{A}$ is a constant and $\vec{k}$ is the propagation vector, which has components in each of the Cartesian coordinates. The magnitude of $\vec{k}$ is the acoustic wavenumber and is equal to the angular frequency divided by the speed of sound, $k = \omega / c_0$.

Waves that have this mathematical form are called plane waves and are the simplest form of propagating waves. Plane waves propagate with constant amplitude and phase through a medium in some direction, dictated by the direction of $\vec{k}$ [38].

If the solution is assumed to be time harmonic, the $e^{j\omega t}$ time dependence can be factored out of the wave equation to yield the Helmholtz equation,

$$\nabla^2 \mathbf{p} + k^2 \mathbf{p} = 0. \tag{2.3}$$

This is also equivalent to taking the spectral Fourier transform of the wave equation. The spatial pressure distribution can then be determined for a given time-harmonic excitation by solving the Helmholtz equation.

In the context of acoustic radiation and propagation, it becomes convenient to know a spatial distribution of the field in terms of its wave numbers. For this, the continuous spatial Fourier transform can be used, which is defined as

$$\mathbf{P}(k) = \frac{1}{\sqrt{2\pi}} \int_{-\infty}^{\infty} \mathbf{p}(x) e^{-jkx} dx, \tag{2.4}$$

where x is a spatial coordinate and $\mathbf{P}(k)$ is known as the angular spectrum or plane wave spectrum. The inverse transform is then defined as

$$\mathbf{p}(x) = \frac{1}{\sqrt{2\pi}} \int_{-\infty}^{\infty} \mathbf{P}(k) e^{jkx} dk. \tag{2.5}$$

For most applications of the Fourier transform, the data are discretely sampled and the discrete-time Fourier transform (DFT) must be used. It is defined using a summation instead of an integral according to

$$\mathbf{P}[l] = \frac{1}{N} \sum_{n=0}^{N-1} \mathbf{p}[n] e^{j2\pi ln/N}, \tag{2.6}$$

where [ ] denotes a discrete sequence, l is the k-space sample number corresponding to the continuous variable k, n is the spatial sample number corresponding to the continuous variable x and N is the number of samples in the sequence. A fast implementation of the DFT is known as the fast Fourier transform and requires that N be a multiple of two for maximum computational efficiency [39].

2.1.2 Spherical Waves

When an acoustic source exhibits spherical symmetry, it becomes convenient to express the wave equation in the spherical coordinates r, θ and ϕ. Using separation of variables, the Helmholtz equation becomes

$$\nabla^2 R(r)\Theta(\theta)\Phi(\phi) = k^2 R(r)\Theta(\theta)\Phi(\phi). \tag{2.7}$$

The Laplacian operator can be expanded in spherical coordinates to obtain

$$\sin^2\theta \frac{1}{R}\frac{d}{dr}r^2\frac{dR}{dr} + \frac{1}{\Theta}\sin\theta\frac{d}{d\theta}(\sin\theta)\frac{d\Theta}{d\theta} + \frac{1}{\Phi}\frac{d^2\Phi}{d\phi^2} + k^2r^2\sin^2\theta = 0. \tag{2.8}$$

so that the ϕ variables are grouped together. Because the sum of the set must equal zero, the ϕ-dependent portion must equal a negative constant as

$$\frac{1}{\Phi}\frac{d^2\Phi}{d\phi^2} = -n^2, \tag{2.9}$$

and the rest of the equation must equal that positive constant $+n^2$, with the requirement that the constant n^2 ensures a 2π periodic solution in ϕ. Solving Equation 2.9 again leads to complex exponentials, now of the form $e^{\pm jn\phi}$. The rest of the equation can now be separated again to achieve

$$\frac{1}{R}\frac{d}{dr}r^2\frac{dR}{dr} + k^2r^2 + \frac{1}{\Theta}\frac{1}{\sin\theta}\frac{d}{d\theta}(\sin\theta)\frac{d\Theta}{d\theta} - \frac{n^2}{\sin\theta^2} = 0, \tag{2.10}$$

where the first portion is dependent only on r while the second portion is dependent only on θ. Again, they must equal a constant, C. Using the substitution $\eta = \cos\theta$, the θ-dependent portion can be written as the familiar associated Legendre differential equation,

$$(1-\eta^2)\frac{d^2\Theta}{d\eta^2} - 2\eta\frac{d\Theta}{d\eta} + (m(m+1) - \frac{n^2}{1-\eta^2})\Theta = 0, \tag{2.11}$$

where $C = m(m+1)$. The solutions are the associated Legendre functions [41]

$$\Theta(\theta) = P_m^n(\cos\theta). \tag{2.12}$$

The remaining portion of Equation 2.10 must be manipulated further in order to find a solution. By multiplying by R and making the substitution $r = \zeta/k$, the equation can be written as

$$\frac{d^2R}{d\zeta^2} + \frac{2}{\zeta}\frac{dR}{d\zeta}[\zeta^2 - m(m+1)]\frac{R}{\zeta^2}. \tag{2.13}$$

The solutions to this equation are spherical Hankel functions, which can be written in terms of spherical Bessel functions of the first and second kind as

$$h_m^{(1)}(\zeta) = j_m(\zeta) + jn_m(\zeta), \tag{2.14}$$

which represents incoming waves and

$$h_m^{(2)}(\zeta) = j_m(\zeta) - jn_m(\zeta), \tag{2.15}$$

which represents outgoing waves [40]. The total solution for an outgoing complex pressure wave can then be written as

$$\mathbf{p}(r, \theta, \phi) = h_m^{(2)}(kr)P_m^n(\cos\theta)\cos n\theta. \tag{2.16}$$

This can be simplified by defining a set of orthonormal functions called spherical harmonics [41], as

$$Y_{mn}^1(\theta) = P_m^n(\cos\theta)\cos n\theta e^{-jm\theta} \tag{2.17}$$

to obtain a more compact solution written as

$$\mathbf{p}(r, \theta, \phi) = h_m^{(2)}(kr)Y_{mn}^1(\theta). \tag{2.18}$$

For the complete solution, a summation over the indices m and n is necessary [42].

For a spherical wave with symmetry in the axial (polar) and azimuthal (circumferential) angles, the solution is only dependent on the radial distance r. This forces the integer coefficients n and m to be zero, therefore reducing $\mathbf{p}$ for the outgoing case to

$$\mathbf{p} = \frac{\mathbf{A}}{r}e^{j(\omega t - kr)}. \tag{2.19}$$

This result shows the general dependence of $1/r$ for spherical waves.

This $1/r$-dependence can also be obtained by determining the average power radiated by a source. The average acoustic power is defined as the surface integral of the acoustic intensity, $\mathbf{I}$, dotted with the outward normal vector, $\mathbf{n}$, or

$$\mathcal{P}_{ave} = \int_S \mathbf{I} \cdot \mathbf{n} dS. \tag{2.20}$$

By letting S be a spherical surface of radius r, the integral reduces to $4\pi r^2$, or the area of the sphere, and makes the intensity, which is related to the squared pressure, inversely proportional to r^2 [48]. This $1/r$ decay for spherical waves is often called spherical spreading because it physically represents a radial spreading of energy as the wave propagates. Many waves travel as spherical waves if the source appears to be sufficiently compact (i.e. is small compared to wavelength).

An analogy to the plane wave spectrum can be defined for spherical waves and therefore is called the spherical wave spectrum, $\bar{\mathbf{P}}_{mn}$ [57]. It is defined in terms of spherical harmonics according to

$$\bar{\mathbf{P}}_{mn} = \int p(r_0, \theta, \phi) Y_m^n d\Omega, \tag{2.21}$$

where $d\Omega$ is $sin\theta d\theta d\phi$. This essentially decomposes the pressure at r_0 into its spherical wave components. The inverse transform can be found using orthogonality of the basis functions Y_m^n, to get

$$\mathbf{p}(r, \theta, \phi) = \sum_{n=0}^{\infty} \sum_{m=-n}^{n} \bar{\mathbf{P}}_{mn} Y_m^n, \tag{2.22}$$

which is actually a double Fourier series.

Strictly speaking, Equations 2.21 and 2.22 are not Fourier transforms at all. Rather, the "forward transform" is equivalent to determining spherical harmonics coefficients and the "inverse transform" is a spherical harmonic series expansion. For this reason, the "forward transform" must actually be derived from the "inverse

transform" using orthogonality of the spherical harmonic basis functions and not vice versa [41]. However, the variables m/r_0 and n/r_0 are somewhat analogous to k_x and k_y in that they are both eigenvalues that decompose the field [57]. For this reason and to be consistent with the literature, the terms *transform* and *spherical wave spectrum* will still be used.

2.1.3 Losses

For the previous derivations, it has been assumed that the acoustic propagation has been lossless. When losses are included, the Helmholtz equation can be altered merely by making the wave number complex according to

$$\mathbf{k} = k - j\alpha, \tag{2.23}$$

where α is the appropriate absorption coefficient. The complex wavenumber then causes both dispersion and attenuation.

For many acoustic propagation problems, losses play an important role in the decay process of the wave. Thermal conduction and viscosity effects as well as molecular relaxation are the major loss mechanisms which are significant for propagation in air. Thermoviscous absorption, also known as classical absorption or modified classical absorption[1], is the superposition of the absorption due to thermal conductivity and that due to viscosity. The modified classical absorption coefficient, which is also known as the diffusivity of sound δ, is defined as

$$\alpha_c = (\frac{\omega^2\eta}{2\rho_0 c^3})(\frac{4}{3} + \frac{\mu_B}{\mu} + \frac{\gamma - 1}{Pr}), \tag{2.24}$$

where η is the coefficient of shear viscosity, γ is the ratio of specific heats, μ is the

[1]Classical absorption actually assumes that the bulk viscosity is zero whereas modified classical absorption includes the bulk viscosity [48].

shear viscosity, μ_B is the bulk viscosity and Pr is the Prandtl number [38]. A semi-empirical form of Equation 2.24 is

$$\alpha_c = 1.84^{-11} f^2, \tag{2.25}$$

which is valid at T=293 K and atmospheric pressure [43]. This equates to a frequency-dependent decay rate, causing higher frequencies to decay much faster than lower frequencies (see Figure 2.1).

Molecular relaxation effects are due to the molecules in the fluid being excited by an acoustic perturbation. Energy is transferred from translational motion to rotational and vibrational motion. If there is enough time for the molecule to return to its equilibrium state before the next perturbation, the absorption increases logarithmically with frequency. This concept is known as the relaxation time and its inverse is the relaxation frequency. If there is not enough time to return to equilibrium, the molecule is considered "frozen". The absorption is then constant above the relaxation frequency. When the interactions between the processes are small, the cumulative effects of each loss mechanism can be added to obtain an overall absorption coefficient[2] α_{tot} [42] and is shown in Figure 2.1. The major contributors to absorption of audible frequencies in the lower atmosphere are the molecular relaxation due to nitrogen and oxygen.

2.2 Fundamentals of Nonlinear Propagation

As previously mentioned, nonlinear effects become important when temperature fluctuations are not negligible. Since sound traveling through a fluid medium is an adiabatic process, the sound speed, c, is temperature-dependent, and continuous tempera-

[2] α is typically in units of nepers per meter and can be converted to decibels per meter by multiplying by 8.686.

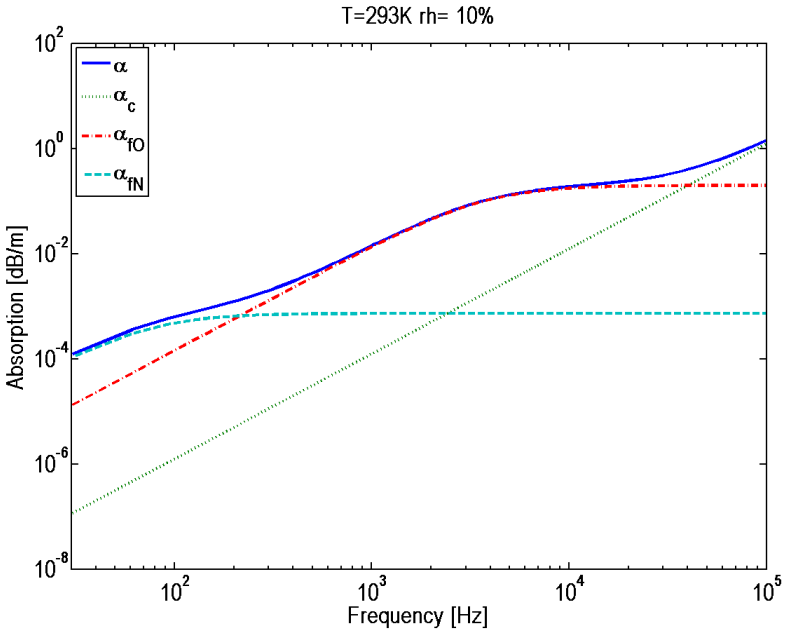

Figure 2.1 Classical and molecular relaxation absorption in dB per meter.

ture changes cause the instantaneous speed of sound to also change continuously [44]. Since the velocity of the wave is a more convenient quantity to consider when determining the change in sound speed, a normalized version is often used. This quantity is known as the acoustic Mach number, ϵ, and is defined as the acoustic velocity divided by the small-amplitude sound speed, u/c_0. For a reference value, a Mach number of 0.1 equates to 177 dB *re* 20 μPa for plane waves. Additionally, properties of the fluid contribute to the amount of nonlinear effects that occur. These are accounted for in a factor known as the coefficient of nonlinearity β, which for an ideal gas is $(1+\gamma)/2$. Since $\gamma = 1.402$ for air, this equates to $\beta = 1.201$ for air [44].

The nonlinear wave equation is very complicated and in general does not have an analytical solution. However, several of the important effects can be shown for simple cases. Also, a series of approximations can be made which allow for solutions in specific cases that still effectively demonstrate many of the fundamental nonlinear

acoustics phenomena.

2.2.1 Time-domain Effects

Waveform Steepening

The instantaneous sound speed for acoustic plane waves in an ideal gas is dependent on the particle velocity u and β according to

$$c = c_0 + \beta u \tag{2.26}$$

for second-order or quadratic nonlinearities. When the velocity magnitude is high, the sound speed deviates from c_0. However, due to the oscillatory nature of waves, the speed of sound will either increase or decrease according to the relative phase of the wave. In other words, the regions of condensation or fluid compression will travel faster than c_0, while the regions of rarefaction or fluid expansion will travel slower than c_0. Figure 2.2 shows the changing sound speed for a single period of a sine wave. As the waveform propagates in space, it becomes more and more distorted. This effect is known as waveform steepening.

Shock Formation

As the waveform continues to steepen, some portion will eventually become triple-valued, a physically impossible phenomenon since acoustic waves are compressional. Instead of the waveform becoming triple-valued, a discontinuity known as a shock is formed. For an initially monofrequency wave, the necessary propagation distance to form a shock is known as the shock formation distance, where a shock is defined as when the rise from a trough to a crest takes less than one-tenth of the period of the wave. The shock formation distance is calculated for plane and spherical waves

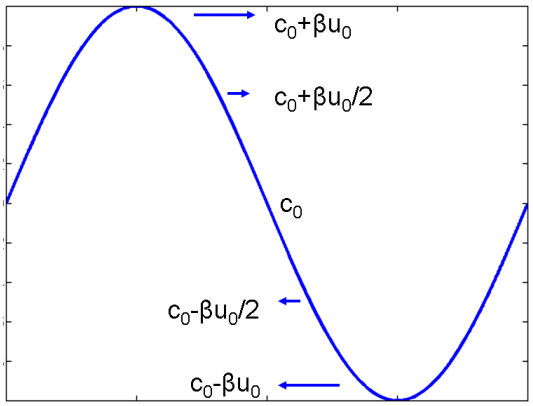

Figure 2.2 The positive portions of a waveform will travel faster than the negative portions. This shift in sound speed is important when amplitudes are large and causes waveform steepening.

respectively according to

$$\bar{x} = \frac{1}{\beta \epsilon k} \tag{2.27}$$

and

$$\bar{r} = r_0 e^{\frac{1}{\beta \epsilon k r_0}}, \tag{2.28}$$

where r_0 is some distance where the monofrequency amplitude is known. From these equations, it is apparent that shocks form quicker for greater Mach numbers (i.e. higher amplitudes), higher frequencies and higher coefficients of nonlinearity. Table 2.1 lists the shock formation distance for several frequencies and Mach numbers in air.

For convenience, distance is often normalized by the shock formation distance to create a dimensionless distance σ defined as $x/\bar{x}$ for plane waves. A value of σ less than one would represent any distance before the shock has formed, known as the preshock region, while $\sigma > 1$ would represent distances larger than a shock formation distance. Once formed, the shock rise time will continue to decrease until it simultaneously overtakes the trough ahead of it and is overtaken by the crest behind it. This occurs

Table 2.1 Shock formation distance for several frequencies and Mach numbers in air.

Frequency [Hz]	Mach Number	$\bar{x}$	$\bar{r}$ $(r_0 = 1)$
100	0.05	9.1 m	8873 m
1000	0.05	0.91 m	2.5 m
100	0.1	4.5 m	94 m
1000	0.1	0.45 m	1.57 m

at $\sigma > \pi/2$ after which the shock amplitude will begin to decrease [45]. After a sine wave has traveled the equivalent of three shock formation distances (i.e. $x = 3\sigma$), the waveform will have become a sawtooth wave (see Figure 2.3) The sawtooth wave will continue to decay at a rate different than linear waves.

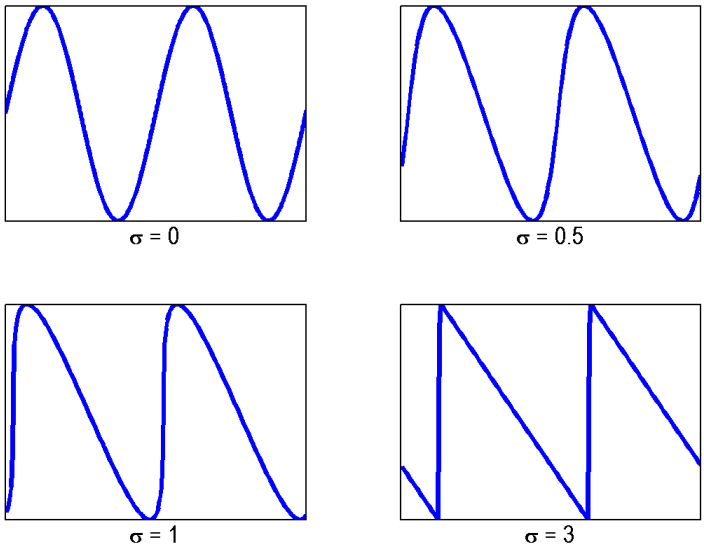

Figure 2.3 A sine wave will steepen up and form a shock due to the amplitude-dependent sound speed. Eventually, the sine wave will become a sawtooth wave.

It must be noted that a waveform will steepen in opposite directions depending

on whether the representation is in space or time, where a moving time frame is generally used (see Subsection 2.2.3 for more details). Figure 2.3 is a representation of steepening in time whereas figure 2.2 is a representation of steepening in space.

For broadband, random noise waveforms, the waveform steepening and shock formation will also occur based on the principles just mentioned. However, since the pressure amplitudes are random, areas of local maxima will experience more steepening than other portions of the waveform. The actual location and amplitude of these maxima cannot be predicted and therefore the term shock formation distance is no longer straightforward. Additionally, since measured shocks are not exactly discontinuous, McInerny defines a shock as occurring when the time for a pressure rise from a minimum to a maximum is less than one tenth of the average period of the overall sound pressure waveform [36]. This is known as the shock rise time and the distance required to accomplish this rise is known as the shock thickness [46].

After a shock forms, its speed becomes dependent on the pressure on both sides of the shock according to

$$U_{sh} = c_0 + \beta \frac{p_a + p_b}{2\rho_0 c_0}, \tag{2.29}$$

where p_a and p_b are the pressure right behind and right in front of the shock respectively [45]. Therefore, the points behind the shock will 'catch up' with the shock, while points ahead of it will be 'overtaken.' Because of this, all shocks do not travel at the same speed and slower shocks may eventually be 'overtaken' by other shocks traveling at a faster speed. This concept is known as shock coalescence. As seen in Equation 2.29, changes in the pressure amplitude due to geometrical spreading or losses will play an important part on the amount of shock coalescence that occurs.

2.2.2 Frequency-domain Effects

Harmonic Generation

A steepened waveform will also have perceivable changes in the spectral information of the wave. If the wave begins as a sinusoid, steepens and forms a shock, the Fourier series components will change from one term to possibly an infinite number of terms. The energy can be thought to have 'leaked' from the fundamental frequency to its harmonics as shown in Figure 2.4. This is a consequence of Fourier's theorem, as

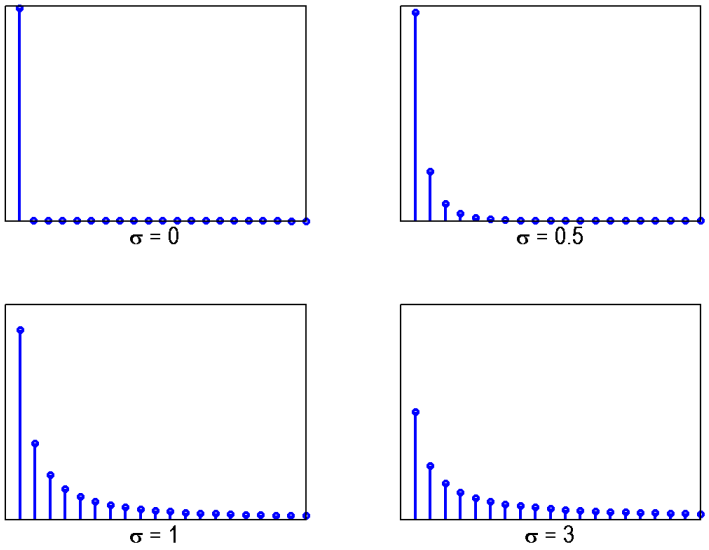

Figure 2.4 The Fourier components of the time waveforms shown in Figure 2.3. The higher-order harmonics become non-zero as the waveform steepens and forms a shock.

more and more harmonics are needed to represent a sine wave experiencing distortion [44]. Furthermore, the amplitudes begin to approximately follow a $1/f$ curve once significant waveform steepening has occurred. This can be observed in the Fourier series solution of a sawtooth wave which has the form

$$f_{sawtooth}(x) = \frac{1}{2} - \frac{1}{\pi}\sum_{n=1}^{\infty}\frac{1}{n}\sin(\frac{n\pi x}{2T}), \tag{2.30}$$

where n is the harmonic number and T is the period [47].

For a broadband waveform, the harmonic generation will also occur and Fourier's theorem will still apply. However, since all frequencies are already present as opposed to a just single tone, the harmonic generation causes a constant f^{-2} decay at all high frequencies as with the monofrequency case only not at just discrete harmonics [69]. This equates to a high frequency roll-off that is uncharacteristic of geometrical spreading or atmospheric absorption. Therefore, a high frequency decay proportional to f^{-2} in a random noise spectrum may indicate waveform steepening and therefore nonlinear propagation [32].

Additionally, the spectral content can be affected by shock coalescence. When a faster shock overtake a slower shock, the waveform may lose a zero-crossing, as shown in Figure 2.5. This loss effectively lowers the characteristic time scale which is related to the center frequency of the spectrum [54]. This is made manifest in the spectrum

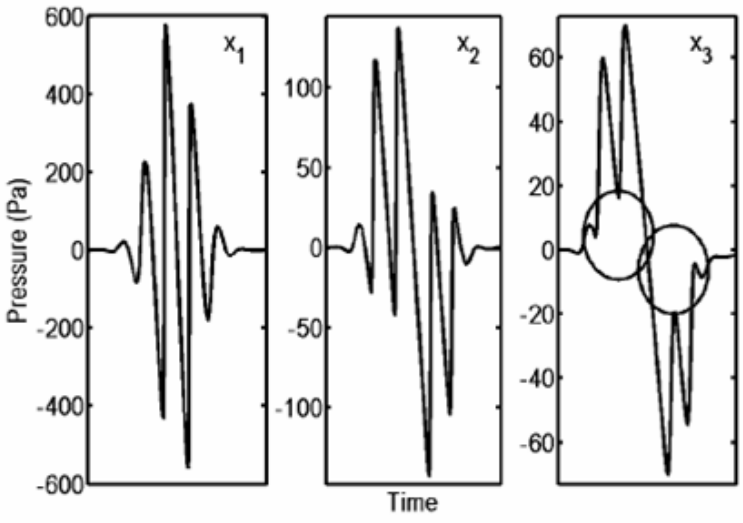

Figure 2.5 A shock traveling at a faster speed can cause a loss in zero-crossings as it begins to overtake another slower shock. The loss in zero-crossings causes a downward shift in the center frequency and a f^2 rise at low frequencies.

by an increase in lower frequency energy according to f^2 [49] and a downward shift in the center frequency [50]. These two factors, a low-frequency dependence on f^2 and a downward shift in center frequency, can be an indication of shock coalescence and therefore nonlinear propagation[3].

In general, nonlinear propagation will act as a frequency filter and will shape the spectrum of a broadband random noise signal. The spectral shape, however, is generally dependent on amplitude and distance.

2.2.3 Analytical Solutions

Burgers Equation

The generalized Burgers equation is the simplest model equation that accounts for nonlinearities, losses and geometrical spreading in one dimension[4]. The generalized form of the Burgers equation is expressed as

$$(\frac{\partial \mathbf{p}}{\partial r} + \frac{m}{r}\mathbf{p} \mp \frac{\delta}{2c_0^3}\frac{\partial^2 \mathbf{p}}{\partial \tau^2}) = \pm\frac{\beta \mathbf{p}}{\rho_0 c_0^3}\frac{\partial p}{\partial \tau}, \tag{2.31}$$

where m is 0, 1/2 or 1 for plane, cylindrical and spherical waves respectively, τ is known as the retarded time and δ is the diffusivity of sound [45]. The retarded time is a moving reference time frame defined as $t - dx/c$, where dx is some spatial step. This reduces to

$$(\frac{\partial \mathbf{p}}{\partial r} \mp \frac{\delta}{2c_0^3}\frac{\partial^2 \mathbf{p}}{\partial \tau^2}) = \pm\frac{\beta \mathbf{p}}{\rho_0 c_0^3}\frac{\partial \mathbf{p}}{\partial \tau} \tag{2.32}$$

for plane waves. Many finite-amplitude propagation algorithms are based on the Burgers equation (e.g. see References [50, 51]).

[3] A downward shift in center frequency can also be caused by near-field effects in jet noise and care must be taken to separate these two effects (see Reference [66]).

[4] The Burgers equation was originally developed to model turbulence but is also a model of other nonlinear phenomena.

Burgers Equation Solutions

For the lossless plane wave case with a monofrequency source, the solution to the Burgers equation takes on the form

$$\mathbf{p} = \mathbf{p}_0 \sum_{n=1}^{\infty} \frac{2}{n\sigma} J_n(n\sigma) \sin n\omega\tau, \tag{2.33}$$

where n is the harmonic number [45]. This solution was developed by Fubini and carries his name. The Fubini solution is valid in the preshock region for values of $\sigma \leq 1$. The pressure solution is clearly in terms of Fourier components B_n, with each component's amplitude defined in terms of Bessel functions according to

$$B_n = \frac{2}{n\sigma} J_n(n\sigma). \tag{2.34}$$

As σ approaches 1, more n^{th}-order Bessel functions are non-negligible, and therefore more Fourier components are included in the solution, as shown in Figure 2.6.

Since the Fubini solution is only valid up to the formation of the shock, it carries no information about the behavior of the actual shock itself. Fay developed a solution that is valid in the region where $\sigma \gg 3$ and includes losses[5]. The pressure is defined as

$$\mathbf{p} = \mathbf{p}_0 \sum_{n=1}^{\infty} \frac{2/\Gamma}{\sinh[n(1+\sigma)/\Gamma]} \sin n\omega\tau, \tag{2.35}$$

where Γ is the Gol'dberg number that will be discussed in the following subsection [45]. Again the solution is an infinite sum of harmonics with the amplitude now defined as

$$B_n = \frac{2/\Gamma}{\sinh[n(1+\sigma)/\Gamma]}. \tag{2.36}$$

The harmonic amplitudes normalized by the initial amplitude of the fundamental are shown Figure 2.7.

[5]These two solutions were thought to contradict each other until Blackstock showed that each is valid in a different region [52].

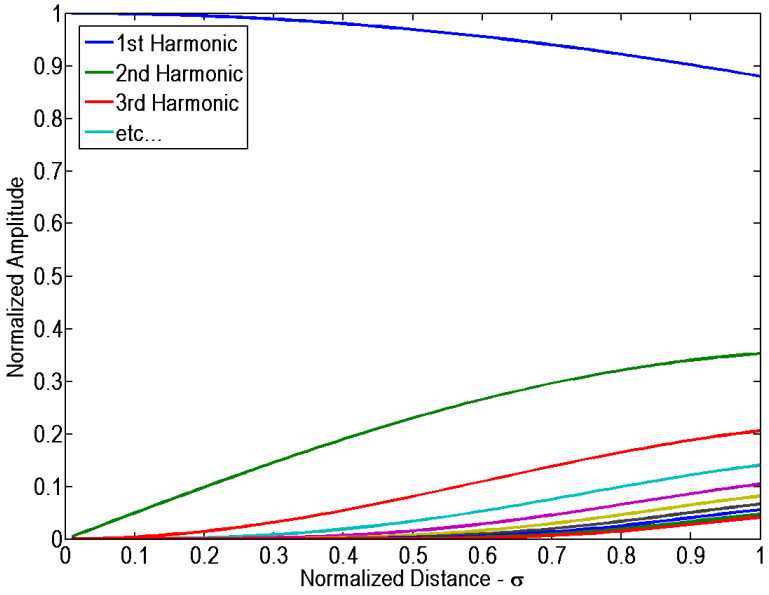

Figure 2.6 The normalized amplitudes of the Fourier series components as defined by the Fubini solution (Equation 2.33) for the preshock region. As σ approaches one, more components are non-zero and contribute to the solution.

2.2.4 Losses

Because nonlinear effects tend to increase energy at high frequencies and absorption tends to decrease energy at high frequencies, it is possible that given enough absorption and a low enough amplitude, waveform steepening will not be able to significantly occur. The parameter Γ, known as the Gol'dberg number, can give an indication of the relative strength of waveform steepening compared to absorption. It is defined as

$$\Gamma = \frac{l_a}{\bar{x}}, \tag{2.37}$$

where l_a is the absorption length defined as $1/\alpha_c$. If $\Gamma \ll 1$, the absorption acts to negate the nonlinear effects, whereas if Γ is greater than unity, the waveform can significantly steepen and form a shock before absorption effects become significant [45]. The Fay solution is therefore not valid where the initial Γ is less than one.

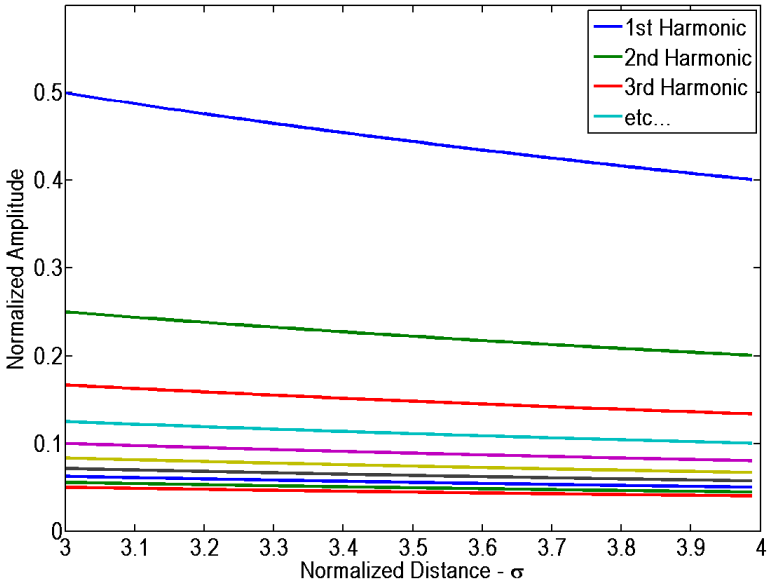

Figure 2.7 The normalized amplitudes of the Fourier series components from $\sigma = 3$ to $\sigma = 4$ as defined by the Fay solution (Equation 2.35). The harmonic amplitudes are normalized according to the initial amplitude of the fundamental.

Additionally, losses can be important for shocks. Attenuation caused by absorption can slow down shock formation and affect shock speed, thereby changing the propagation behavior (see Equation 2.29). The expression for shock thickness, shown here as

$$h = \frac{2\delta \ln(9)}{\beta u_b}, \tag{2.38}$$

where u_b is the acoustic velocity behind the shock, demonstrates the battle between dissipation and nonlinearity. Nonlinearity tends to steepen the compression wave which decreasing the shock thickness, whereas dissipation tends to spread it out and therefore increase h [46].

Chapter 3

Research Methods

The methods used in this research are described in the following order. First, the methods for creating and propagating four broadband waveforms are explained. Next, the reconstruction implementation using NAH is derived. Finally, the theory behind the nonlinearity indicators used is extensively described.

3.1 Numerical Methods

In order to accurately propagate the signals of interest, a numerical propagation algorithm that accounts for nonlinearities and losses was used. Four broadband random noise waveforms were created and input into the algorithm.

3.1.1 Propagation Algorithm

The numerical algorithm used for propagation was recently developed by Wochner [54] and builds off the work by Sparrow and Raspet [55]. Wochner's algorithm solves an extended Navier-Stokes equation set, comprised of conservation equations. They are

defined here in two dimensional form: the equation of continuity,

$$\frac{D\rho}{Dt} + \rho\nabla \cdot \mathbf{v} = 0, \tag{3.1}$$

the Navier-Stokes equation or conservation of momentum,

$$\rho\frac{D\mathbf{v}}{Dt} = -\nabla p + \nabla(\mu_B \nabla \cdot \mathbf{v}) + \mu \sum_{ij} \mathbf{e_i} \frac{\partial \phi_{ij}}{\partial x_j}, \tag{3.2}$$

the entropy balance equation, which is necessary for shock formation and propagation,

$$\rho\frac{Ds_{fr}}{Dt} + \sum_{\nu} \frac{\rho}{T_\nu} c_{v\nu} \frac{DT_\nu}{Dt} - \nabla \cdot (\frac{\kappa}{T}\nabla T) = \sigma_s, \tag{3.3}$$

and the relaxation equation,

$$\frac{DT_\nu}{Dt} = \frac{1}{\tau_\nu}(T - T_\nu). \tag{3.4}$$

In the above equations, D/Dt is the total derivative, ρ is the fluid density, $\mathbf{v}$ is the velocity vector, μ and μ_B are the shear and bulk viscosities, $\mathbf{e}_i$ is the unit vector in the i^{th} direction, ϕ_{ij} is the rate of shear tensor, s_{fr} is the frozen entropy, T is the absolute temperature, κ is the coefficient of thermal conduction, $c_{v\nu}$ is the specific heat constant of the ν-type molecule, σ_s is the entropy source term, and T_ν and τ_ν are the apparent vibration temperature and relaxation time of the ν-type molecule.

The temporal and spatial variables are grouped together to form a matrix of this form

$$\frac{\partial \mathbf{w}}{\partial t} + \frac{\partial \mathbf{F}}{\partial x} + \frac{\partial \mathbf{G}}{\partial y} = \mathbf{H}, \tag{3.5}$$

where $\mathbf{w}$ is a matrix of the time-dependent variables, $\mathbf{F}$ is a matrix of the x-dependent variables, $\mathbf{G}$ is a matrix of the y-dependent variables, and $\mathbf{H}$ is a matrix of the

remaining source-like terms. More specifically, $\mathbf{w}$, $\mathbf{F}$ and $\mathbf{G}$ are

$$\mathbf{w} = \begin{pmatrix} \rho \\ \rho u \\ \rho v \\ \rho s_{fr} \\ \rho T_{0_2} \\ \rho T_{N_2} \end{pmatrix}, \qquad \mathbf{F} = \begin{pmatrix} \rho u \\ \rho u^2 \\ \rho uv \\ \rho u s_{fr} \\ \rho u T_{0_2} \\ \rho u T_{N_2} \end{pmatrix}, \qquad \mathbf{G} = \begin{pmatrix} \rho v \\ \rho uv \\ \rho v^2 \\ \rho v s_{fr} \\ \rho v T_{0_2} \\ \rho v T_{N_2} \end{pmatrix}, \tag{3.6}$$

where T_{N_2} and T_{O_2} are the vibration temperatures of nitrogen and oxygen respectively, and $\mathbf{H}$ is defined in Reference [54]. Acoustic pressure is then found using the van der Walls form of the equation of state,

$$\Re\{\mathbf{p}\} = c^2[(\rho - \rho_0) + \frac{\gamma - 1}{2\rho_0}(\rho - \rho_0)^2 + \frac{\rho\beta T}{c_p}(s_{fr} - s_{fr_0})], \tag{3.7}$$

which relates the pressure, density and entropy of a perturbation. This set of equations can also be simplified to one dimension by removing the y-component of the velocity and generalized for arbitrary geometrical spreading. More specific details regarding the derivation of the equation set can be found in Reference [56].

Equation 3.5 is then solved for using finite-difference approximations for a given set of initial and boundary conditions. Appendix A describes the basic theory behind solving partial differential equations using finite-difference approximations including definitions of the terms stencil and CFL number.

A weighted essentially non-oscillatory (WENO) scheme was used to solve for the spatial derivatives (see Reference [54] for WENO references). The specific WENO method used is a three stencil scheme with each stencil containing three points equating to fifth-order accuracy in space. Each stencil is then weighted with the center stencil receiving the highest weighting, while smoothness factors are calculated to determine how continuous the points are. For portions with discontinuities, the smoothness factors approach zero for that stencil and force the weighting functions to zero,

thus allowing the estimate of the derivative to maintain finite by using the remaining stencils with non-zero smoothness factors. This type of scheme requires the CFL number to be less than one half. The WENO scheme is able to stably propagate discontinuities and therefore will not go unstable when shocks with close to infinite slopes form. However, this ability comes at a large computational cost and also inherently includes an initial smoothing effect which limits the useable frequency content of broadband waveforms. Figure 3.1 shows the effect of the smoothing on a broadband time waveform while Figure 3.2 shows the smoothing effect on the waveform's third-octave band spectrum. Frequencies above 2 kHz experience significant smoothing

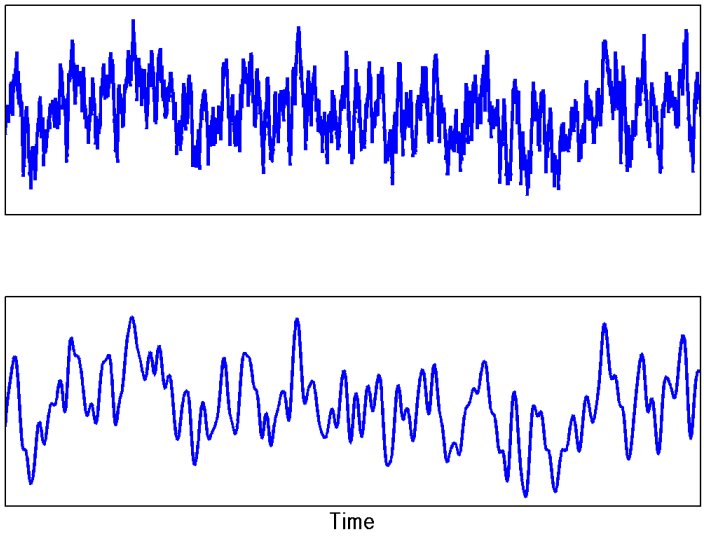

Figure 3.1 A broadband noise time waveform before (top) and after (bottom) being smoothed by the WENO scheme. Some high frequency content is lost (see Figure 3.2).

by the WENO scheme and therefore are not accurate. It must also be noted that the WENO method does not have trouble creating higher frequencies that occur with nonlinear distortion. Rather, the initial smoothing is the WENO scheme's attempt to ensure adequate smoothness of the broadband input.

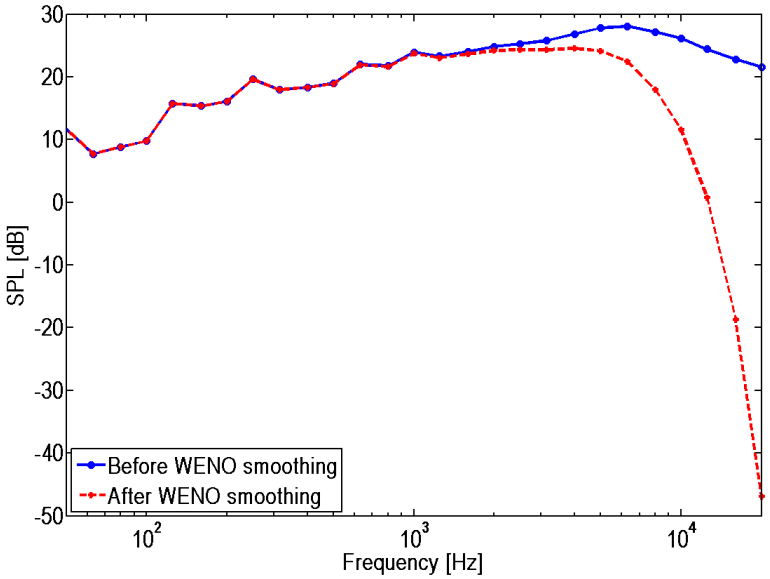

Figure 3.2 A random noise waveform spectrum before and after the WENO smoothing. The smoothing causes an artificial decay in frequencies above about 2 kHz.

The temporal portion of Equation 3.5 is solved using a third-order Runge-Kutta scheme. This is accomplished by using a series of three approximations of the time solution, each dependent on the last iteration with the final approximation being the actual estimate. Each iteration uses the spatial derivative information and therefore triples the number of computations required per iteration. For more advanced details about the algorithm theory, development and numerical verification, see Reference [54].

An absorbing boundary condition was implemented using a Gaussian decay. Mathematically, the decay is described as

$$Q(\psi) = e^{\frac{ln(2)(\psi-\psi_0)^2}{\alpha^2}}, \tag{3.8}$$

where ψ is the spatial variable, α is the Gaussian half-width, ψ_0 is the location of the center of the distribution and Q is the variable to which the boundary condition is applied. This absorbing boundary condition was applied to all of the variables

starting 100 points away from the actual boundary with α set to the value $600d\psi$, where $d\psi$ is the discretization step size in ψ. This allows for virtually no numerical reflection, but did increase the number of points required in the domain.

A point source was implemented with the following Gaussian distribution for the one-dimensional case

$$Ae^{\frac{ln(2)(x-x_0)^2}{\alpha^2}}, \tag{3.9}$$

where A is the amplitude, and x is equivalent to ψ in equation 3.8, with an additional $(y-y_0)^2$ term included for two-dimensional propagation. This is a common approximation of a point source in numerical simulations and is used to overcome the infinite slope requirement of an actual point source. This approximation also has its limitations, especially when used to propagate broadband noise. If the Gaussian half width is too small and α is less than about half a wavelength, the source will not be able to generate low frequencies. On the other hand, if α is large compared to the spatial discretization step dx, then that wavelength will also not be able to be resolved. For this reason the Gaussian half width value of $10dx$ was used as a middle point for the broadband propagation.

Several of the weaknesses of this algorithm are as follows. First, the algorithm is computationally expensive, especially with the addition of the y-dimension. Without the use of parallel processing, only very small domains can be used with high accuracy. Since a large number of time iterations is required for high resolution in the frequency domain, this again equate to extremely long run times. This required the use of a supercomputing cluster which, due to its size and utilization, crashed more frequently than one would desire. Second, the amplitude of the waveform cannot be specified explicitly beforehand. This means that a trial run must be performed to ensure that the amplitude is correct. The amplitude also changed depending on the input parameters. Third, the algorithm smooths out broadband waveforms losing

the initial high frequency content as previously discussed. Finally, the exact stability requirements are not well known due to the complexity of the finite-difference scheme and the set of equations that is being solved. The algorithm can also go unstable if the absorbing boundary condition parameters are not sufficient to force the amplitude to zero at the boundary, causing numerical reflections to occur. These factors can all work together to cause the algorithm to go unstable with only minor adjustments of the numerical parameters.

3.1.2 Source Terms

Several random noise time waveforms were then created, two with a characteristic 'haystack' spectral shape and two with a more narrow spectrum similar to narrow-band noise. This was done to test the effect of the spectral shape on propagation and reconstruction. Furthermore, two peak frequencies of 100 and 500 Hz were additionally chosen for each of the spectra to study the effect of the center frequency. These were chosen not to exactly match the center frequencies for jets and rockets spectra but as estimates that allow for reasonable computations[1].

A block diagram of the waveform generation procedure is shown in Figure 3.3 and is described as follows: An $N = 2^{16} = 65,536$ array of random numbers was generated with an rms value, or standard deviation of 1. It was sampled at 500 kHz and transformed to the frequency domain. The respective spectral shapes were attained by multiplying the spectrum with a filter function, W, with the spectral shape defined as

$$W = \begin{cases} f^m & , \quad f < f_c \\ f^{-m} & , \quad f > f_c \end{cases} \tag{3.10}$$

[1]Extremely long run times would have been required in order to get good frequency resolution below 100 Hz.

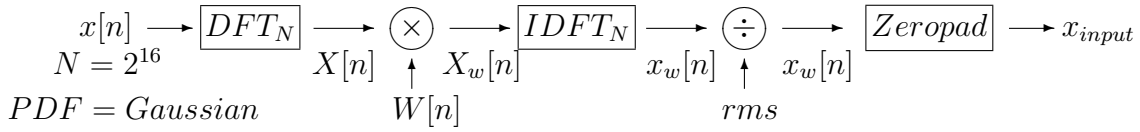

Figure 3.3 Block diagram for creating the input waveforms. The filter W is shown in Equation 3.10.

where $m = 1$ for the 'haystack'-shaped filter and $m = 2$ for the narrowband-noise-like filter. This equates to f^2 and f^4 dependence for the respective power spectra. The spectrum was then transformed back to the time domain and divided by the standard deviation to maintain the rms value of unity. The waveform was then padded with zeros to ensure that only zeros and not the actual waveform exited the domain during the run. This equates to a moving reference frame that allows for analysis of the entire 2^{16} point waveform at each virtual microphone. The waveforms were then input into the domain by defining the amplitude, A, from Equation 3.9, at each time iteration, i, in terms of the input waveform amplitude according to

$$A_i = \mathcal{B}x_i, \tag{3.11}$$

where x_i is the i^{th} point of the input waveform. $\mathcal{B}$ acted then as a scaling factor to allow for varying the actual amplitude of the run.

To avoid confusion of which waveform was used, a simpler naming convention will be used and is shown in Table 3.1. Narrow-band and third-octave-band spectra for the four waveforms are shown in Figures 3.4, 3.5 , 3.6 and 3.7. The third-octave-band filter changes the apparent slopes of the narrowband spectra because the energy is being spread out over larger bins, effectively increasing the rise and decreasing the decay and causing the symmetry of the spectra to disappear.

As mentioned in Chapter 1, the peak pressures for rockets have been measured 10

Table 3.1 List of Input Waveforms

Spectral Shape	Center Frequency [Hz]	Simplified Name
f^2	100	waveform 1
f^2	500	waveform 2
f^4	100	waveform 3
f^4	500	waveform 4

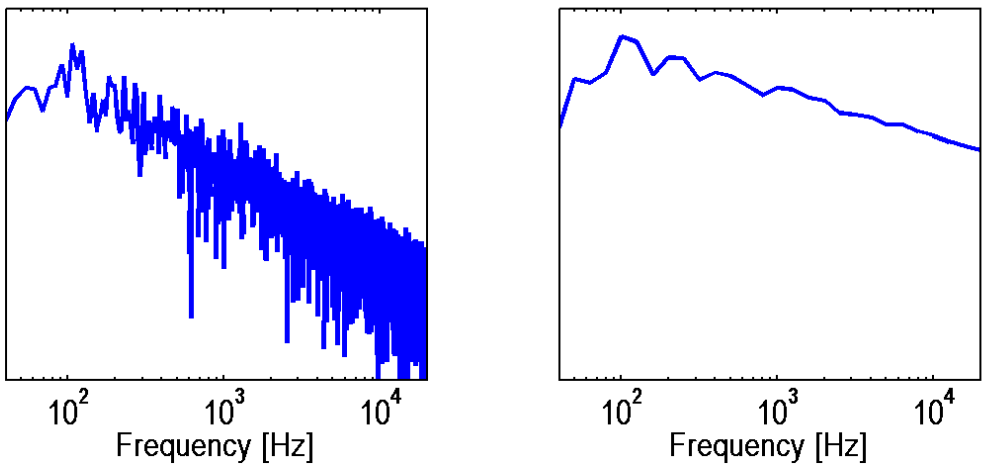

Figure 3.4 Waveform 1 in narrow- and third-octave bands. The f^2 rise now appears to be proportional to f^3 while the f^{-2} decay appears to be proportional to f^{-1}.

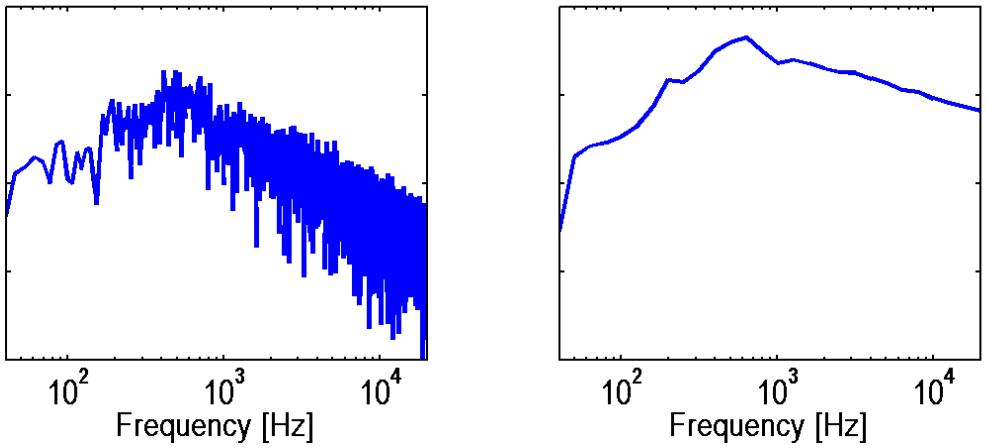

Figure 3.5 Waveform 2 in narrow- and third-octave bands. The f^2 rise now appears to be proportional to f^3 while the f^{-2} decay appears to be proportional to f^{-1}.

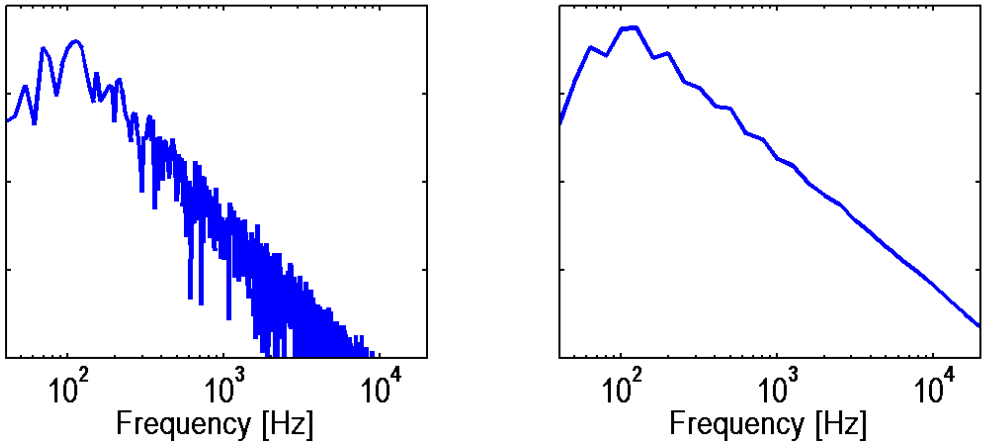

Figure 3.6 Waveform 3 in narrow- and third-octave bands. The f^4 rise now appears to be proportional to f^5 while the f^{-4} decay appears to be proportional to f^{-3}.

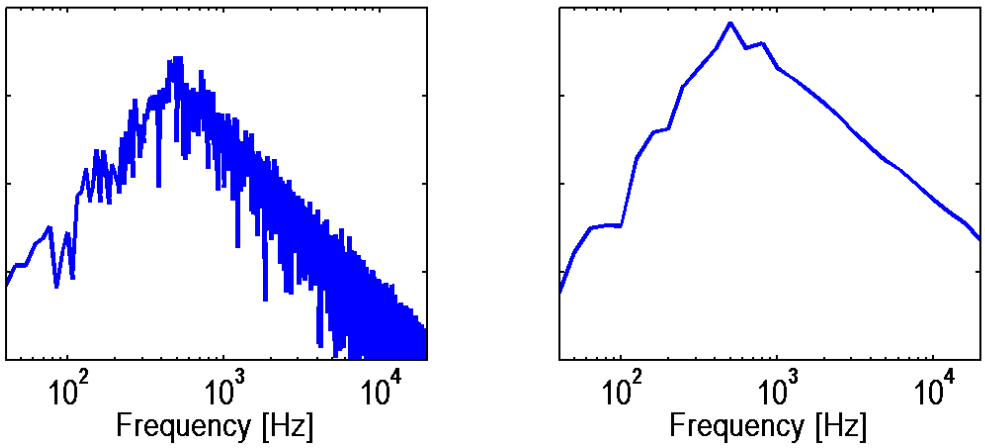

Figure 3.7 Waveform 4 in narrow- and third-octave bands. The f^4 rise now appears to be proportional to f^5 while the f^{-4} decay appears to be proportional to f^{-3}.

to 15 dB higher than the OASPL. The crest factor, $\mathcal{C}$, is used to determine this and is defined in decibels as

$$\mathcal{C} = 20log_{10}(\frac{p_{max}}{p_e}), \tag{3.12}$$

where p_{max} is the maximum pressure and p_e is the effective or rms pressure. Table 3.2 shows the crest factors for waveforms 1-4. This shows crest factors slightly lower than

Table 3.2 Crest factor for the generated waveforms

Waveform	Crest Factor [dB]
1	9.8
2	11.0
3	7.4
4	10.3

rocket noise crest factors published in Reference [35]. This means that real rocket noise would have slightly higher peak amplitudes and therefore more nonlinear effects than the waveforms used for this research.

3.1.3 Implementation

The algorithm was modified only slightly for the one-dimensional studies. Both spherical spreading and full atmospheric absorption were included with the source arbitrarily placed 0.02 meters into the domain. Because of the spherical spreading constraint, the domain itself was set 0.3 meters from the origin in order to keep the backward propagating portion from becoming too large due to the backward spreading. This equated to the source being located 0.32 meters from the origin with absorbing boundary conditions at each end of the domain. Virtual microphones were equally spaced throughout the domain and recorded the pressure at each time step. The pressure data at each virtual microphone were then output as an ASCII file at the completion of the run. Small-domain jobs were run on a desktop PC[2] while large-domain jobs were run on a single node of the Marylou4 supercomputing cluster housed in the Brigham Young University Fulton Supercomputing Laboratory[3].

In order to have high accuracy with numerical schemes, small temporal and spatial sizes must be used. The spatial step would correspond to a finite number of points per wavelength and the temporal step is defined by the CFL number, sound speed and spatial step size (see Appendix A). However, due to computational constraints, realistic discretization steps must be chosen that correspond to achievable domain size for a given processor and a practical run time. In order to ensure that the numerical parameters chosen, shown in Table 3.3, produced an accurate estimate of the solution, two test cases were performed and compared against the Fubini and Fay solutions.

The Fubini solution is valid for lossless propagation from a monofrequency source in the pre-shock region (see Chapter 2). The spatial discretization size was set to

[2]Intel®Pentium®D processor at 3.2 GHz with 3.5 GB RAM

[3]Dell 1955 Blade Cluster with 1260 Dual Core Intel EM64T processors at 2.6 GHz (2520 cores) and 618 compute nodes with a total of 5,040 GB total memory (8 GB/node)

Table 3.3 Numerical parameters chosen for the propagation algorithm

Frequency [kHz]	Point per Wavelength	CFL Number
20	200	.49

8.57e-5 meters, which, as shown in Table 3.3, corresponds to 200 points per wavelength at 20 kHz, while the temporal step size was set to 1.225e-7 seconds. With 100,000 spatial steps and 150,000 temporal steps, this equated to a useable domain size of 2.5 meters and a run time of 41 hours on the supercomputer. The normalized decibel amplitude of the first five harmonics for the exact and numerical solutions in the pre-shock region are plotted in Figure 3.8. The errors are small except at short distances

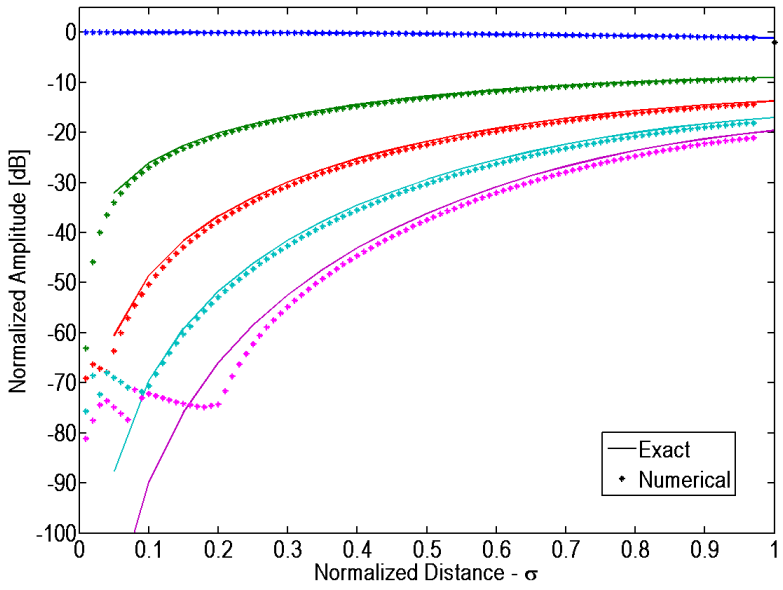

Figure 3.8 The Fubini solution is compared to the solution from the numerical scheme for the first 5 harmonics in the preshock region. Errors at low frequencies are insignificant because they are over 60 dB down from the fundamental.

for the higher harmonics. These errors however are insignificant because they are over 60 dB less than the fundamental. The good agreement for all the harmonics up

to $\sigma = 1$ signify that the parameters chosen are adequate.

For propagation distances corresponding to $\sigma > 3$, the exact solution is that of a sawtooth with the harmonic amplitudes defined by Fay (see Chapter 2). For the same conditions but including thermoviscous losses, the harmonic amplitudes are shown in Figure 3.9. The errors are slightly higher, but still no greater than 1 dB. If the

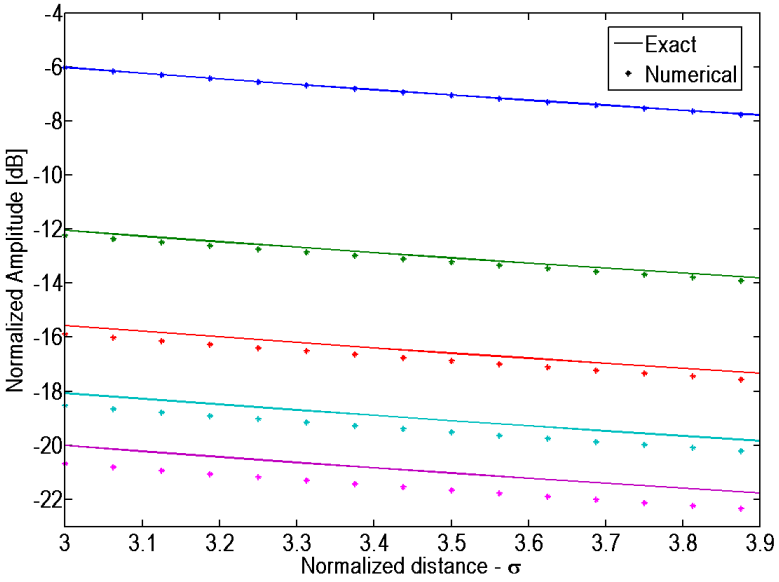

Figure 3.9 The Fay solution is compared to the solution from the numerical scheme for the first 5 harmonics in the sawtooth region. Errors for the higher harmonics are increasing, but are still within 1 dB.

discretization sizes were made smaller, the error would decrease (see Appendix A), but would increase necessary computational power and run time. However, it must be noted that even with smaller step sizes, the results will still have some estimation error for the higher harmonics due to the finite number of points per wavelength[4] resulting in possible error in the rise-time of the shocks. However, the discretization step sizes chosen allow for a good compromise between realizable run time and domain

[4]The errors in harmonic amplitude as a function of points per wavelength was thoroughly studied in [54]

size with reasonably low numerical estimation error.

3.2 Near-field Acoustical Holography

Near-field acoustical holography (NAH) was developed in the early 1980's by Maynard and Williams [24] as a source-imaging method based on wave number decomposition and the discrete Fourier transform (DFT). The power of NAH typically comes from placing microphones close enough to the source so as to capture evanescent mode information. In this manner, the resolution issues faced in traditional acoustic holography are eliminated [25]. Several methods for implementing NAH have been developed to broaden its use and refine its accuracy (see e.g. References [26–29]). All NAH methods, however, are based on solutions to the linear Helmholtz equation. This section explains basic original theory as well as the theory for the NAH implementation used in this research.

3.2.1 Planar NAH

NAH is based on the linear theory. The Helmholtz equation, described in Chapter 2 and restated here for convenience

$$\nabla^2 \mathbf{p} + k^2 \mathbf{p} = 0, \tag{3.13}$$

is obtained from the linear, lossless wave equation when a time harmonic signal is assumed. Since the Helmholtz equation has no time dependence, it only describes the spatial behavior of a linear, time harmonic pressure wave. The Helmholtz equation can be solved to find a unique solution given a set of boundary conditions. For plane waves in a free field, the function that describes the propagation of the wave in the z-direction is $e^{-jk_z z}$, where z is the propagation distance. The difference between the

pressure field at two different planes is then merely the phase difference $e^{-jk_z(z-z_h)}$. For NAH applications, this function is known as a propagator. Therefore, if the pressure field is measured in a plane, it can be used to determine the pressure field at any other plane in the field by multiplying the k-space spectrum by the propagator and then inverse transforming back into the spatial domain. This method has great utility due to the efficiency of the fast Fourier transform. Other acoustical quantities such as particle velocity and intensity can also be computed by merely changing the propagator.

The utility of NAH, however, lies in techniques for implementing the above procedure. To allow for greater spatial resolution, the initial pressure field must be measured close to the source so as to capture any evanescent modes which decay out quickly. This plane is referred to as the hologram plane. The plane where the pressure is reconstructed is then called the reconstruction plane. In most NAH application, k-space filtering or matrix regularization is required to prevent any signal noise from being amplified by the application of the propagator and to guarantee the uniqueness of the solution [30, 57, 58].

3.2.2 Spherical NAH

For imaging a spherical source, spherical region enclosing a source or spherical array of transducers, the natural convention is to use NAH in spherical coordinates. In spherical k-space[5], the pressure in one spherical plane at r_h can be equated to another spherical plane at r using a ratio of spherical Hankel functions, remembering that the spherical Hankel function contains the radial (r-dependent) information. This equates

[5]Again, the convention spherical k-space is used because of its analogy to k-space. (See Chapter 2)

to

$$\bar{\mathbf{P}}_{mn}(r) = \frac{h_n^2(kr)}{h_n^2(kr_h)}\bar{\mathbf{P}}_{mn}(r_h). \tag{3.14}$$

The complete solution in spherical coordinates comes from taking the inverse spherical wave transform and rearranging to get

$$\mathbf{p}(r) = \sum_{n=0}^{\infty} \frac{h_n^2(kr)}{h_n^2(kr_h)} \sum_{m=-n}^{n} Y_n^m(\theta,\phi) \int \mathbf{p}(r_h) Y_n^m(\theta',\phi') e^{jm\phi'} d\Omega'. \tag{3.15}$$

When axial symmetry is assumed, only the $n = 0$ axial mode is required and forces azimuthal symmetry ($m = 0$). This leads to $h_0^2(x) = e^{-jx}/x$, $P_0^0 = 1$ and $Y_0^0 = \sqrt{1/4\pi}$ [61]. Using these simplifications

$$\int_0^{\pi}\int_0^{2\pi} \mathbf{p} Y_0^0 sin\theta d\phi d\theta = 2\sqrt{\pi}\mathbf{p}, \tag{3.16}$$

and the pressure at the reconstruction plane then becomes

$$\mathbf{p}(r) = \mathbf{p}(r_h)\frac{r_h}{r}e^{jk(r_h - r)}. \tag{3.17}$$

This again shows the general $1/r$ spreading as seen in Chapter 2. Therefore the pressure magnitude at some distance r from an axisymmetric source is just the pressure magnitude at some distance r_h multiplied by a ratio of the distances. This shows that NAH for spherical geometries simplifies down to the spherical spreading problem for an axisymmetric source and can be performed entirely in the time domain. This also causes the near-field requirement to be relaxed and the k-space filtering to be unnecessary.

Furthermore, since the Fourier transform of a constant times some function is the constant times the Fourier transform of the function, this NAH reconstruction can actually be applied in the frequency domain as well. Therefore, in order to determine the effect of the propagation on the spectrum, this reconstruction was applied in the frequency domain for the 1-D simulations.

3.2.3 Application to Aeroacoustic Sources

Traditionally, NAH has been used solely to determine source characteristics of vibrating structures, which are highly correlated spatially. The fact that the rockets and jets are aeroacoustic sources raises the additional question of whether NAH can image aeroacoustic sources, which can be highly uncorrelated. This problem was answered in the affirmative when Lee, *et al.* successfully imaged an axial cooling fan [59]. More interesting is the attempted application of NAH to subsonic jets [30,31], which are infinitesimal in amplitude. More recently, the application of NAH to nonlinear, aeroacoustic problems has become a topic of increased interest in an effort to improve current jet and rocket noise models (see Reference [37]).

3.3 Nonlinearity Indicators

Nonlinearity indicators are functions that are able to detect whether certain nonlinear relationships are present in a set of data. The indicators used for this research can be separated into frequency and time domain indicators, each with its own utility and assumptions.

3.3.1 Time Domain - Statistics

When nonlinear effects exist, distortion occurs and time domain analysis can yield insight into the effects of the distortion. Furthermore, since most acoustic noise processes are Gaussian or near-Gaussian random data, any changes or variation in the distribution will be manifested using statistical analysis and could indicate nonlinear effects such as quadratic phase coupling. Higher-order statistical properties can be especially useful to determine changes in Gaussian or near-Gaussian behavior.

The probability density function (PDF) therefore becomes a useful tool when

performing statistical analysis. A probability density function, $\tilde{p}(x)$, is defined as the probability which is assigned to the set of points satisfying a desired inequality [60]. Therefore, the integral of the PDF over all possible values must equal unity. An estimate of the PDF is defined as

$$\tilde{p}(x) = \frac{\mathcal{N}}{Lw_{bin}}, \tag{3.18}$$

where L is the length of the sequence, w_{bin} is the width of the histogram bin, and $\mathcal{N}$ is the number of values in that bin. This was the method used for estimating the PDF in this research.

First, the shape or relative shape of the PDF can help indicate nonlinear effects. A random noise waveform with some distribution will generally maintain its shape if its propagation is linear and losses are small. If waveform steepening and shock formation are occurring, the PDF will change from Gaussian to non-Gaussian because the phase coupling causes the probability of the existence of energy in some frequency bin to be related to its "mother" frequency and not be completely random. Outliers, or points with high or low values, are emphasized by the nonlinear distortion and steepen up more quickly than the other portions of the waveform. The steepened portions of the waveform alter the PDF because the transition from negative to positive is more dramatic, while the transition to the next trough region becomes more linear. Once shocks have formed, the PDF changes again. The attenuation of the shocks suppress outliers and the distribution tends toward a uniform probability [69]. The changing of the PDF of random noise that is initially Gaussian or near-Gaussian to a more uniform distribution would therefore be an indication of the presence of shock formation.

Next, the use of central moments can help indicate nonlinear propagation. The first two central moments are the mean, μ =E[x], where E[ ] notates the expected

value, and the variance $\sigma^2 = \mathrm{E}[(x-\mu)^2]$. The variance is a measure of the variability and is related to the acoustic power of the signal. Its square root, the standard deviation, is the root-mean square (rms) value. These quantities are useful descriptions of a PDF.

Higher-order statistical properties though can be especially useful for determining if the PDF has changed shape. The third central moment is known as the skewness coefficient and is a measure of the asymmetry of a distribution. The definition[6] for the sample skewness coefficient used in this research is

$$S = \frac{1}{n-1}\sum_{i=1}^{n}\frac{(x_i-\mu)^3}{\sigma^3}, \tag{3.19}$$

but other forms have also been used [35]. A symmetric distribution has a skewness value of zero. If the PDF has a long tail to the right, the skewness coefficient is positive. It is similarly negative if the tail is to the left [68].

The sample kurtosis coefficient is the fourth central moment and can be defined as

$$K = \frac{1}{n-1}\sum_{i=1}^{n}\frac{(x_i-\mu)^4}{\sigma^4}. \tag{3.20}$$

The kurtosis coefficient is a measure of the relative peakedness of the distribution and $K = 3$ for a Gaussian distribution. Other definitions of kurtosis normalize the Gaussian value to zero, but are not common for this type of application. A kurtosis value above three would represent a more 'pointy' PDF while a value less than three would indicate a broader distribution with narrow tails [68].

A histogram of an array of random numbers is shown in figure 3.10 with the skewness and kurtosis values numerically confirming its Gaussian shape. The mean and standard deviation are also listed for convenience. Figure 3.11 on the other hand shows a skewed waveform. Both the skewness and kurtosis values have shifted away

[6] McInerny does not include the $1/(n-1)$ in her definition. However, the inverse dependence on

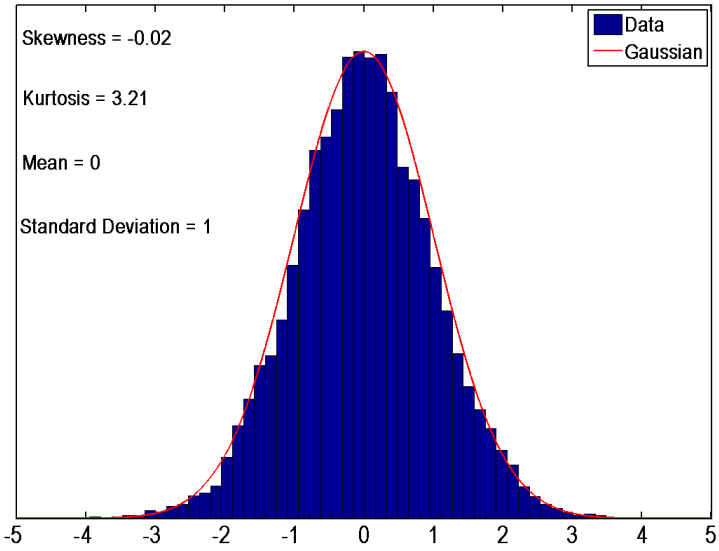

Figure 3.10 A histogram plot for an array of random numbers plotted against a Gaussian curve. The first four standard moments are shown for the array of random numbers, with the skewness and kurtosis values confirming numerically its Gaussian nature.

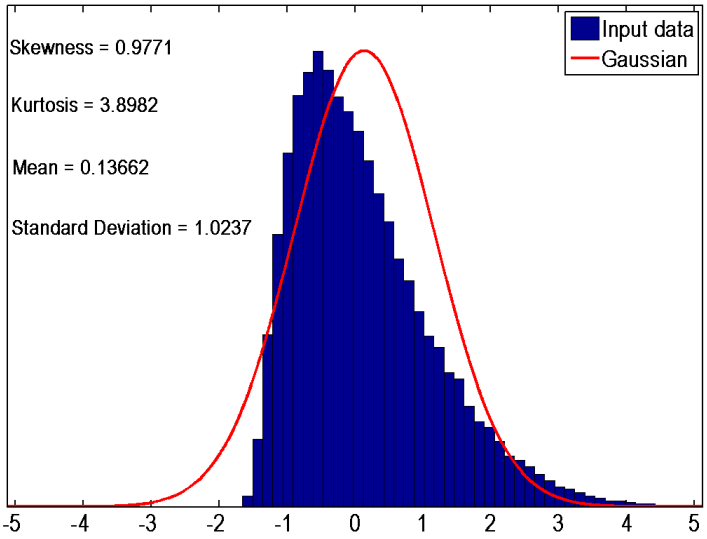

Figure 3.11 A histogram plot for an array of numbers with a skewed distribution plotted with a Gaussian curve. The skewness and kurtosis values indicate that the distribution is not symmetric and bell-shaped, and therefore non-Gaussian.

from zero and three. These higher-order moments can then be used to show if a PDF is non-Gaussian.

McInerny [35], however, showed that higher-order statistical analysis is more sensitive to nonlinear effects (i.e.shocks) if applied to the time derivative of the data, not the data themselves. Since a random noise waveform will have a random phase distribution that is Gaussian, the time derivative of that random noise waveform, which basically reveals the phase, will also be Gaussian and any variation from Gaussian behavior will be magnified through taking the derivative. This is more obvious in that a shock is a discontinuity with a theoretical slope that approaches infinity [36]. A slightly skewed or peaked distribution in time would become an extremely skewed and peaked distribution when analyzing the time derivative of the data. As the waveform becomes dominated by shocks, the slopes in the regions between the shock will all approach the same negative value. The slope in the shock regions, which are relatively few compared to the total number of points in the waveform, will remain large, theoretically approaching infinity. This will lead to a distribution dominated by a close-range set of negative numbers and a small number of extreme positive outliers.

A time derivative can be easily estimated using a first-order forward or backward finite-difference approximation[7] (see Appendix A for more details on finite-difference theory). Equation 3.21 shows a first-order forward approximation of the pressure time derivative at some point x_n and time t_i with a time step Δt equal to the sampling period [70].

$$\frac{\partial p(x_n, t_i)}{\partial t} = \frac{p(x_n, t_{i+1}) - p(x_n, t_i)}{\Delta t} \tag{3.21}$$

Since the time slope right at the shock is very large compared to the slope right before

n is necessary to remove the influence of the signal length.

[7]A center-difference approximation could be used, but would be inaccurate when dealing with non-smooth or discontinuous waveforms due to the use of a three-point stencil.

and right after the shock, a large peak in the time-derivative would clearly show the location and relative strength of the shock.

Equation 3.21 was implemented to find the time derivative for all statistical analysis performed in this research. Since the equation is only valid for data points [1...N-1], the value at the last data point is omitted for convenience. Also, the Δt does not reflect any change in the statistics and is therefore removed for consistency in all analyses performed. Finally, in terms of notation, a subscript 'd' will be used when analyzing statistics (e.g. S_d) to signify that the analysis is of the data's time derivative, not the data themselves.

3.3.2 Frequency Domain - Bispectrum

In nonlinear propagation, frequency components interact to create sum and difference frequencies, causing quadratic phase coupling to exist (see Chapter 2). The most accepted technique to detect quadratic nonlinearity is using bispectral analysis, which has been used to detect nonlinear relationships in various fields such as plasma physics [63], medicine [64] and ocean noise [65]. More recently, the bispectrum has been used to analyze nonlinear effects in military jet aircraft noise by Gee, *et al.* [62].

The bispectral density (BSD) or bispectrum is defined as

$$S_{xxx}(f_1, f_2) = \lim_{T\to\infty} \frac{1}{T} E[X(f_1)X(f_2)X^*(f_1 + f_2)], \tag{3.22}$$

where $X(f)$ is the Fourier transform of the signal $x(t)$ and * denotes the complex conjugate. For finite-length signals, the limit can be removed while still obtaining a good approximation of the BSD, as is commonly done for power spectral density calculations [67]. Thus, the BSD is similar to the power spectral density (PSD) except that it decomposes the third-order moment of the signal (related to the skewness, see Subsection 3.3.1) at a given bifrequency $(f_1 + f_2)$, instead of the mean-square power or

variance (a second-order moment) at a given frequency f_1. The BSD for a Gaussian signal is by definition zero. Therefore, if the BSD of an acoustic signal is non-zero, that could indicate nonlinear propagation.

However, a more physical interpretation of the BSD can be obtained by a normalization called the bicoherence. The bicoherence is defined as

$$b(f_1, f_2) = \frac{|S_{xxx}(f_1, f_2)|}{\sqrt{Z(f_1, f_2) S_{xx}(f_1 + f_2)}}, \tag{3.23}$$

where

$$Z(f_1, f_2) = \lim_{T \to \infty} \frac{1}{T} E[|X(f_1) X^*(f_2)|^2]. \tag{3.24}$$

by Gee, *et al.* [62], even though the original definition by Kim and Powers [63] is equivalent to squaring both sides of Equation 3.23. This leads to a value between 0 and 1, showing its analogous nature to the coherence function. For a periodic signal, $b(f_1, f_2) = 0$ would indicate no fraction of the energy at f_1, f_2 is due to quadratic nonlinearities, whereas $b(f_1, f_2) = 1$ indicates that all the energy at that sum frequency is due to quadratic phase coupling. The quantitative interpretation for random noise signals is less straight-forward due to the possibility of multiple bifrequecies interacting at a single sum frequency. However, the qualitative aspects are still present in that bicoherence values close to zero indicates low quadratic phase coupling [66].

The bicoherence was computed for this research using an ensemble-averaging technique, with 2^{11} samples per block. A Hamming window was applied to each ensemble, with a 95% overlap between blocks. This large overlap was used because of a limitation on the number of points in the waveform and allowed for more averages, even though other block sizes have been recommended (see Reference [62]).

3.4 Summary

In summary, a WENO-based propagation algorithm was used for the nonlinear propagation with four random noise inputs. The input waveforms were created to test the effect of center frequency and spectral shape on the propagation and reconstruction. For the reconstruction, spherical NAH simplifies down to removing the spherical spreading for the one-dimensional case. For analysis, bispectral and higher-order statistical methods will be used to determine nonlinear behavior in the propagation.

Chapter 4

Results: Nonlinear Propagation

Propagation results are discussed for one- and two-dimensional propagation. Time waveform, statistical and bispectral analysis were used to determine the relative amount of nonlinear effects on the results in one dimension. The results in two dimensions are analyzed using spatial derivatives and by comparing against the linear case.

4.1 One-dimensional Propagation

Using the numerical parameters specified in Table 3.3, the broadband waveforms discussed in Chapter 3 were then used as input to the 1-D propagation algorithm. The algorithm ran for 180,000 time iterations, equating to a total run time of approximately two days. Ninety nine virtual microphones were placed every 0.08 meters starting at the source.

Each waveform was propagated for a low-amplitude 50 dB benchmark case and three high-amplitude cases. The OASPLs recorded at the source for the high-amplitude cases were 143, 158, and 166 dB. The 143 dB amplitude would be more typical of a jet,

whereas the 166 dB amplitude would be more typical of a rocket. These amplitudes do not by any means encompass the amplitudes for all jets and rockets. Likewise, the finite propagation distance and small bandwidth, limited by computational restraints, does not come close to representing the actual distances that the noise propagates for real jet/rocket spectra[1]. However, the general trends that occur with increasing amplitude, propagation distance, and center frequency will be discussed, which could then be applied to actual imaging studies. Also, since spherical spreading is incorporated by the algorithm, these resulting trends are only valid for applications where this assumption is good, such as for measurements taken in the far-field.

The propagated waveforms are shown first, followed by the statistical and bispectral analysis. The table of simplified waveform names is repeated here for easy reference.

Table 4.1 List of Input Waveforms

Spectral Shape	Center Frequency [Hz]	Simplified Name
f^2	100	waveform 1
f^2	500	waveform 2
f^4	100	waveform 3
f^4	500	waveform 4

4.1.1 Shock Formation and Coalescence

At high amplitudes, it is expected that nonlinear effects will occur during propagation. Figure 4.2 shows a portion of waveform 1 at several distances as it propagated out

[1]Because of the small useable bandwidth and short propagation distances, losses did not play a significant role in propagation. In real life applications, large bandwidths and longer propagation distances will cause losses and other atmospheric effects to play a more important role in propagation.

to 2 meters, where the initial OASPL of the waveform at the source was 166 dB. A

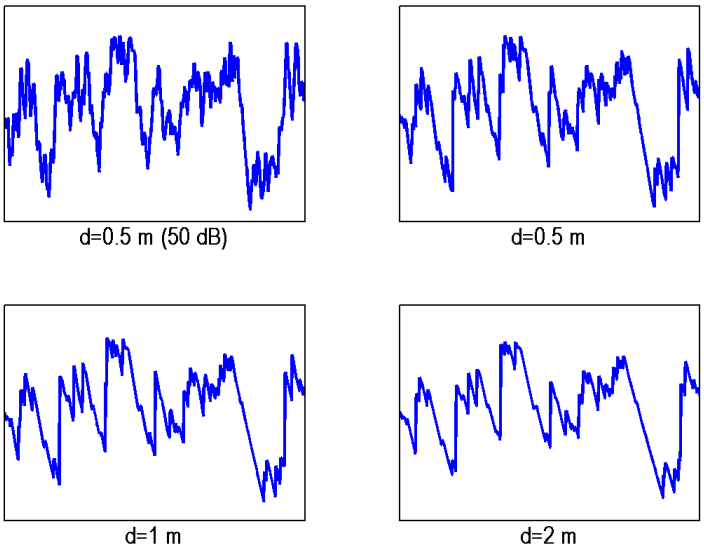

Figure 4.1 Snapshots of waveform 1 at 166 dB as it propagates nonlinearly, with the top right figure as a low-amplitude reference (no nonlinear effects). Waveform steepening is clearly evident with some shock formation.

reference low-amplitude segment is also included. It is clear that waveform steepening has occurred as the waveform propagated causing several shocks to form. Some smaller undulations have also been overtaken by the shock fronts.

Figure 4.2 depicts portions of waveform 2 at the same distances and initial amplitude. It appears that some shocks have already begun to form at 0.15 meters from the source. By 1 meter, the shocks dominate the waveform and most of the smaller undulations are gone. There also appears to be some shock coalescence by 2 meters.

Propagation of waveform 3 under the same conditions is shown in Figure 4.3. Again, there appears to be some waveform steepening and shock formation. However, since waveform 3 is the closest to a sinusoid, there exist fewer undulations. Therefore, waveform steepening and shock formation have not extremely altered the waveform.

Finally, waveform 4 is shown in Figure 4.4. As with waveform 2, significant

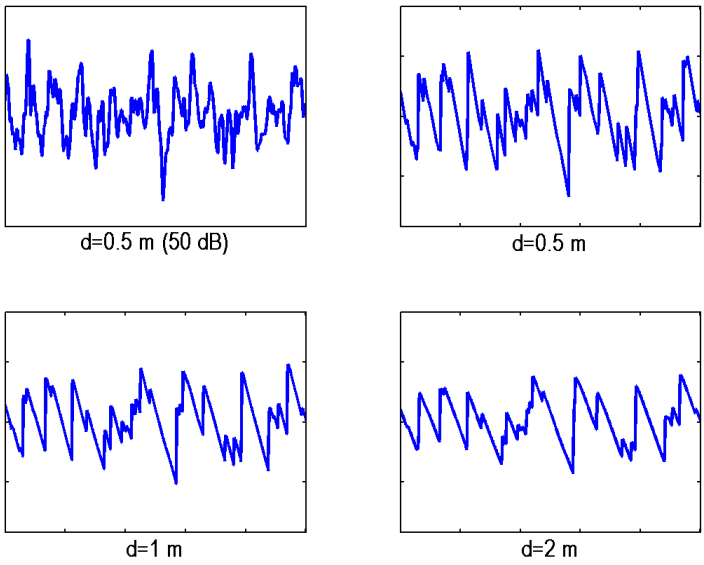

Figure 4.2 Snapshots of waveform 2 at 166 dB as it propagates nonlinearly, with the top right figure as a low-amplitude reference (no nonlinear effects). Shocks have formed very quickly and seem to dominate the waveform.

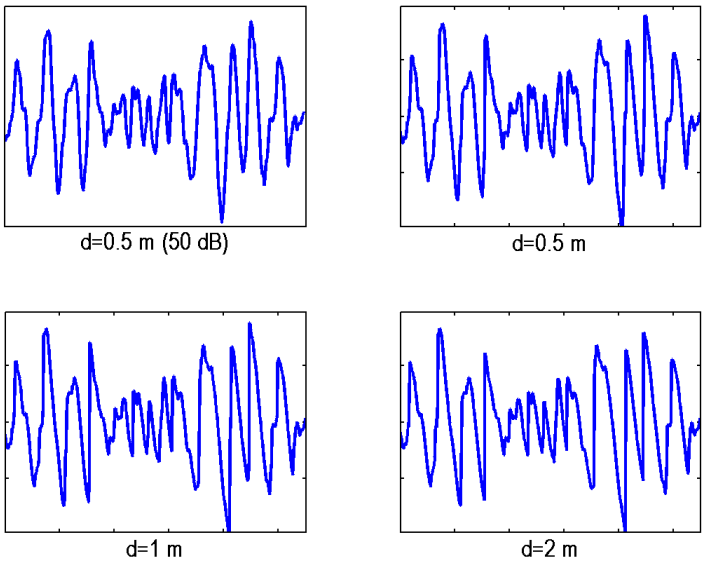

Figure 4.3 Snapshots of waveform 3 at 166 dB as it propagates nonlinearly, with the top right figure as a low-amplitude reference (no nonlinear effects). Some shock formation is evident.

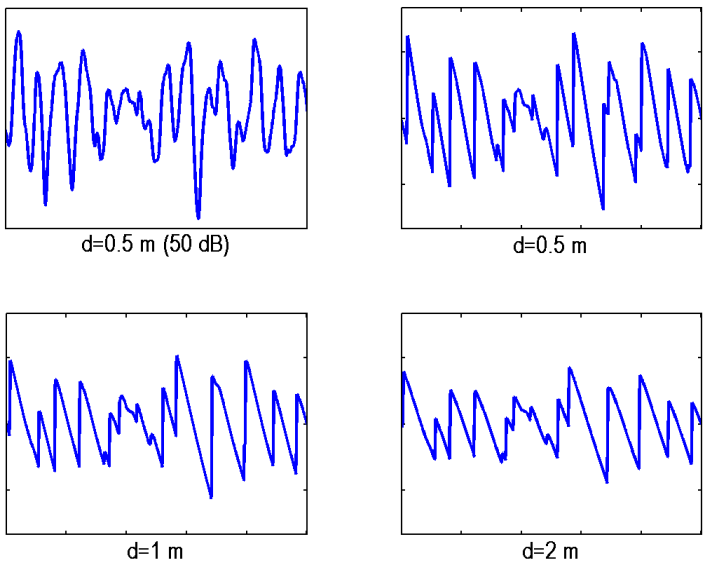

Figure 4.4 Snapshots of waveform 4 at 166 dB as it propagates nonlinearly, with the top right figure as a low-amplitude reference (no nonlinear effects). Shocks have formed very quickly and seem to dominate the waveform.

waveform steepening and shock formation have occurred after propagating only 0.15 meters. After 2 meters, there also appears to have been coalescence of shocks.

4.1.2 Statistical Analysis

The skewness and kurtosis coefficients were then calculated for both the time waveform and time derivative of the waveforms to help determine whether the PDF had changed after the nonlinear propagation. Distances are referenced from the origin, which was set 0.32 meters behind the source. Figure 4.5 plots the higher-order moments of waveform 1 against distance for the four amplitudes. The skewness coefficient remains close to zero for all amplitudes and distances, while the kurtosis values remain close to 2.75 for all amplitudes except 166 dB, which deviates slightly starting at 0.8 meters. Even though the kurtosis is not exactly three for the low-amplitude case, the constant behavior over distance indicates that the distribution is close to

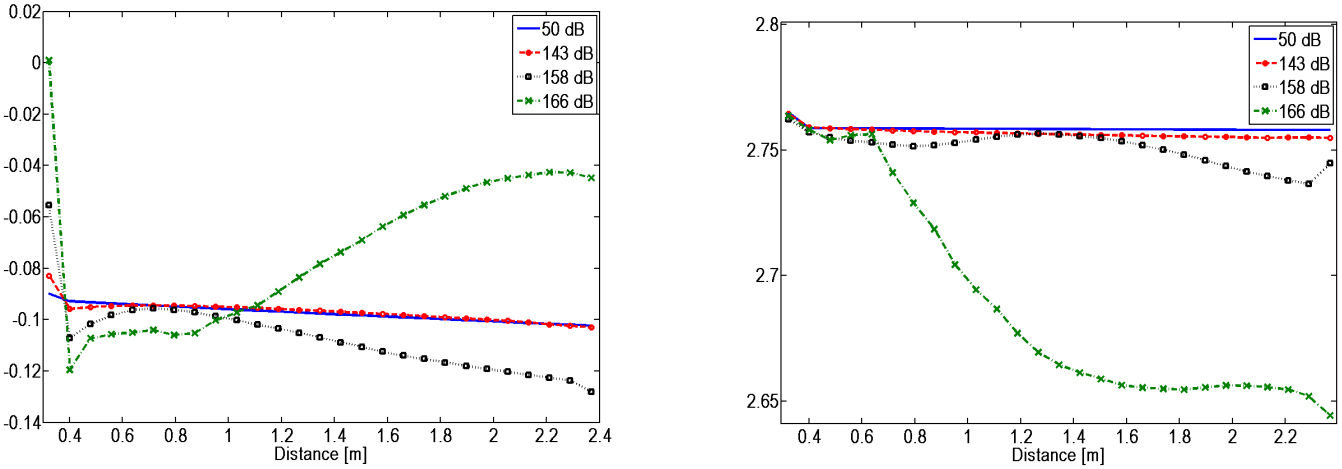

(a) (b)

Figure 4.5 The (a) skewness and (b) kurtosis values for waveform 1 plotted against distance at four amplitudes. The kurtosis at 166 dB begins to deviate slightly from three after 0.8 meters.

Gaussian and, more importantly, does not change with distance. The PDFs shown in Figure 4.6 are for the 50 dB case and the 166 dB case at 2 meters. The high amplitude case has a similar distribution as the low amplitude case.

Next, Figure 4.7 shows the same statistical quantities, but applied to the time derivative of the data. The low amplitude case reveals near-perfect Gaussian behavior for all distances, while the higher amplitude cases deviate from Gaussian behavior rather quickly. Of particular note is the increasing values of both quantities with distance and amplitude. The initially 158 and 166 dB waveforms show very non-Gaussian behavior after very small propagation distances. Figure 4.8 shows the PDF for the 50 and 166 dB runs at 2 meters. The PDF has transformed from being very Gaussian to being extremely skewed with a concentration of values slightly below zero and a small tail of outliers. This gives strong evidence of nonlinear effects that are not as apparent in the analysis of the time waveform alone. All four waveforms

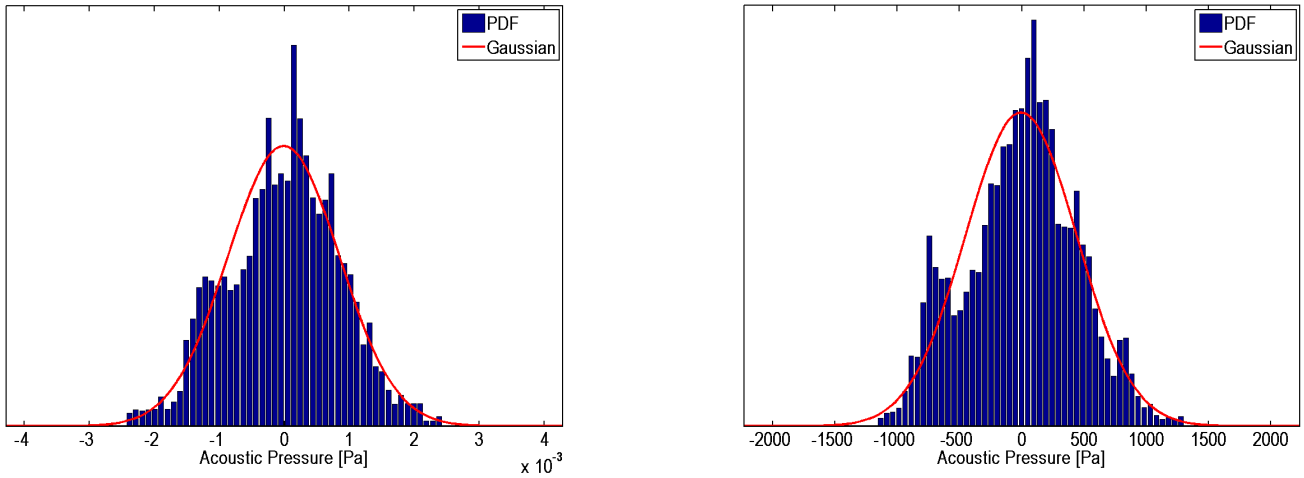

(a) (b)

Figure 4.6 The PDFs for waveform 1 for (a) the 50 dB case and (b) the 166 dB case both after propagating 2 meters. The shape is still generally the same.

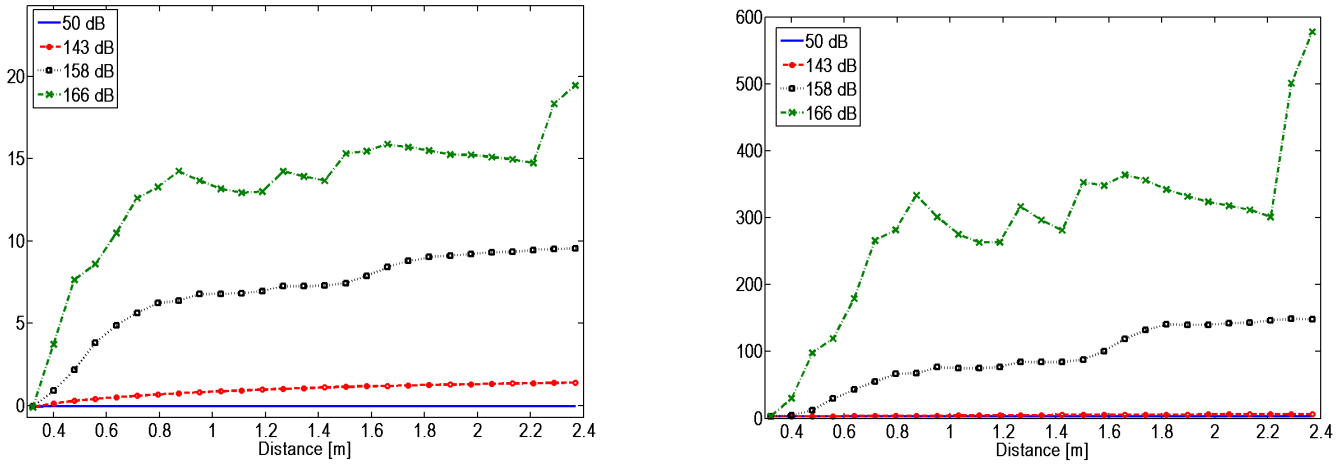

(a) (b)

Figure 4.7 The (a) skewness and (b) kurtosis values for the time derivative of waveform 1 plotted against distance at four amplitudes. The initially 158 and 166 dB waveforms show very non-Gaussian behavior after very small propagation distances. The value at the shocks cannot be seen on this scale, but are located between about 50 and 300 Pascals per second.

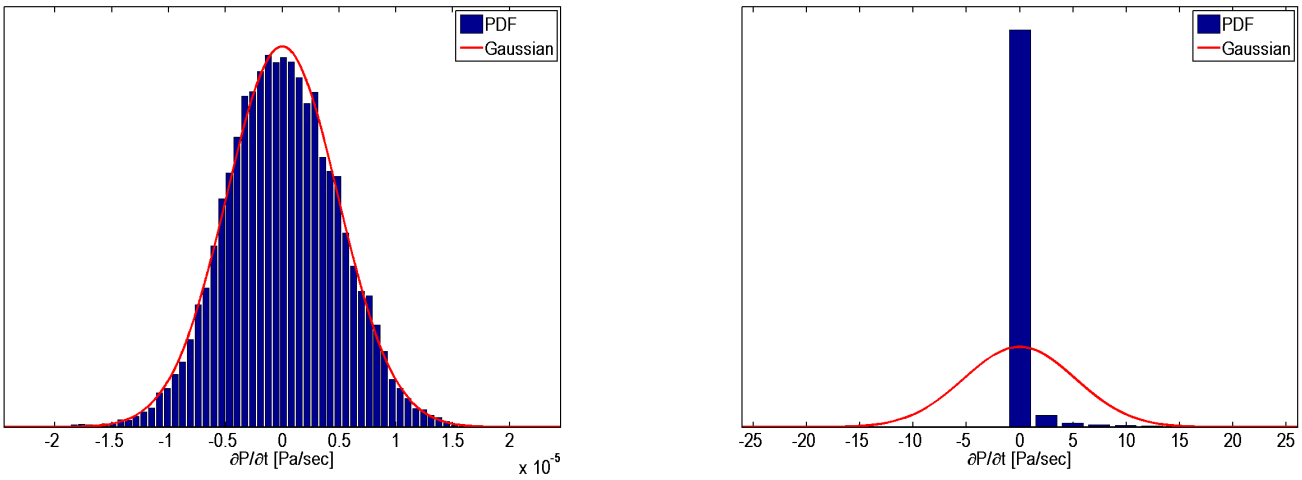

(a) (b)

Figure 4.8 The PDFs for the time derivative of waveform 1 for (a) the 50 dB case and (b) the 166 dB case both after propagating 2 meters. The shape has shifted from Gaussian to extremely skewed.

exhibit this same trend with the PDF shifting from Gaussian or nearly Gaussian to extremely skewed, with basically no new information. For this reason, the remaining time derivative PDFs are not shown and only the skewness and kurtosis values are discussed.

For waveform 2, many of the same trends are apparent in the statistics of the time data (see Figure 4.9), except that the kurtosis now slightly deviates for both the initially 158 and 166 dB cases after only 0.5 meters. The PDFs (shown in Figure 4.10) also change, becoming more uniform after high amplitude propagation, an indication of shock formation.

Analysis of the time derivative again yields more information. The trend of increasing skewness and kurtosis values with amplitude is again shown, but only for short propagation distances (see Figure 4.11). The initially 158 and 166 dB cases reach a maximum in both skewness and kurtosis, then seem to slowly decrease. The

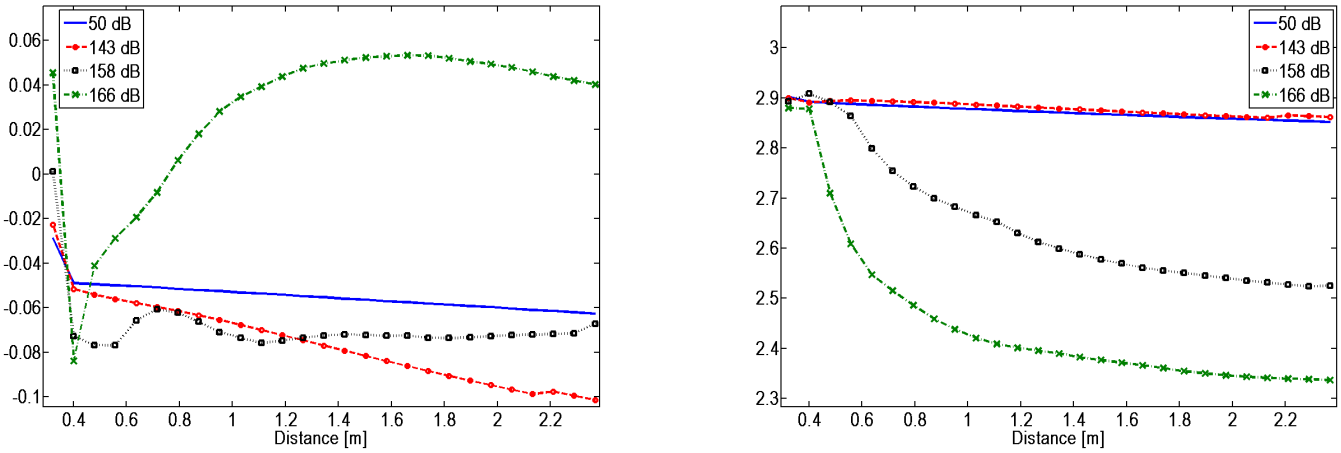

(a) (b)

Figure 4.9 The skewness a) and kurtosis b) value for waveform 2 plotted against distance at four amplitudes.

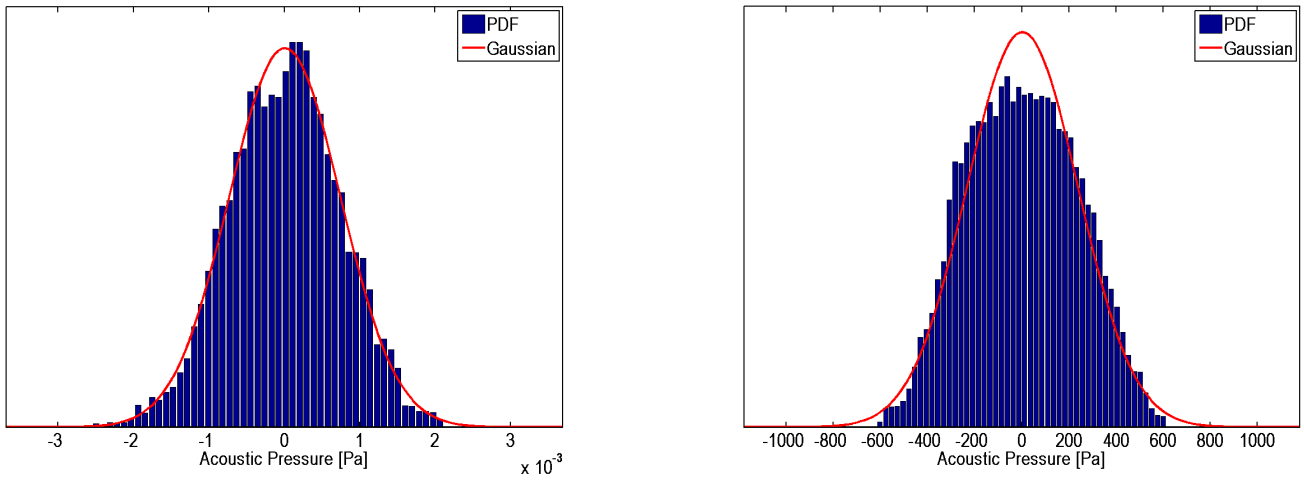

(a) (b)

Figure 4.10 The PDFs for waveform 2 for (a) the 50 dB case and (b) the 166 dB case both after propagating 2 meters. The distribution has become more uniform for the 166 dB case.

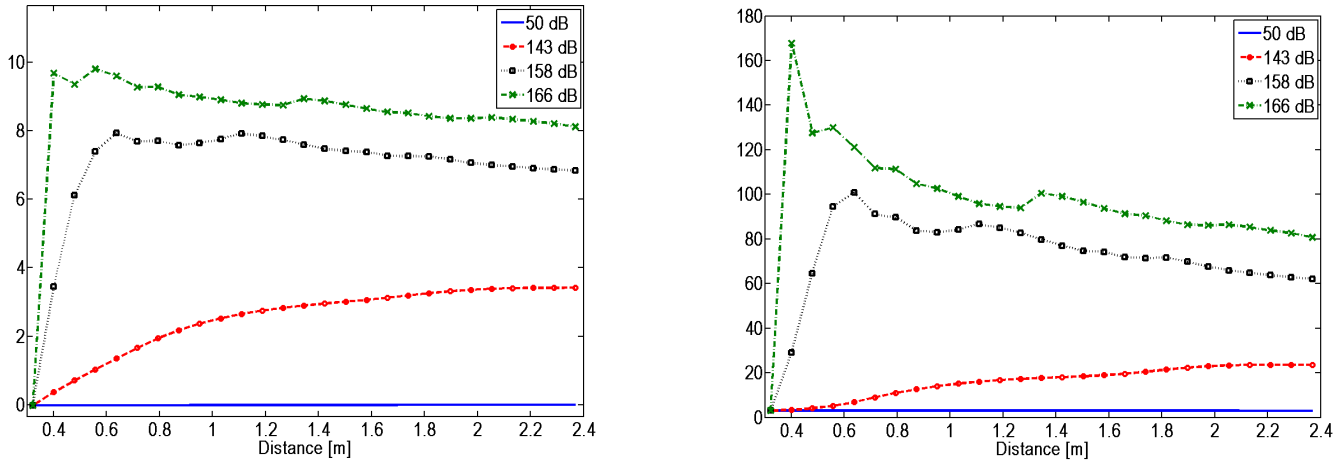

(a) (b)

Figure 4.11 The (a) skewness (b) kurtosis values for the time derivative of waveform 2 plotted against distance at four amplitudes. Both the skewness and kurtosis increase out to some distance, then decrease for the 158 and 166 dB cases.

maximum is reached at 0.7 meters for the lower of the two amplitudes and at 0.4 meters for the higher amplitude.

The skewness and kurtosis values for waveform 3 are shown in Figure 4.12 with the PDFs shown in Figure 4.13. The trends are very similar to waveform 1, except that the kurtosis for the 166 dB case deviates slightly differently. Even with this irregular deviation, the kurtosis values still remain quite close to other values. The PDFs again have the same general shape for the low-amplitude and high-amplitude cases.

Analysis of the time derivative reveals slightly different behavior than that of waveform 1 as is shown in Figure 4.14. The 143 and 158 dB cases increase as expected, but the 166 dB case increases until 0.8 meters, then decreases similar to waveform 2.

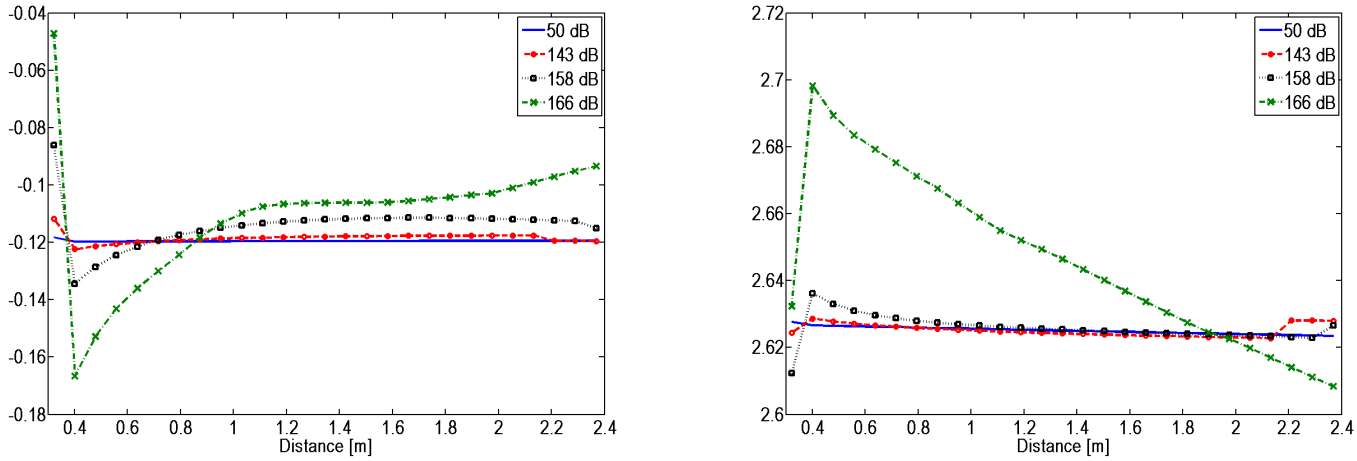

(a) (b)

Figure 4.12 The (a) skewness and (b) kurtosis values for waveform 3 plotted against distance at four amplitudes. The skewness and kurtosis do not change significantly for low amplitudes and only change slightly for high amplitudes.

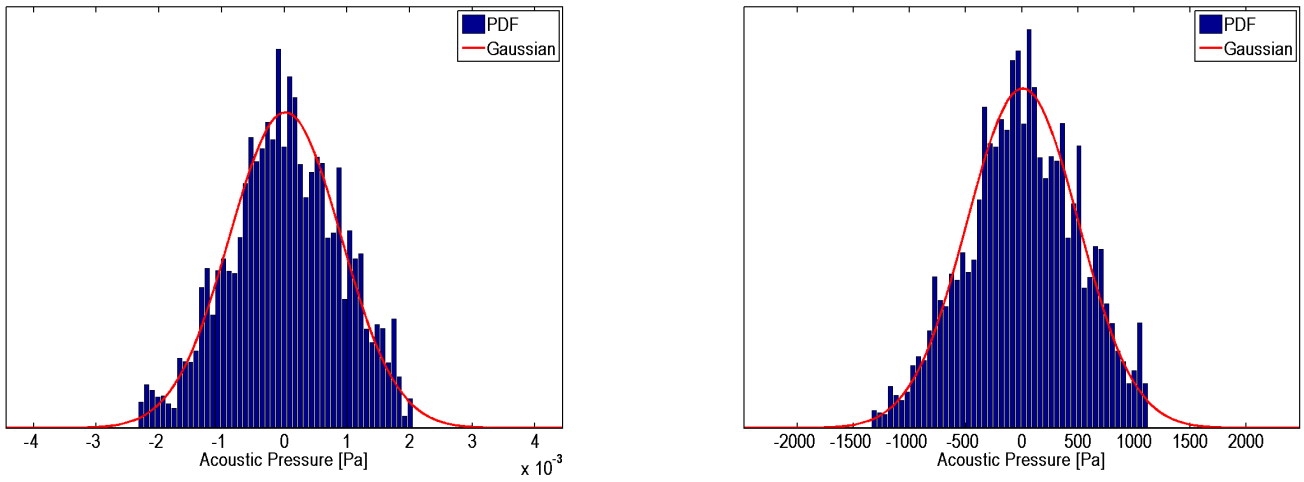

(a) (b)

Figure 4.13 The PDFs for waveform 3 for (a) the 50 dB case and (b) the 166 dB case both after propagating 2 meters. The shape is still generally the same.

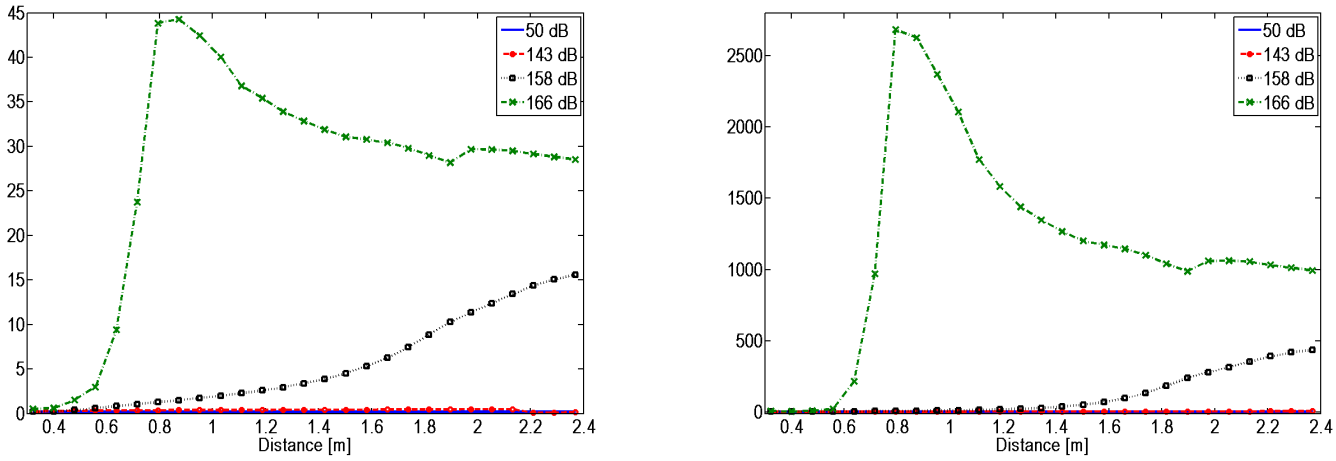

(a) (b)

Figure 4.14 The (a) skewness and (b) kurtosis values for the time derivative of waveform 3 plotted against distance at four amplitudes. The skewness and kurtosis exhibit the same rise and fall behavior for the 166 dB case as with waveform 2.

Finally, for waveform 4 many of the same trends are exhibited that were observed for waveform 2. The PDF becomes more uniform and the same rise and fall is exhibited in the skewness and kurtosis values at 158 and 166 dB. However, the switch from increasing quantities to decreasing quantities happens at a shorter distance. This again indicates nonlinear activity, but seems to occur at lower amplitudes and distances.

The fact that the skewness and kurtosis for the derivative show a trend of increasing as nonlinear effects kick in for all the cases, but then decrease at higher amplitudes and larger distances for waveforms 2-4 suggests that there is physical meaning in this decrease. The losses at the shock fronts would cause the slope of the waveform between the shocks to decrease. The distribution would then change as the outliers shift toward then mean. Since the increase in higher-order moments of the derivative is due to waveform steepening and shock formation, once the waveform becomes mostly

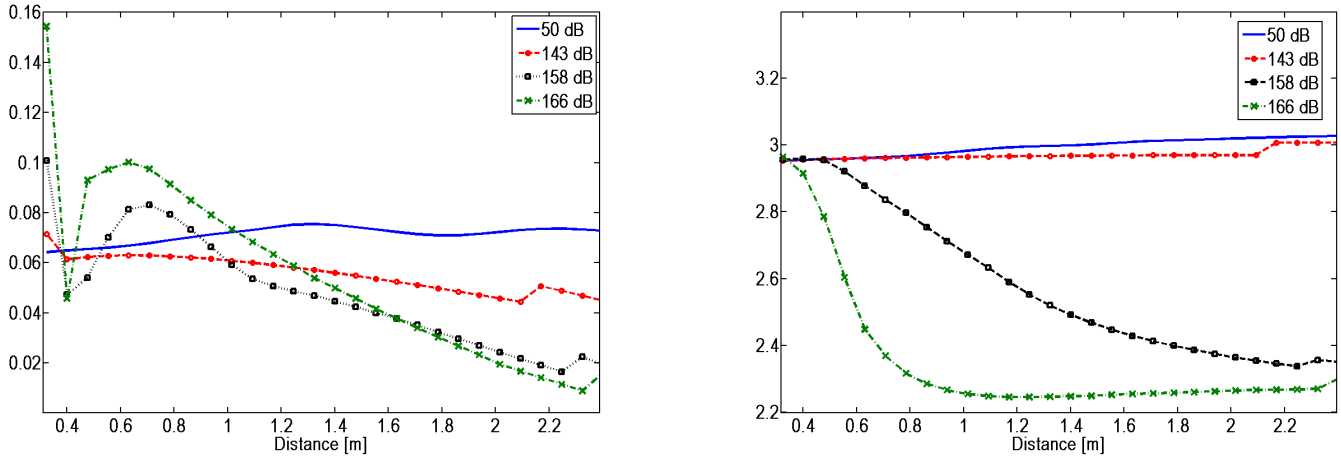

(a) (b)

Figure 4.15 The (a) skewness and (b) kurtosis values for waveform 4 plotted against distance at four amplitudes.

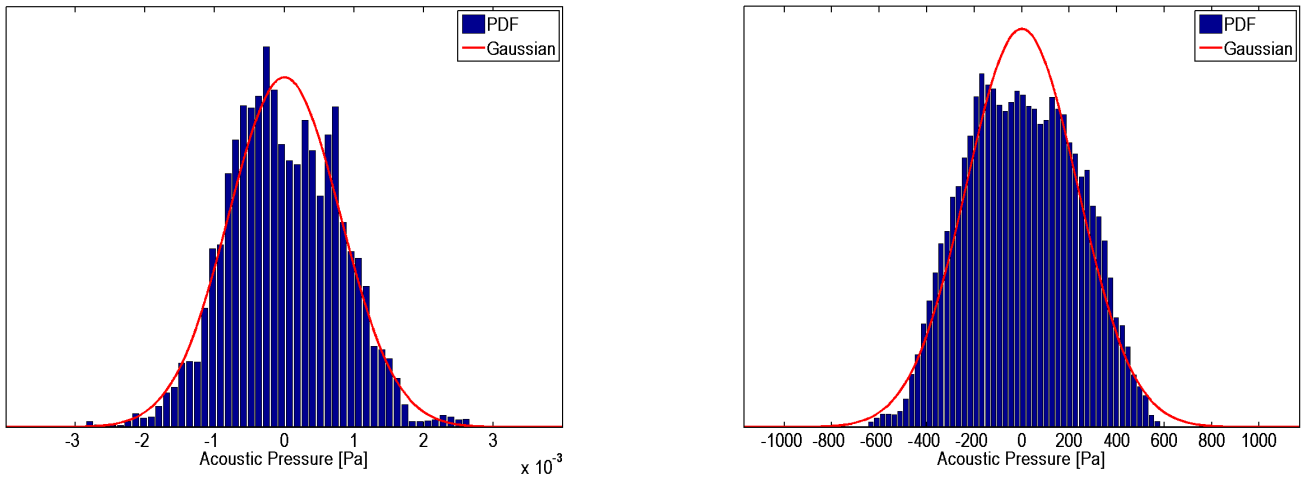

(a) (b)

Figure 4.16 The PDFs for waveform 4 for (a) the 50 dB case and (b) the 166 dB case both after propagating 2 meters. The shape is becoming more uniform.

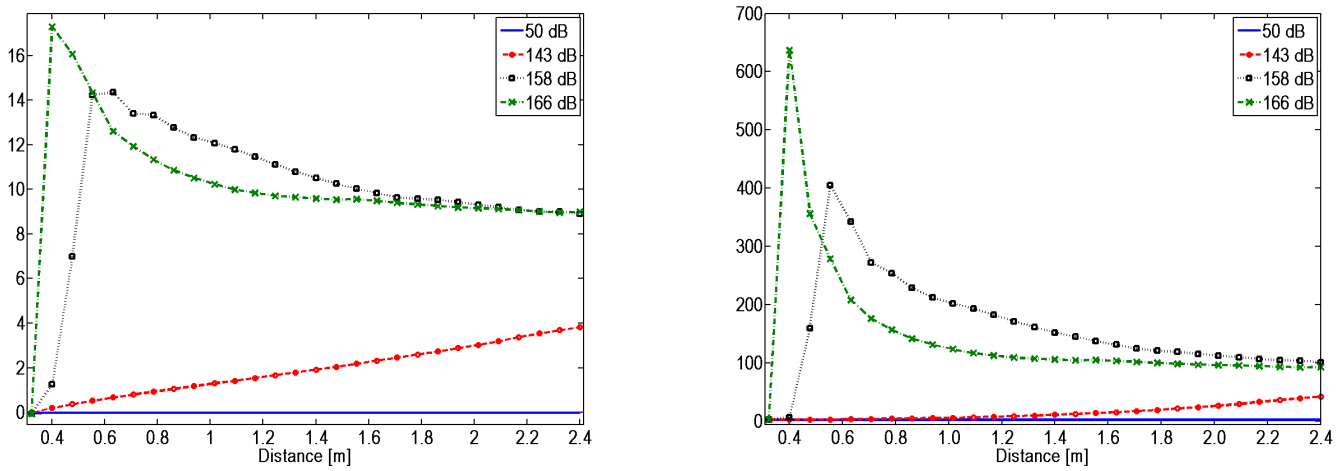

(a) (b)

Figure 4.17 The (a) skewness and (b) kurtosis values for the time derivative of waveform 4 plotted against distance at four amplitudes. The skewness and kurtosis rise and fall again for the 158 and 166 dB case but at shorter distances.

dominated by shocks and waveform steepening occurs less significantly, the changes due to losses at the shocks will have a more dominant effect the PDF. Thus, a decrease in skewness and kurtosis coefficients would indicate that the waveform is dominated by shocks and that the effect of waveform steepening is less significant than the effect of the decreasing of the shock amplitudes.

4.1.3 Bispectral Analysis

The bicoherence was computed next to show the relative amount of quadratic phase coupling between the four waveforms. The bicoherence is plotted with frequency on both axes with the color representing the value of the bicoherence at that bifrequency set. The scale shows that blue represents very little energy created due to nonlinear interactions at that bifrequency set with yellow, orange or red representing increasing

amounts of energy being created from interaction of those two frequencies. The results shown are in sets of increasing amplitude and distance. Since nonlinear effects increase with both, the same basic trends are seen for increasing just distance or amplitude, though possibly less pronounced.

Figure 4.18 shows the four waveforms for the initially 143 dB case after propagating 0.15 meters. Waveform 3 is the darkest blue showing very little quadratic phase

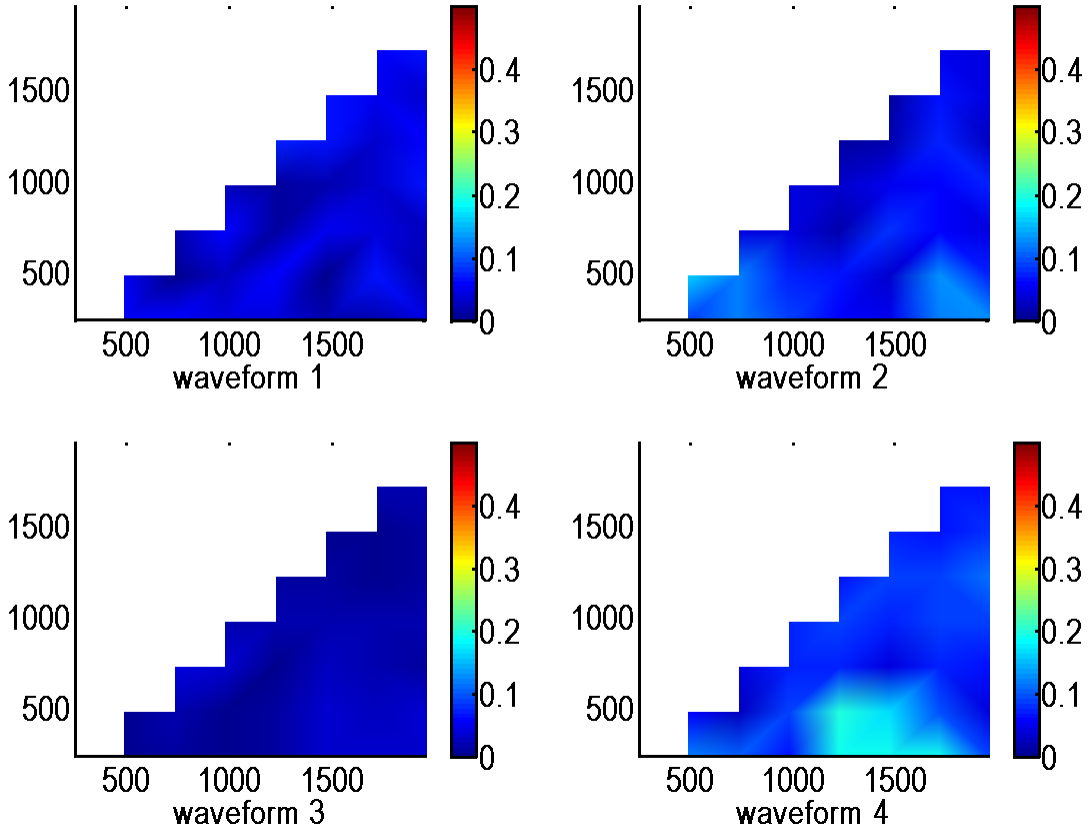

Figure 4.18 Bicoherence for the four waveforms initially at 143 dB after propagating 0.15 meters. Waveform 4 is beginning to show some nonlinear interactions.

coupling, while waveforms 1 and 2 show slightly lighter shades of blue. Both however have bicoherence values close to zero. Waveform 4 shows the most interactions with

non-zero bicoherence occurring between frequencies below 500 Hz and between 1000 Hz and 1500 Hz.

The next plot shows the same waveforms initially at 158 dB and propagating 1 meter. Now, all the waveforms show some nonlinear activity. Again, waveform 3

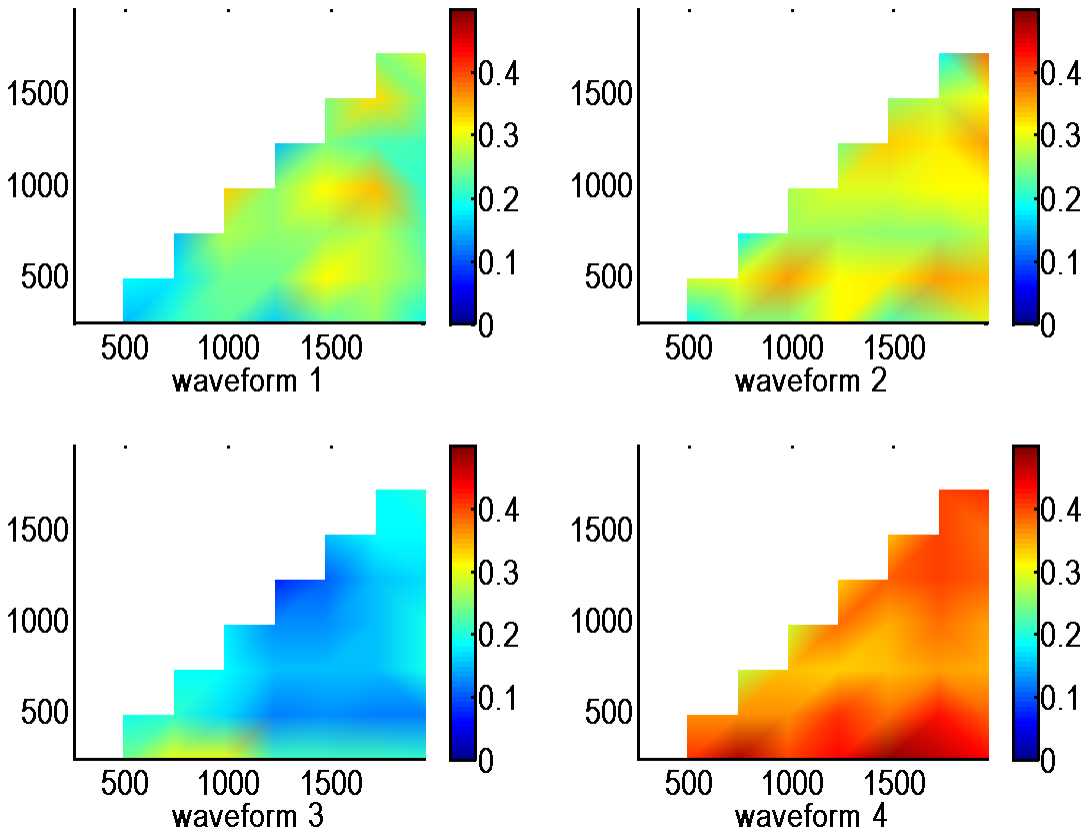

Figure 4.19 Bicoherence for the four waveforms initially at 158 dB after propagating 1 meter. All the waveforms show some nonlinear interactions, with waveform 4 exhibiting the highest amount and waveform 3 exhibiting the lowest amount.

seems to show the least amount of phase coupling, followed by waveforms 1, 2 and 4. Bicoherence values for waveform 4 ranges from 0.2 to 0.4 at all bifrequencies suggesting that all frequencies are interacting with each other.

Finally, Figure 4.20 shows the waveforms after propagating 2 meters and having

an initial level of 166 dB. All the waveforms have significant interaction between all

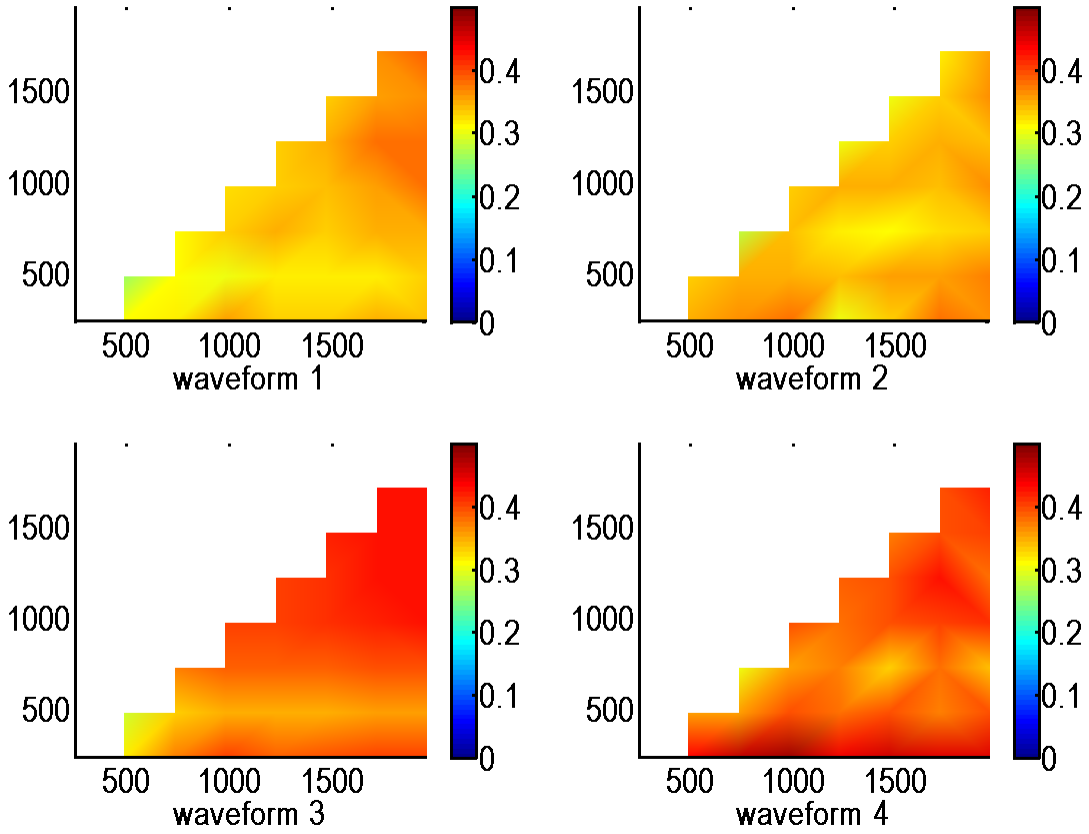

Figure 4.20 Bicoherence for the four waveforms initially at 166 dB after propagating 2 meters, with the bicoherence values higher than for the 1 meter propagation. Now waveform 3 seems to have the highest amount of nonlinear interaction.

the frequencies shown. However, waveform 3 now seems to have the highest amount of phase coupling.

These results show that waveform 3 experienced the least amount of nonlinear effects for lower amplitudes and propagation distances, but seemed to experience the largest amount of nonlinear phase coupling at higher amplitude and propagation distances. Waveform 4 experienced more nonlinear effects at lower amplitudes and distances and waveforms 1 and 2 experienced about the same amount of phase

coupling at all distances and amplitudes. Since waveforms 3 and 4 show the most phase coupling at 166 dB and also have the same spectral shape, it appears that the narrow-band spectral shape experiences more nonlinear effects at higher amplitudes.

4.1.4 Comparison of Statistical and Bispectral Analyses

The statistical analysis results cannot readily be compared to the bispectral analysis results because they are viewed in different domains, in the time and frequency domains respectively. However, they both do show that waveform 4 having the most amount of nonlinearity over the shortest distances. This is apparent in Figures 4.18, 4.19 and 4.20 from bispectral analysis and in Figures 4.17 from statistical analysis.

4.2 Two-dimensional Propagation

The study moves next to two-dimensional propagation. Since jet and rocket sources are known to be extended and Laufer, *et al.* [19] found that the use of independent sources is a realistic description of acoustic behavior supersonic jet flow, a simple model would be an array of point sources. Two point sources were used in this research as the most basic model. The domain was set to have dimensions of 0.11 x 0.13 meters with a discretization step of .0001715 meters. In order to study the nonlinear effects in such a small domain, waveform 4 was used as the input to the first point source because it induces more nonlinearity than the other waveforms over shorter distances. An additional random-noise waveform with the same characteristics as waveform 4 was created and input into the second point source so that each source was independent from the other.

4.2.1 High Amplitude Comparison

Both a low-amplitude case, shown in Figure 4.21, and a high amplitude case, shown in Figure 4.22, were performed so that the differences in the interference patterns due to nonlinear propagation could be observed. The figures show the acoustic pressure at a single snapshot in time, with the pressure value indicated at each spatial point by the color of the plot. The nonlinear case shows sharp transitions between extrema

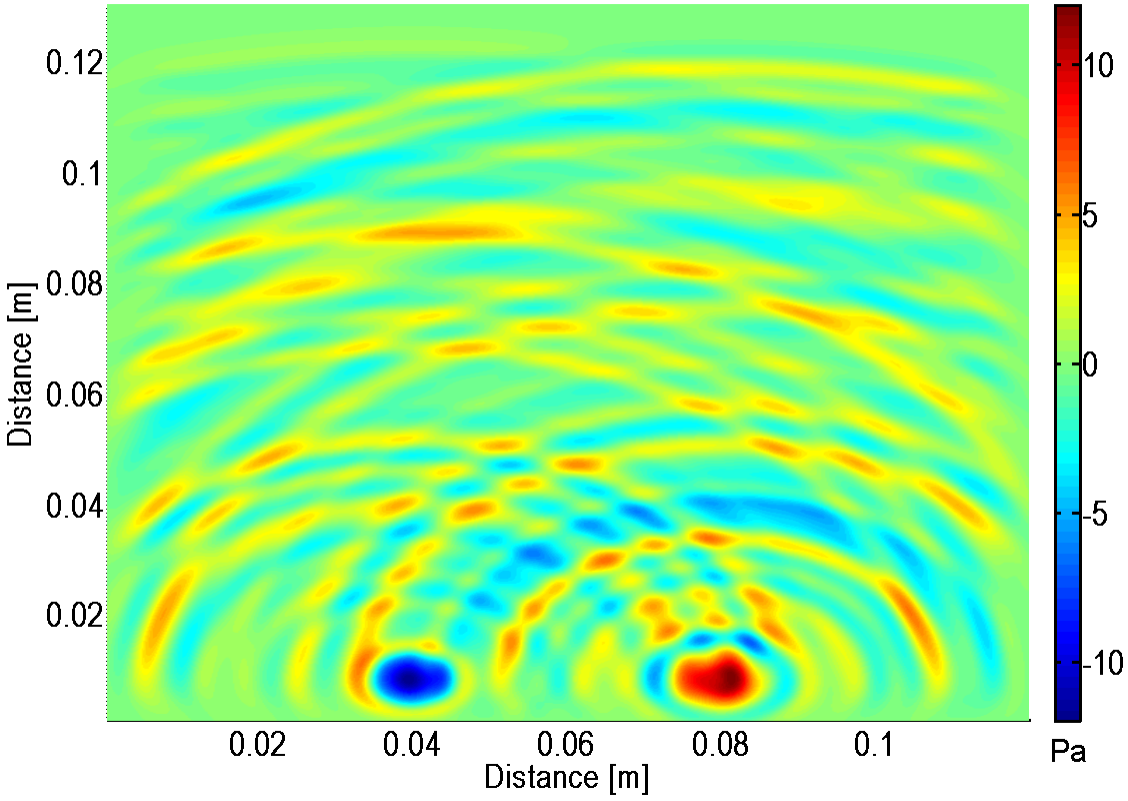

Figure 4.21 A surface plot of the broadband radiation from two point sources at a low amplitude (100 dB), where the color represents the acoustic pressure. This shows the linear interference patterns that develop due to superposition.

suggesting the formation of shocks. The spatial derivative shows more clearly the locations of the shock fronts. Figure 4.23 shows the spatial derivative in x while

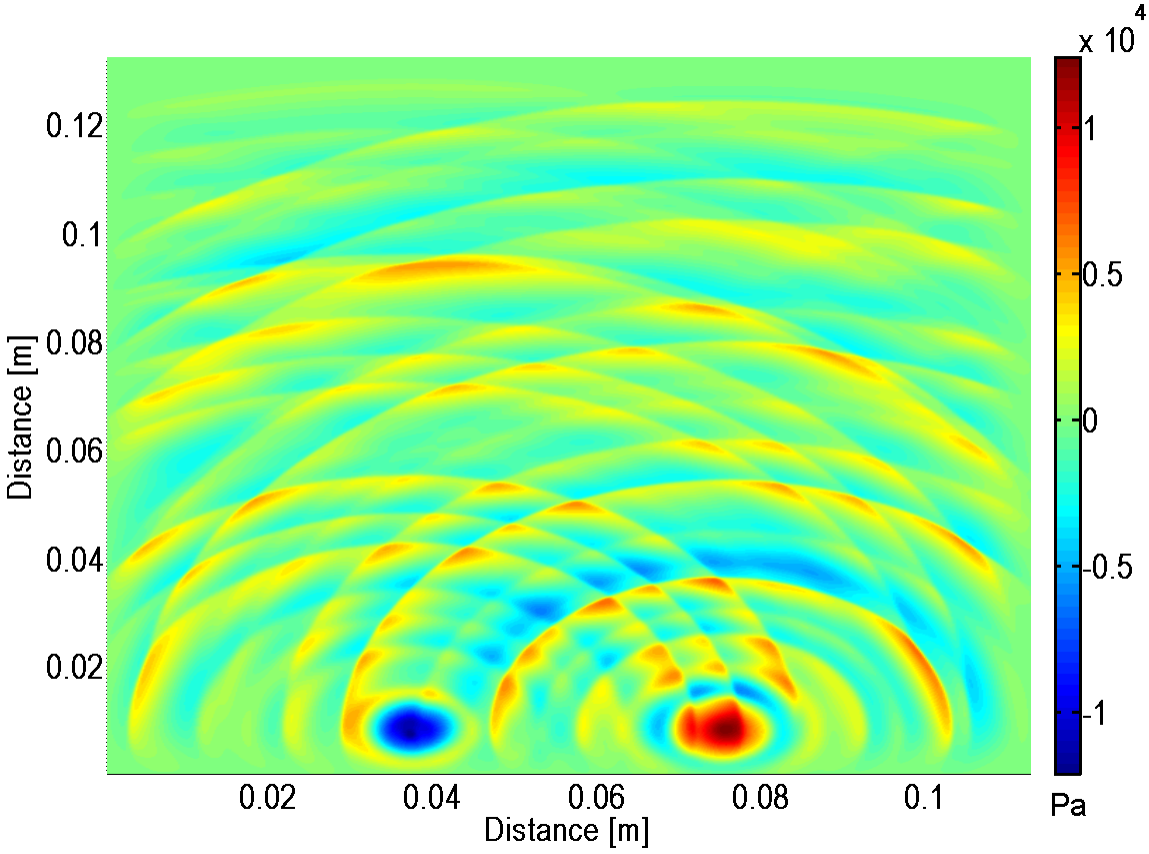

Figure 4.22 A surface plot of the broadband radiation from two point sources at a high amplitude (170 dB), where the color represents the acoustic pressure. This shows the interference patterns that develop when propagation is nonlinear. The area of sharp transitions indicate shock fronts.

Figure 4.24 shows the spatial derivative in y.

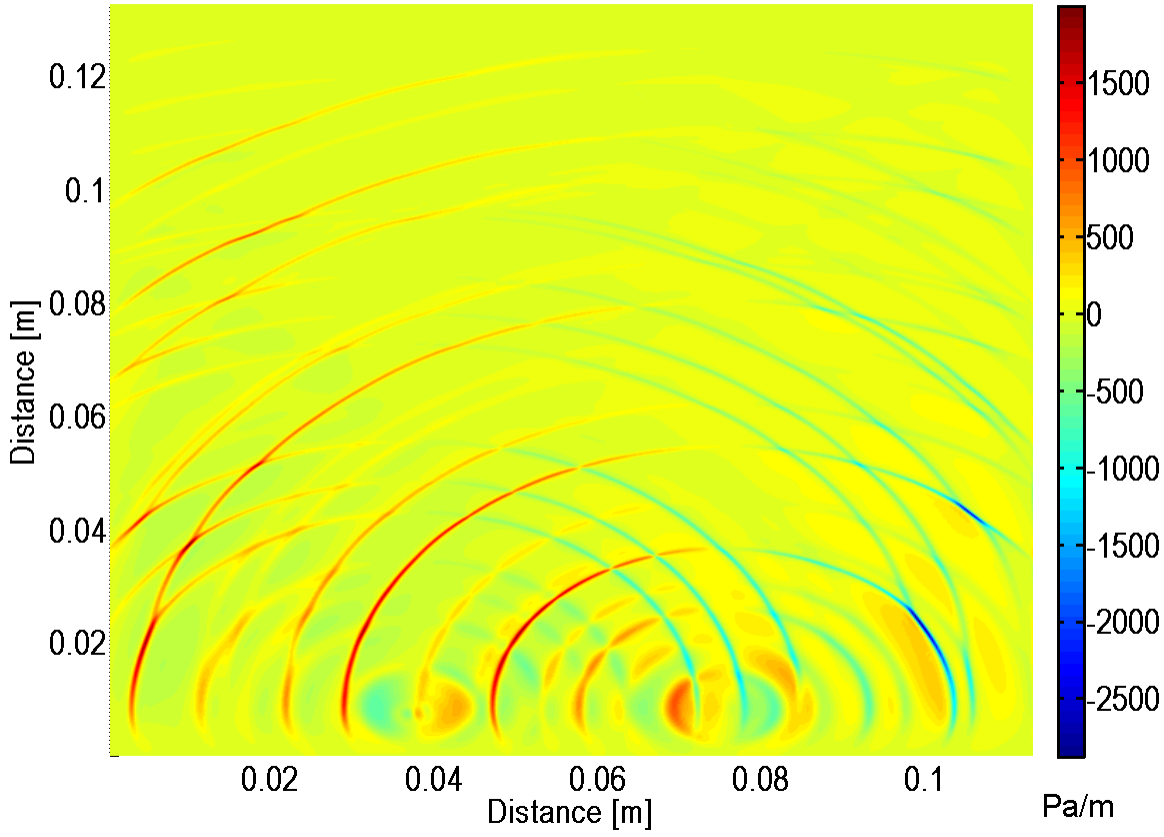

Figure 4.23 The spatial derivative in x for the high-amplitude case in 2-D clearly defines the locations of the shocks in the x-direction.

To investigate more fully the differences between the high-amplitude and low-amplitude cases, several slices of the domain are shown at increasing distances from the sources with normalized amplitudes to be able to compare the shapes and are shown in Figures 4.25 and 4.26.

Figure 4.25 shows the first slice, set through both sources. The nonlinear case (red) deviates most from the linear case (blue) at the edges where definite steepening has occurred. It must be noted that since the waves are spherical, the steepening will be in the direction of propagation, causing the steepening on the edges to be in

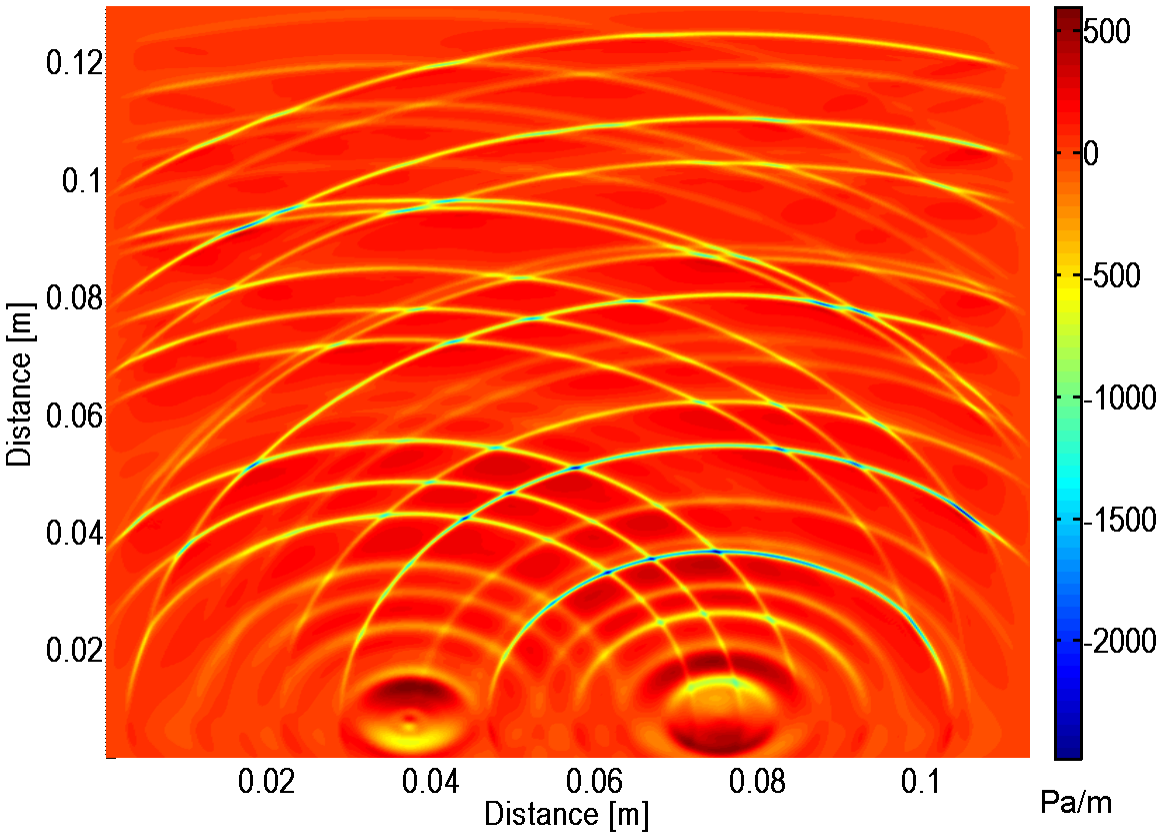

Figure 4.24 The spatial derivative in y for the high-amplitude case in 2-D clearly defines the locations of the shocks in the y-direction.

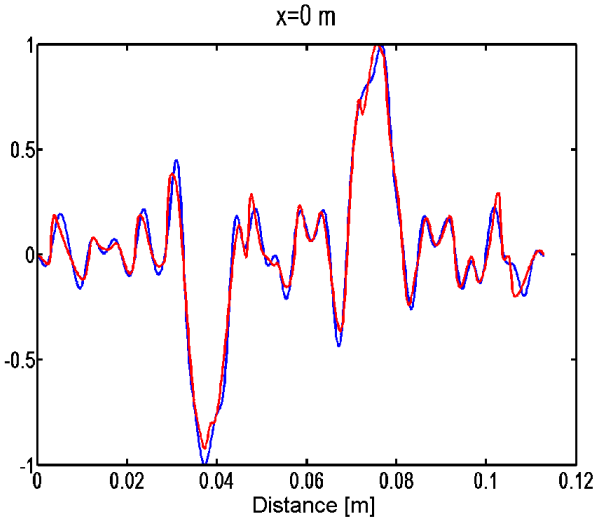

Figure 4.25 A slice of the domain at the sources for the linear (red) and nonlinear (blue) case with normalized pressure amplitudes. Deviations at the edges are due to waveform steepening.

opposite directions. The noted deviations at the edges are expected considering the theory of nonlinear propagation discussed in Chapter 2.

The next slice is set 0.025 meters from and parallel to the sources and is shown in Figure 4.26. There again appears to be waveform steepening near the edges of the slice. However, in the center region the deviations seem to be much more complicated and unpredictable. This is caused by the random interaction of the two broadband waveforms. Since the portions of highest amplitude will steepen up fastest, and the two waveforms are independent, the interactions of the two possibly steepened waveforms will be totally unpredictable.

The last slice is set at 0.043 meters from the sources in Figure 4.27. Again, the deviation for linear behavior in the center region is totally unpredictable. Since propagation in two dimensions now includes interference effects, the differences between linear and nonlinear will not just be from waveform steepening and shock coales-

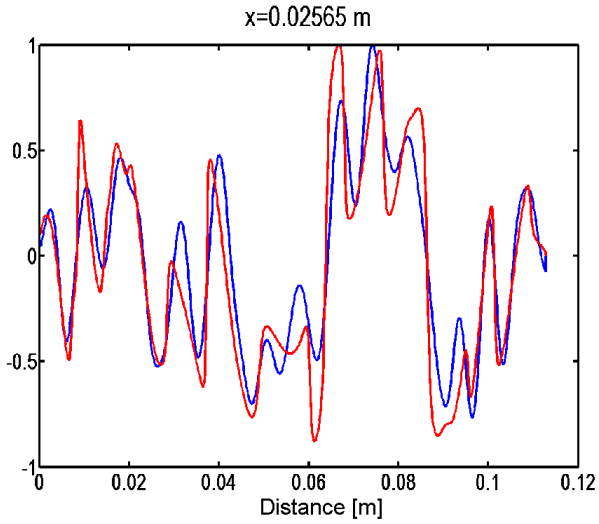

Figure 4.26 A slice of the domain taken 0.025 meters from the source for the linear (red) and nonlinear (blue) case with normalized pressure amplitudes. Complicated interactions are beginning to cause unpredictable deviations between linear and nonlinear.

cence. The differences are also due to extremely complicated interference pattern from combinations of completely unsteepened portions, partially steepened portions and completely shocked portions. If a continuous source distribution were used instead of discrete sources, diffraction effects would also occur.

4.3 Chapter Summary

In summary, the propagation results in one dimension reveal that all the waveforms experienced significant nonlinear effects at 166 dB after propagating 2 meters, causing the waveform to deviate significantly from that expected with linear propagation. The nonlinear effects were smaller with lower amplitudes and smaller propagation distances. However, the waveform steepening and shock formation occur fastest for

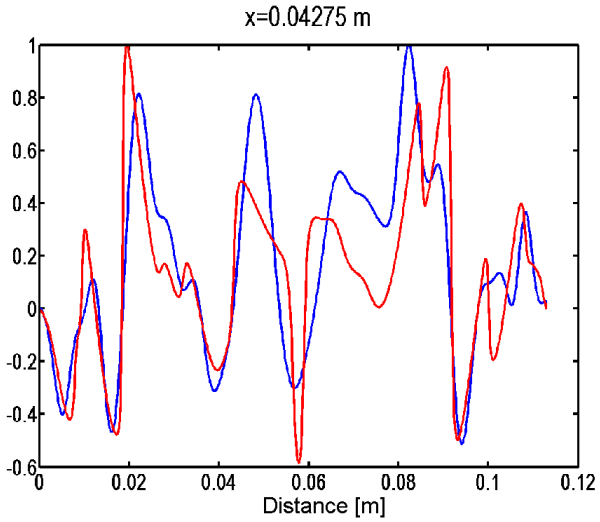

Figure 4.27 A slice of the domain 0.043 meters from the source for the linear (red) and nonlinear (blue) case with normalized pressure amplitudes. Complicated interactions cause unpredictable deviations between linear and nonlinear.

spectra with higher center frequencies and the narrowest spectral shape. This was shown using statistical analysis of the time derivative and bispectral analysis. Additionally, the skewness and kurtosis of the time derivative seem to decrease when shocks are dominant in the waveform. Finally, the two-dimensional propagation reveals that complicated interactions between steepened and unsteepened waveforms create complex interference patterns that cannot be predicted.

Chapter 5

Results: Reconstruction

After the waveforms were propagated nonlinearly in one dimension, the waveforms were reconstructed back to the source using spherical NAH and the errors were determined. The insight gained from the 1-D results is then applied to the two dimensional nonlinear propagation problem.

5.1 Reconstruction for One-dimensional Nonlinear Propagation

As mentioned in Chapter 4, virtual microphones recorded pressure data at equally spaced points in the domain. Of specific note are the virtual microphones placed at the source as well as at 0.15, 1 and 2 meters from the source. The microphone not located at the source are referred to as being located at holography planes[1], whereas the microphone at the source is referred to as being at the reference plane. Spherical NAH was then applied in the frequency domain to reconstruct the pressure

[1]These are actually points, but are referred as planes to keep the same convention as is typically used in NAH.

magnitude at the reference plane using the pressure at the holography planes. The reconstruction was then compared to the actual pressure spectrum recorded with the virtual microphone at the source so as to cancel out any initial numerical smoothing caused artificially by the algorithm. The error in decibels was determined in third-octave bands. The error magnitudes were then averaged to determine an average error value.

5.1.1 Reconstructed Power Spectra

The results presented for reconstruction are the initially 166 dB runs only. Since nonlinear effects increase with both distance and amplitude, the same trends should exist when varying just distance as when varying just amplitude. Therefore, the runs with initial amplitudes of 143 and 158 dB would presumably show the same effects after propagating longer distances as the 166 dB does propagating a shorter distance. Thus only the results from the 166 dB case are shown along with the errors at each frequency.

Figure 5.1 shows the reference and reconstructed PSDs from three distances in third-octave bands for waveform 1. This shows that the reconstructed spectra generally maintain the same shape. The small decreases in amplitude above the peak frequency for the higher amplitudes do, however, cause some error because the waveform itself is not preserved, only its shape. The error is shown as a function of distance and frequency in Figure 5.2. The errors are less than 2 dB at all frequencies and reconstruction distances.

The reconstructed forms of waveform 2 are shown in Figure 5.3 with good reconstruction at frequencies up to slightly below the center frequency. The reconstructed waveforms from 1 and 2 meters have significantly lower amplitudes and the center frequency appears to have shifted slightly downward. The error is shown as a func-

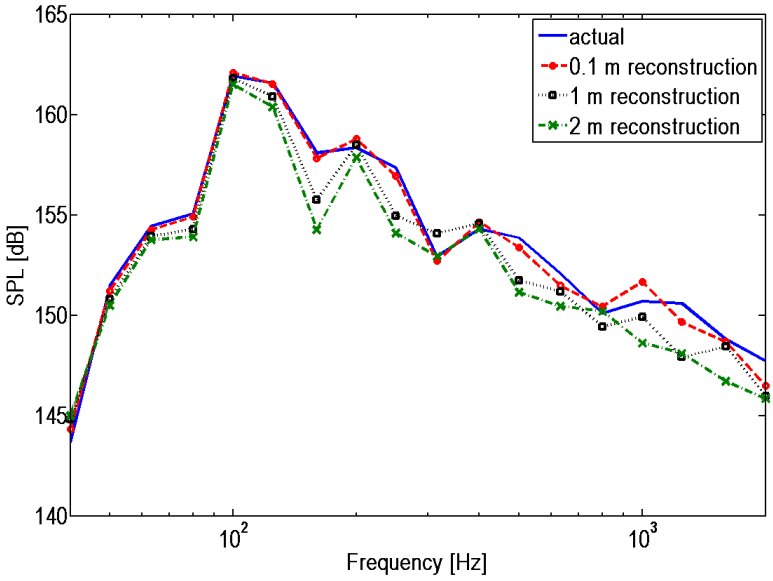

Figure 5.1 The reference and reconstructed power spectra for waveform 1 at 166 dB. The spectral shape is generally well maintained.

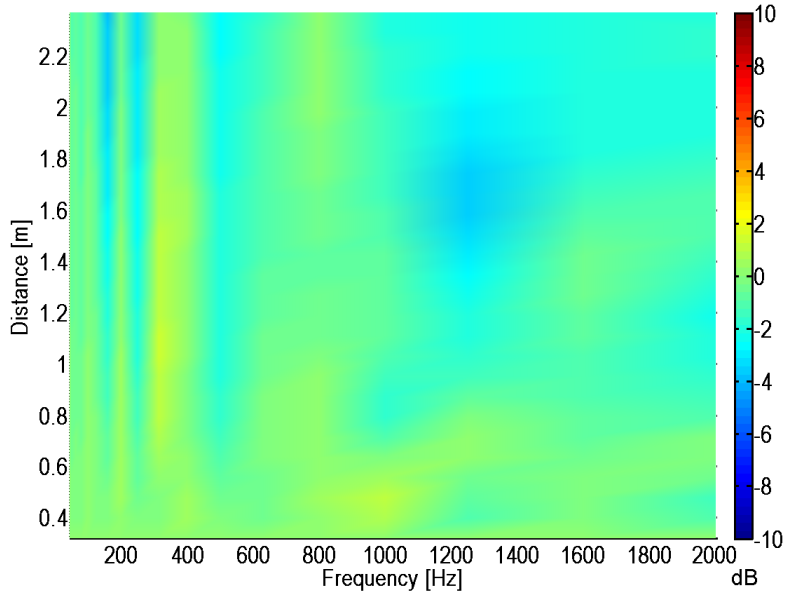

Figure 5.2 A surface plot of the error over frequency and distance for waveform 1 at 166 dB. The errors are relatively small for all distances and frequencies.

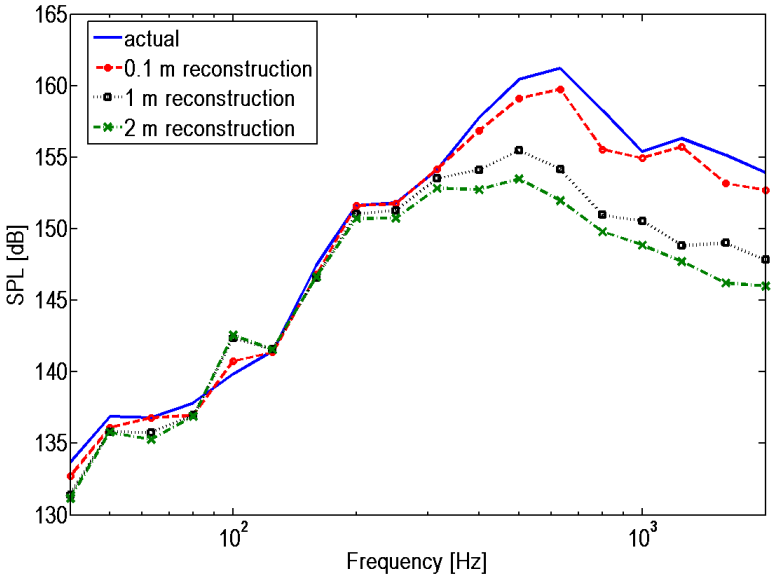

Figure 5.3 The reference and reconstructed power spectra for waveform 2 at 166 dB. The farther reconstruction distances greatly underestimate the middle and high frequencies.

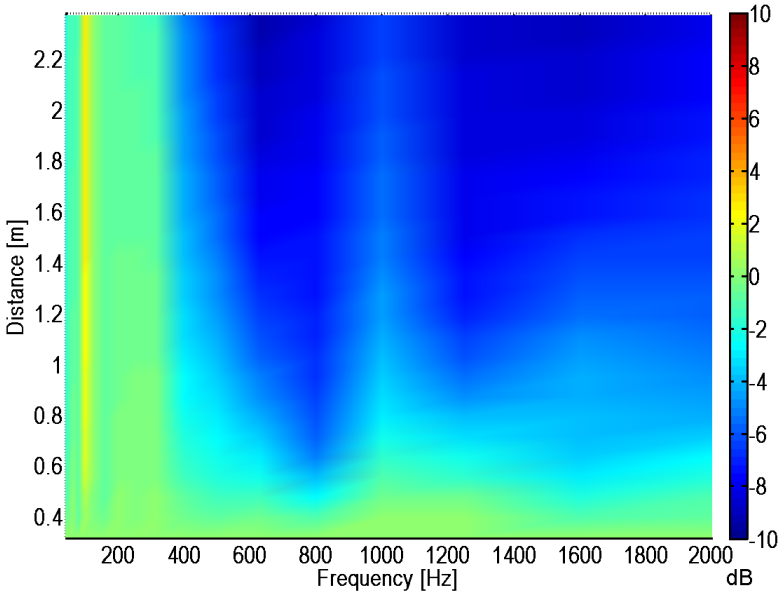

Figure 5.4 A surface plot of the error over frequency and distance for waveform 2 at 166 dB. The errors are between -4 and -6 dB for frequencies above 400 Hz and propagation distances greater than 0.6 meters. This illustrates the underestimation of the reconstructed pressure.

tion of distance and frequency in Figure 5.4. The errors are between -4 and -6 dB for frequencies above 400 Hz and propagation distances greater than 0.6 meters. This illustrates the underestimation of the reconstructed pressure.

The reconstructed PSDs for waveform 3 show an increase in energy at frequen-

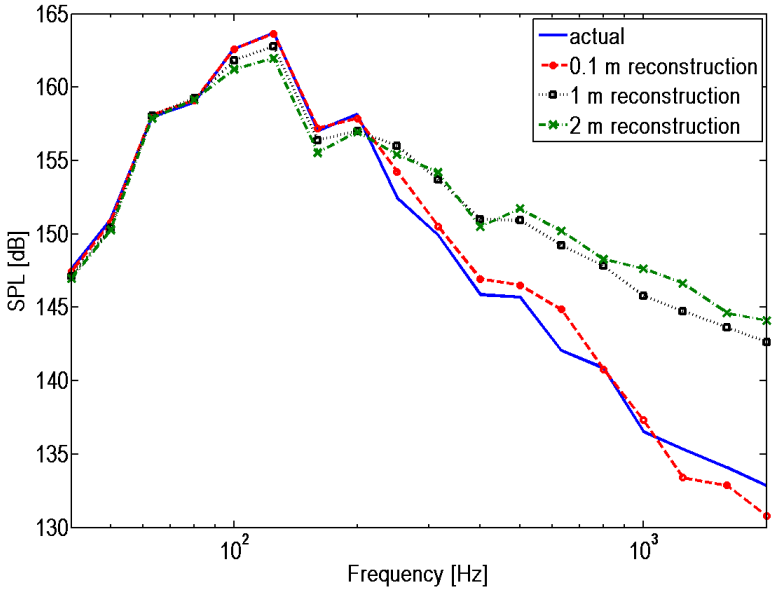

Figure 5.5 The reference and reconstructed power spectra for waveform 3 at 166 dB. The farther reconstruction distances greatly overestimate the high frequencies.

cies above the cut-off frequency and the slope of the decay to increase for only the reconstruction from 1 and 2 meters. The error is shown as a function of distance and frequency in Figure 5.6. The errors are between 4 and 8 dB for frequencies above 250 Hz and propagation distances greater than 0.6 meters. This illustrates the overestimation of the reconstructed pressure.

The reconstructed PSDs for waveform 4 are shown in Figure 5.7. The PSD shows a decrease in amplitude at the center frequency as well as a shift in the slope at low frequencies and high frequencies suggesting not only waveform steepening but also shock coalescence. The error is shown as a function of distance and frequency in Figure

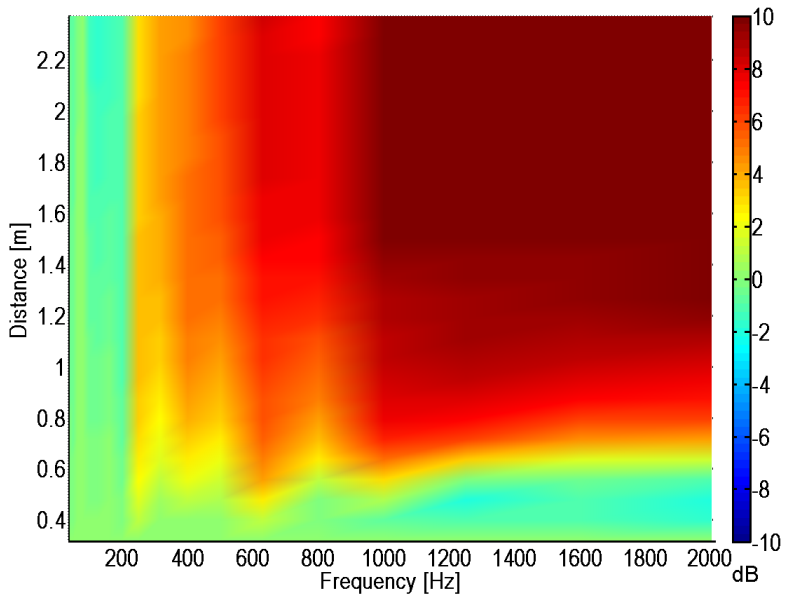

Figure 5.6 A surface plot of the error over frequency and distance for waveform 3 at 166 dB. The errors are between 4 and 8 dB for frequencies above 250 Hz and propagation distances greater than 0.6 meters. This illustrates the overestimation of the reconstructed pressure.

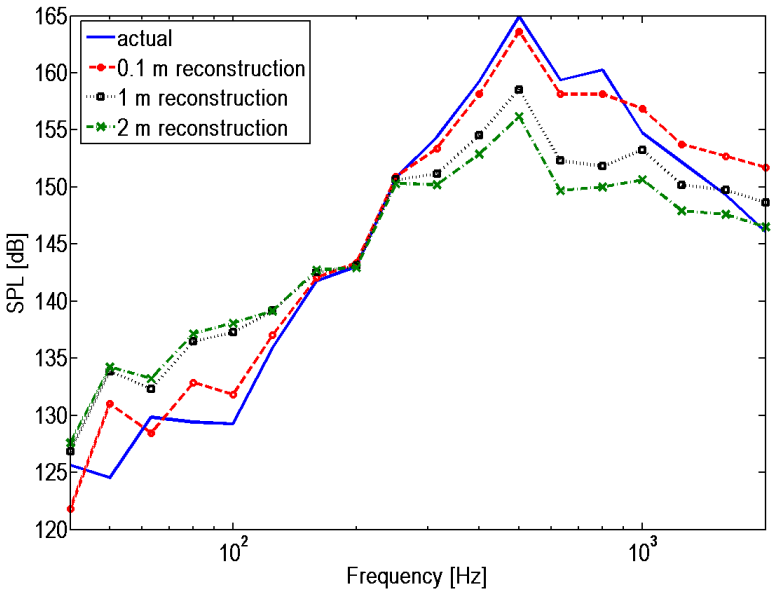

Figure 5.7 The reference and reconstructed power spectra for waveform 4 at 166 dB. The farther reconstruction distances change both the low-frequency rise and high-frequency decay.

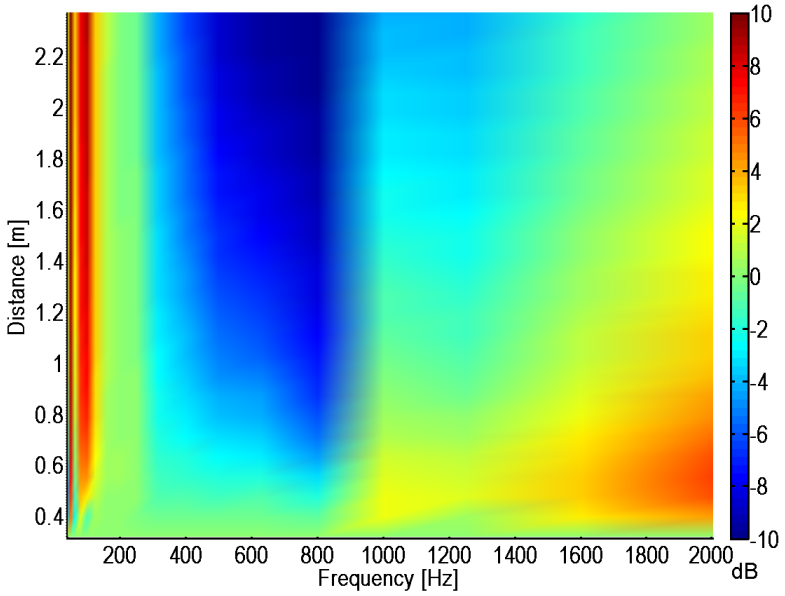

Figure 5.8 A surface plot of the error over frequency and distance for waveform 4 at 166 dB. The errors are positive below 100 Hz and negative between 300 and 1 kHz. This illustrates the overestimation of the reconstructed pressure at low frequencies and the underestimation of the reconstructed pressure at middle frequencies.

5.8. The errors are positive below 100 Hz and negative between 300 Hz and 1 kHz. This illustrates the overestimation of the reconstructed pressure at low frequencies and the underestimation of the reconstructed pressure at middle frequencies.

5.1.2 Averaged Errors

The error magnitudes were then averaged over frequency to determine an average error value and compare the performance of each waveform. Figure 5.9 depicts the

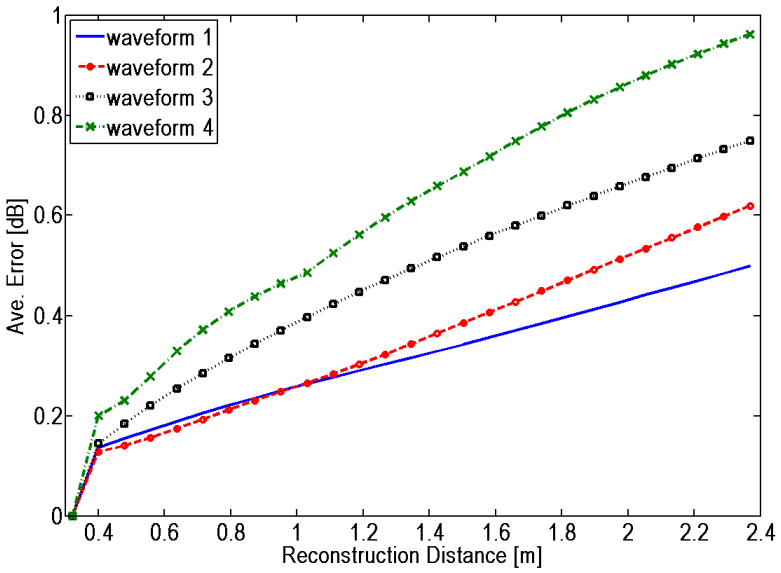

Figure 5.9 Average error plotted against distance for the four waveforms initially at 143 dB.

errors for the initially 143 dB case. Waveform 4 has the highest error and waveform 1 has the lowest, except at short distances where waveform 2 has the lower error. However, the error for reconstruction from 2 meters of all the waveforms are closer are under 1 dB.

Figure 5.10 shows the average error for the 158 dB case. Again, waveform 4 has the highest error and waveform 1 has the lowest, while waveforms 2 and 3 switch

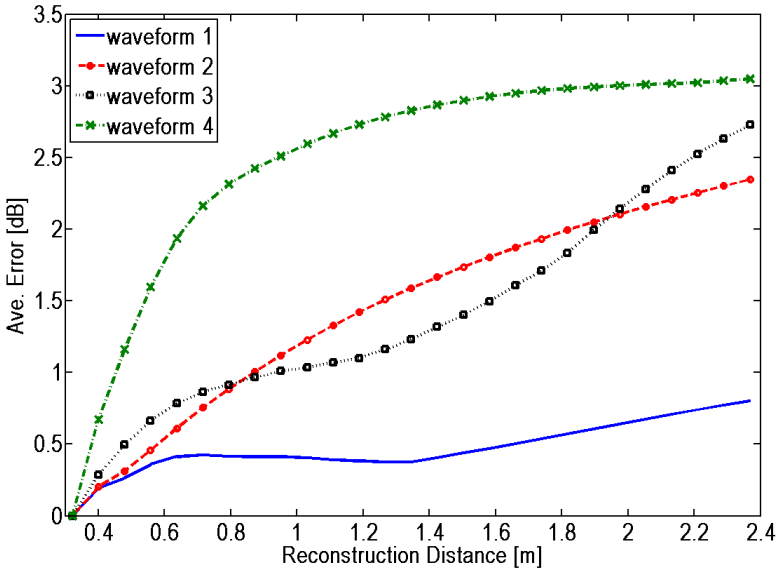

Figure 5.10 Average error plotted against distance for the four waveforms initially at 158 dB.

several times. For this case, only waveform 1 has errors under 1 dB at 2 meters, with the other three average errors close to or exceeding 2.5 dB.

Figure 5.11 shows the last of the three amplitudes, 166 dB. Waveform 1's error remains far below the other three and waveform 3 has the highest, exceeding 5 dB at 2 meters. Waveforms 2 and 4 also have average errors above 4 dB.

Waveform 1 has the lowest errors because of its self-preserving shape. The nonlinear effects filter the waveform to have the same shape. However, waveform 2 also has the same shape but exhibits much higher error at higher frequencies. As shown in Figure 5.3, the slope is maintained, but the loss in energy at the fundamental frequency causes the decay to become offset from its original position. Also, the center frequency appears to have shifted downward, further offsetting the high-frequency decay. The low-frequency slope, however, remains preserved. This shift is caused by more nonlinear effects that seem to be caused by the higher center frequency. This follows the same trend as seen in Equation 2.28 in that higher frequencies steepen

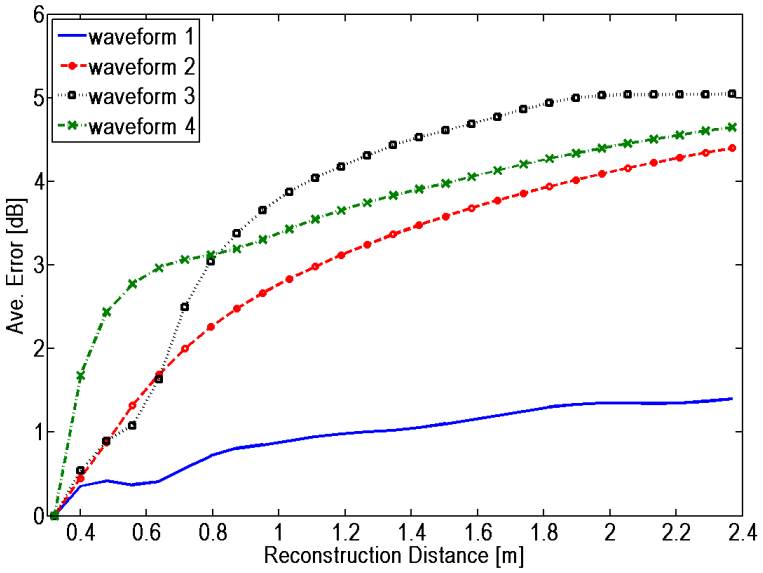

Figure 5.11 Average error plotted against distance for the four waveforms initially at 166 dB.

and form shocks more quickly.

Waveform 4 has greater errors than waveform 3 at most distances because of this same frequency-dependent effect. Both have experienced waveform steepening evident in the high- frequency increase. However, since waveform 4 has a shift in the low-frequency rise and waveform 3 does not, it seems that shock coalescence has not occurred significantly for waveform 3 yet, possibly due to the larger distances needed to experience distortion. The shift in waveform 4 effectively lowers the errors where the slopes intersect causing the average error to be lower than waveform 3 even though more nonlinear effects have occurred.

5.1.3 Summary

These four waveforms exhibit four separate effects that can occur when attempting reconstruction. The first two are for a waveform with a 'haystack' spectral shape. The first case is when nonlinear propagation effects do not change the already exist-

ing spectral shape, therefore allowing for good reconstruction. This occurs when only small amounts of energy are lost at the center frequency due to waveform steepening and no shock coalescence has occurred. Second, if a waveform does experience significant waveform steepening or shock coalescence, the reconstruction will only be good at low frequencies but will become very inaccurate at and above the center frequency. This is caused by the downward shift in the center frequency and not by a shift in the slope of the high-frequency decay. This effect can be caused by large amplitudes, long propagation distances and higher center frequencies.

The last two cases are for waveforms with the narrower spectrum. The third case occurs when waveform steepening causes a high frequency boost, but no shock coalescence occurs. This allows for good reconstruction below the center frequency but alters the spectral shape above the center frequency and causes significant reconstruction error. The last and final case is when both waveform steepening and shock coalescence occur, therefore boosting low and high frequencies and decreasing middle frequencies. This also leads to significant reconstruction error. This then becomes the limiting case as propagation distances, amplitudes and center frequencies increase.

5.2 Insight into Nonlinear Reconstruction in 2-D

Applying NAH in two-dimensions becomes quite different than the one-dimensional implementation. First, the spatial nature of the field must analyzed for single frequencies allowing for a spatial reconstruction at the source for that frequency. Second, the implementation must use cylindrical NAH and assume that the acoustic field exhibits circumferential symmetry. Finally, the spectral Fourier transform must be utilized to obtain complex data that is required to account for the phase. This would require enough data points to obtain a good frequency resolution.

Considering these factors, the major limitation for applying NAH to nonlinear sound fields in two dimensions is still obtaining the field itself. The WENO algorithm used is capable of obtaining these fields but at considerable cost. Parallel processing techniques may be used, but even then, 128 processors running for 9 days would only obtain a domain that is about one square meter. The propagation results shown in Chapter 4 were for a very small domain, still requiring a multi-day run time on a highly optimized processor, and were not sufficient to obtain accurate reconstruction.

However, the results of the one-dimensional reconstruction shed some insight into the errors that would arise when attempting to perform NAH reconstruction in two-dimensions. Reconstruction errors may be small when the spectrum already has the 'haystack' shape. As previously noted, as the amplitude, center frequency and propagation distance increase, the nonlinear effects become more significant and reconstruction errors will be large regardless of the initial 'haystack' shape.

These results do not take in account interference effects which were shown to be important for two-dimensional propagation in Chapter 4. Therefore, the 1-D results would not directly apply to the reconstruction of multiple or extended sources in nonlinear fields. The assumption that small nonlinear effects will cause small reconstruction errors is likely valid though.

Chapter 6

Conclusions

6.1 Summary

Four random noise waveforms were propagated nonlinearly in one dimension using the Wochner algorithm to test the effect of center frequency and spectral shape on the nonlinear propagation. The waveforms that were initially at 166 dB experienced significant nonlinear distortion after propagating two meters. Higher-order statistical analysis as well as bispectral analysis showed that the waveforms with higher center frequencies experience more distortion in shorter distances. Also, the narrower spectrally-shaped waveforms experienced more nonlinear effects. This confirms the need to consider nonlinear effects when studying this problem.

The higher-order statistical analysis confirmed the work of McInerny [35] that the time derivative is more sensitive to nonlinear effects, particularly the presence of shocks. However, the fact that skewness and kurtosis coefficients of the time derivative both decrease once the waveform is dominated by the shocks has not been known. This strengthens the potential of using higher-order statistics of time derivatives as a point or multi-point nonlinearity indicator to extract information about the relative

amount of nonlinearity occurring. Specifically, the skewness and kurtosis of the time derivative could show whether waveform steepening or shock decay is more significant, information that is not currently available from point nonlinearity indicators.

These nonlinearly propagated waveforms were then reconstructed using one-dimensional spherical NAH. Waveform 1 showed the least amount of error due to the self-preserving nature of its spectral shape. However, the errors for waveform 2, which were also small for very short propagation distances, were significant after propagating 2 meters despite having the same spectral shape. This is due to the increased amount of nonlinearity, which then causes the center frequency to shift downward and its amplitude to decrease. Waveforms 3 and 4 also had significant reconstruction error as the nonlinear propagation effectively filtered the spectral shape of the waveform to have f^2 dependence.

This implies that a 'haystack' spectrum with a low center frequency, a very small propagation distance or low amplitude could be reconstructed correctly in regions where the spherical spreading assumption holds. However, since all three factors play a significant roll in the propagation, it may be difficult to predict whether this would actually be the case. However, if the higher-order statistics of the time derivative were known to be decreasing, this could indicate that the nonlinearity would cause large reconstruction errors. Reconstruction of a narrow-band spectrum will likely always have significant error when any nonlinear effects are present due to the filtering effects of the distortion.

Propagation of narrow-band-noise from two point sources in two dimensions also showed the effects of nonlinear distortion. However, the interference effects of the steepened waveforms created more errors than expected. Since the broadband waveforms are random, the deviations from linear behavior become more unpredictable with increasing amplitude. This would imply that a holography scheme must in-

clude nonlinear interference/diffraction terms for accurate reconstruction of a finite-amplitude sound field if the holography plane is in the near-field of the source.

6.2 Applications to Rocket and Jet Noise Imaging

The specific application of this research is to determine the accuracy of using NAH to reconstruct the acoustic source of a rocket. However, jets and rockets are similar in their source mechanisms and this research is therefore naturally extended to jets. The major benefit for possible imaging rockets over jets is the low center frequency associated with its spectra, which require longer distances for nonlinear effects to occur. However, since amplitudes are so high, nonlinear effects may still occur over very short distances and it is possible that amplitudes are high enough to fall into the strongly nonlinear regime where shocks can form right at the source (see Reference [71]). Jets on the other hand have higher center frequencies which would more experience nonlinearity over shorter distances but lower amplitudes. Considering only these factors (center frequency and amplitude), it remains difficult to predict which source would have more accurate reconstruction.

It must be noted that before any imaging of either jet or rocket sources could be performed, several other problems that must be overcome. First, a typical rocket or jet source can be quite large, extending several tens of meters with directional radiation. This would cause even more complicated diffraction effects and could require a very large microphone array. Additionally, rockets are typically fired in the vertical position, with the plume usually being deflected to the side by a large deflector. This could severely limit the locations where acoustical measurements are even possible and introduction reflection effects. Jets may also have limited accessibility and ground reflection problems. Lastly, the temperatures associated with

rocket launches are very high. The temperature fluctuations would greatly change the behavior of the acoustic field and create other problems with the measurement hardware. Although temperatures effects are not as great for jets, they can be large enough to significantly alter the acoustical behavior. Additionally, other atmospheric effects, such as temperature gradients, turbulence and wind, would likely significantly affect the noise propagation. However, these effects may be low over small distances.

To conclude, nonlinear propagation effects can cause significant errors in finite-amplitude reconstruction techniques. It is possible though that that these errors may be small due to a low center frequency, 'haystack' spectral shape, short propagation distance or low but still finite in nature amplitude. However, for real-life application to rockets, many other problems also exist that make it difficult to reach definitive conclusions.

6.3 Future Work

The results of two-dimensional finite-amplitude propagation were discussed in Chapter 4. This research could be extended by performing NAH reconstruction in 2-D and determining the reconstruction errors. The NAH implementation must then change from spherical to cylindrical and assume azimuthal symmetry, or no dependence in the circumferential (ϕ) direction. This would be a more realistic application of NAH, where all spatial points are imaged for a single frequency.

Additional research could also be performed to study and experimentally verify the evolution of the statistics of the time derivative of random noise using a shock tube. Perhaps more insight could be gained into the physical meaning of this occurrence, which may be valuable in the study of intense random-noise.

Future work could also include verifying the reconstruction results experimentally

by measuring actual rocket data to determine realistic propagation distances, sound pressure levels, and temperatures. It would actually be recommended that the future direction of experimental research be using model-scale jets. This could allow for a more complete study in a controlled environment to be performed that is also less expensive. The results could then be applied to full-scale jets and finally to rockets.

Bibliography

[1] Gonzalez, G., Miller, N., Istre, C. "The Influence of Rocket Noise on the Hearing of Guinea Pigs," *Aero. Med.* **41**(1): 21-25, 1970.

[2] Cole, J.N., von Gierke, H.E., Kyrazis, D.T., Humphrey, A.J., "Noise radiation from fourteen types of rockets in the 1,000 to 130,000 pounds thrust range," WADC TR 57-354 AD 130794, Dec 1957.

[3] Mayes, W.H., Lanford, W.E., and Hubard, H.H., "Near-field and Far-field Noise Surveys of Solid-fuel Rocket Engines of a Range of Nozzle Exit Pressures," NASA TN D-21, Aug 1959.

[4] Potter, R.C., Crocker, M.J., "Acoustic prediction methods for rocket engines, including the effects of clustered engines and deflected exhaust flow," NASA-CR-566, Oct 1966.

[5] Potter, R.C. "Noise Field for Shadowgraph Model Rocket Experiments," NASA-CR-76267, 1966.

[6] Potter, R.C. "Investigation to locate the acoustic sources in a high speed jet exhaust stream," NASA-CR-101105, 1968.

[7] McInerny, S. "Rocket Noise - A Review," *AIAA 13th Aeroacoustics Conference* **90**: 1-7, 1990.

[8] McInerny, S. "Characteristics and Predictions of Far-field Rocket Noise," *Noise Con. Eng. J.* **38**(1): 5-16, 1992.

[9] Lighthill M.J., "The Bakerian Lecture, 1961. Sound Generated Aerodynamically," *Proceedings of the Royal Society of London. Series A, Mathematical and Physical Sciences* **267**(1329): 146-182, 1962.

[10] Lighthill M.J., "On Sound Generated Aerodynamically II: Turbulence as a Source of Sound," *Proceedings of the Royal Society of London. Series A, Mathemcatical and Physical Sciences* **222**(1148): 1-32, 1954.

[11] Eldred, K.M, "Acoustic Loads Generated by the Propulsion System," NASA SP-8072, June 1971.

[12] Yang, M., "Prediction of liftoff acoustic environments for launch pads with covered ducts," *J. Acoust. Soc. Am.* **122**(5): 3095, 2007.

[13] Varnier, J. "Experimental Study and Simulation of Rocket Engine Freejet Noise," *AIAA J.* **39**(10): 1851-1859, 2001.

[14] Tam, C.K.W. "Computational Aeroacoustics: An Overview of Computational Challenges and Applications," *Int. J. of Comp. Fluid Dyn.* **18**(6): 547-567, 2004.

[15] Lilley, G.M., "Jet Noise Classical Theory and Experiments," Ch. 6 *Aeroacoustics of Flight Vehicles, Theory and Practice–Volume 1: Noise Sources*, 1994.

[16] Tam, C.K.W., "Jet Noise Generated by Large-Scale Coherent Motion," Ch. 4 *Aeroacoustics of Flight Vehicles, Theory and Practice–Volume 1: Noise Sources*, 1994.

[17] Lowson, M.V. and Ollerhead, J.B. "Visualization of Noise from Cold Supersonic Jets," *J. Acoust. Soc. Am.* **44**(2): 624-630, 1968.

[18] Fuchs, H.V. "On the application of acoustic "mirror", "telescope" and "polar correlation" techniques to jet noise source location," *J. of Sound and Vib.* **58**(1): 117 - 126, 1978.

[19] Laufer, J., Schlinker, R. and Kaplan, R.E. "Experiements on Supersonic Jet Noise," *AIAA J.* **14**(4): 489-497, 1976.

[20] Brusniak, L., Underbrink, J. and Stoker, R., "Acoustic Imaging of Aricraft Noise Sources Using Large Aperature Phased Arrays," *Proceedings of 12th AIAA/CEAS Aeroacoustics Conference* 2006-2715, 2006.

[21] Venkatesh, S.R., Polak, D.R., Narayanan, S., "Beamforming algorithm for distributed source localization and its application to jet noise," *AIAA* **41**(7): 1238-1246, 2003.

[22] Varnier, J. "Experimental Characterization of the Sound Power Radiated by Impinging Supersonic Jets," *AIAA J.* **40**(5): 825-831, 2002.

[23] Yu, J.C., Dosanjh, D.S, "Noise Field of a Supersonic Mach 1.5 Cold Model Jet," *J. Acoust. Soc. Am.* **51**(5): 1400-1410, 1972.

[24] Maynard, J.D., Williams, E.G., and Lee, Y. "Nearfield acoustic holography: I. Theory of generalized holography and the development of NAH ," *J. Acoust. Soc. Am.* **78**(4):1395 -1413 ,1985.

[25] Williams, E.G., Maynard, J.D. "Holographic imaging without the wavelength resolution limit," *Phys. Rev. Let.* **45**: 554-557, 1980.

[26] Zhaoxi, W., Wu, S.F. "Helmholtz equation-least-squares method for recontructing the acoustic pressure field," *J. Acoust. Soc. Am.* **102**(4): 2020-2032, 1997.

[27] Veronsi, W.A. Maynard, J.D. "Digital holographic reconstruction of sources with arbitrarily shaped surfaces," *J. Acoust. Soc. Am.* **85**(2): 588-598, 1989.

[28] Cho, Y.T., Bolton, J.S. "Source visualization by using statistically optimized near-field acoustical holography in cylindrical coordinates," *J. Acoust. Soc. Am.* **118**(4): 2355-2364, 2005.

[29] Harris, M.C., Blotter, J.D., Sommerfeldt, S.D. "Obtaining the complex pressure field at the hologram surface for use in near-field acoustical holography when pressure and in-plane velocities are measured," *J. Acoust. Soc. Am.* **119**(2): 808-816, 2006.

[30] Lee, M., Bolton, J.S. "Source characterization of a subsonic jet using near-field acoustical holography," *J. Acoust. Soc. Am.* **121**(2): 967-977, 2007.

[31] Pundarika G., Lakshminarayana, R., Sheshadri, T.S., "Application of holography to jet acoustic studies," *Sādhanā* **29**(4): 389-400, 2004.

[32] Morfey, C.L., Howell, G.P. "Nonlinear Propagation of Aircraft Noise in the Atmosphere," *AIAA J.* **19**(8): 986-992, 1981.

[33] Gee, K.L., Gabrielson, T.B., Achtley, A.A., Sparrow, V.W. "Preliminary Analysis of Nonlinearity in Military Jet Aircraft Noise Propagation," *AIAA J.* **43**(6): 1398-1404, 2005.

[34] McInerny, S.A., "Launch Vehicle Acoustics Part 1: Overall Levels and Spectral Characteristics," *J. of Aircraft* **33**(3): 511-517, 1996.

[35] McInerny, S.A., "Launch Vehicle Acoustics Part 2: Statistics of the Time Domain Data," *J. of Aircraft* **33**(3): 518-523, 1996.

[36] McInerny, S.A., Olcmen, S.M. "High-intensity rocket noise: Nonlinear propagation, atmospheric absorption, and characterization," *J. Acoust. Soc. Am.* **117**(2): 578-591, 2005.

[37] Maynard, J.D. "Nearfield acoustical holography and Nonlinear Sound Fields," *J. Acoust. Soc. Am.* **121**(3069), 2007.

[38] Kinsler, L.E., Frey, A.R., Coppens, A.B., Sanders, J.V., *Fundamentals of Acoustics, 4th Edition*, John Wiley, New York, 2000.

[39] Oppenheim, A.V., Schafer, R.W., Buck, J.R., *Discrete-time Signal Processing, 2nd Edition*, Prentice Hall, New Jersey, 1999.

[40] Notes from Dr. Timothy Leishman's physics 565 lecture, winter semester 2005.

[41] Asmar, N. *Partial Differential Equations and Boundary Value Problems*, Prentice Hall, New Jersey, 2000.

[42] Blackstock, D.T., *Fundamentals of Physical Acoustics*, John Wiley, New York, 2000.

[43] "Acoustics - Attenuation of sound during propagation outdoors - Part 1: Calculation of the absorption of sound by the atmosphere," International Standard 9613-1 First Ed. 1993-06-01.

[44] Atchley, A.A., "Not your ordinary sound experience: a nonlinear acoustics primer," *Acoustics Today* **1**(1): 19-24, 2005.

[45] Hamilton, M.F., Blackstock, D.T., Pierce, A.D., "Progressive Waves in Lossless and Lossy Fluids," Ch.4 *Nonlinear Acoustics*, Academic Press, San Diego, 1998.

[46] Blackstock D.T., "History of Nonlinear Acoustics: 1750s-1930s," Ch.1 *Nonlinear Acoustics*, Academic Press, San Diego, 1998.

[47] "Wolfram Mathworld" accessed online at http://mathworld.wolfram.com/SawtoothWave.html on 10 August 2007.

[48] Pierce, A. D., *Acoustics: An Introduction to Its Physical Principles and Applications*, Acoustical Society of America, New York, 1989.

[49] Pestorius, F.M., Blackstock, D.T., "Experimental and Theoretical Study of Propagation of Finite-Amplitude Noise in a Pipe," *J. Acoust. Soc. Am.* **54**(302): 1973.

[50] Pestorius, F.M., *Propagation of Plane Acoustic Noise of Finite Amplitude*, Ph.D. dissertation, The Univerisity of Texas at Austin, 1973.

[51] Gee, K.L., *Prediction of Nonlinear Jet Noise Propagation*, Ph.D. dissertation, The Pennsylvania State University 2005.

[52] Blackstock, D.T., "Connection between the Fay and Fubini Solutions for Plane Sound Waves of Finite Amplitude," *J. Acoust. Soc. Am.* **39**(6): 1019-1026, 1966.

[53] Morse, P.M., Ingard, K. U., *Theoretical Acoustics*, Princeton Univ. Press, Princeton, 1968.

[54] Wochner, M.S., *Numerical Simulation of Multi-Dimensional Acousitc Propagation in Air Including the Effects of Molecular Relaxation*, Ph.D. dissertation, The Pennsylvania State University 2006.

[55] Sparrow, V., Raspet, R., "A numerical method for general finite amplitude wave propagation in two dimensions and its application to spark pulses," *J. Acoust. Soc. Am.* **90**(5): 2683-2691, 1991.

[56] Wochner, M.S., Atchley, A.A., Sparrow, V.W, "Numerical simulation of finite amplitude wave propagation in air using a realistic atmospheric absorption model," *J. Acoust. Soc. Am.* **118**(5): 2891-2898, 2005.

[57] Williams, E.G., *Fourier Acousics: Sound Radiation and Nearfield Acoustical Holography*, Academic Press, San Diego, 1999.

[58] Williams, E.G., "Regularization methods for nearfield acoustic holography," *J. Acoust. Soc. Am.* **110**(4):1976-1988, 2001.

[59] Lee, M., Bolton, J.S., Mongeau, L., "Application of cylindrical near-field acoustical holography to the visualization of aeroacoustic sources," *J. Acoust. Soc. Am.* **114**(2): 842-858, 2003.

[60] Bendat, J.S., Peirsol, A.G., *Random Data: Analysis and Measurement Procedure*, John Wiley, New York, 2000.

[61] Arfken G.B., Weber H.J., *Mathematical Methods for Physicists 5th Ed.*, Harcourt Academic Press, San Diego, 1995.

[62] Gee, K.L, Atchley, A.A., Falco, L.E., Gabrielson, T.B., Sparrow, V.W.,"Bispectral Analysis of High-amplitude Jet Noise," *Proceedings of 11th AIAA/CEAS Aeroacoustics Conference* 2005-2937, 2005.

[63] Kim, K.I., Powers, E.J., "Digital Bispectral Analyisis and its Application to Nonlinear Wave Interactions," *IEEE Transactions on Plasma Science*, **PS-7**(2): 120-131, 1979.

[64] Hagihira, S., Takashina, M., Mori, T., Ueyama, H., and Mashimo, T., "What we can know from bispectral analysis of EEG?," *International Congress Series*

- Basic and Systemic Mechanisms of Anesthesia: Proceedings of the 7th International Conference on Basic and Systematic Mechanisms of Anesthesia **1283**: 239-242, 2005.

[65] Brockett, P.L., Hinich, M., Wilson, G.R., "Nonlinear and non-Gaussian ocean noise," *J. Acoust. Soc. Am.* **82**(4): 1386-1394, 1987.

[66] Gee, K.L, Shepherd, M.R., Falco, L.E., Atchley, A.A., Ukeiley, L.S., Jansen, B.J., Seiner, J.M., "Identification of Nonlinear and Near-field Effects in Jet Noise Using Nonlinearity Indicators," *Proceedings of 13th AIAA/CEAS Aeroacoustics Conference* pp, 2007.

[67] Thornhill, R.J., Smith, C.C., *Fourier, Spectral, and Wavelet Analysis in Dynamic Systems*, 2004.

[68] Keller, G., *Applied Statistics with Microsoft Excel*, Duxbury, Pacific Grove, 2001.

[69] Gurbatov, S.N., Rudenko, O.V., "Statistical Phenomena," Ch. 13 *Nonlinear Acoustics*, Academic Press, San Diego, 1998.

[70] Flaherty J.E., *Numerical Solution of Partial Differential equations*, Rensselaer Polytechnic Institute Press, Troy, NY, 1999.

[71] Inoue, Y., Yano, T., "Propagation of strongly nonlinear plane waves," *J. Acoust. Soc. Am.* **94**(3): 1632-1642, 1993

Appendix A

The Basics of Finite-difference Approximations

Finite-difference schemes are frequently used to solve ordinary and partial differential equations or sets of equations with complicated or unknown analytical solutions, but can also be used to solve simple equations. Many schemes have been developed, some which are very efficient for solving certain equations but cannot solve others. For this reason, it has become common to separate the temporal and spatial aspects of an equation, estimate the respective derivatives using an efficient finite-difference scheme, solve the respective portion of the equation explicitly or implicitly and then to combine the results.

The theory behind finite-difference approximations is that of series expansions. A Taylor series expansion is shown here for the function f evaluated at x.

$$f(x) = f(a)+f'(a)(x-a)+\frac{f''(a)}{2!}(x-a)^2+\frac{f'''(a)}{3!}(x-a)^3+\ldots+\frac{f^{(n)}(a)}{n!}(x-a)^n, \quad \text{(A.1)}$$

where $'$ denotes a derivative that is defined at that location. If $f(a) = U(x_j)$ and $f(x) = U(x_{j+1})$, the expansion can be truncated by removing all terms above some

order and rewritten as

$$U(x_{j+1}) = U(x_j) + U'(x_j)(x_{j+1} - x_j) + \tau, \tag{A.2}$$

where τ becomes the local truncation error. Since $x_{j+1} - x_j$ can be simplified to Δx, the expression can be further rearranged to obtain

$$U'(x_j) = \frac{U(x_{j+1}) - U(x_j)}{\Delta x} - \frac{\tau}{\Delta x}, \tag{A.3}$$

which is a first-order forward-difference estimate because the estimate uses information at x_{j+1} to determine the value of the derivative at x_j and could be easily modified to obtain a backward-difference estimate. τ then reveals the highest order of the error, which in this case is $\mathcal{O}(\Delta x)$, or of order Δx. A centered-difference estimate is obtained by subtracting two series expansions centered at $j + 1$ and $j - 1$ and the local truncation error is $\mathcal{O}(\Delta x^2)$, becoming a higher-order accurate approximation. All three schemes become more accurate by keeping more terms in series before truncating [70].

Since all numerical work is inherently discrete, this makes for easy implementation of finite-difference approximations. The number of points used in the estimate is known as the stencil size, where the stencil represents all the group of points used in the finite-difference estimate. One can use one stencil or multiple stencil schemes with combinations of backward-, forward-, and centered-difference estimates.

Each scheme requires three criteria to achieve accurate results: consistency, stability and convergence. Consistency means that as the discretization step decreases and goes to zero, the estimate becomes the exact solution or $\tau = 0$. Stability refers to when small changes in initial or boundary conditions do not alter the solution. Convergence would then mean that the numerical solution approaches the actual solution within some tolerance. For a scheme to be stable a realizable relationship

must be maintained between the spatial steps and temporal steps. When this occurs, convergence is automatically achieved. For wave problems, the wave speed c then plays an important part in determining the necessary ratio between the two for stability. This ratio is known as the Courant-Fredrichs-Levy (CFL) number. For simple finite-difference schemes, consistency and stability can be proven analytically. However, both conditions are specific to the equation being solved and are not easily determined for more complex finite-difference schemes used on complicated equation sets [70].